Title
Ferromagnetic Resonance Enhanced Electrically Small Antennas

Author
Gu, Wei

Publication Date
2019

Peer reviewed|Thesis/dissertation

UNIVERSITY OF CALIFORNIA

Los Angeles

Ferromagnetic Resonance Enhanced Electrically Small Antennas

A dissertation submitted in partial satisfaction of the

requirements for the degree Doctor of Philosophy

in Electrical and Computer Engineering

by

Wei Gu

2019

ABSTRACT OF THE DISSERTATION

Ferromagnetic Resonance Enhanced Electrically Small Antennas

by

Wei Gu

Doctor of Philosophy in Electrical and Computer Engineering

University of California, Los Angeles, 2019

Professor Yuanxun Wang, Chair

An innovative idea that ferromagnetic resonance (FMR) can be utilized to improve the radiation efficiency E_{rad} and input impedance Z_{in} matching for electrically small antennas (ESAs) simultaneously is proposed. This idea is inspired by the recent discovery that using magnetic materials with extremely large imaginary permeability μ'' can still achieve high E_{rad} in designs of ESAs. The equation of E_{rad} for ESAs as a function of ferrites' complex permeability μ is re-derived based on the field modeling and analysis of an ideal thin-film ferrite radiator to verify the discovery. Furthermore, taking FMR into consideration, a conclusion is made that the gilbert damping factor α of the resonance determines E_{rad} more essentially than μ of ferrites. The first practical design for the proposed FMR enhanced ESAs has been realized through a modified, small single loop antenna loaded with a thin-film yttrium-iron-garnet (YIG) core. A real physical prototype has been fabricated and evaluated through both full-wave simulations and experiments. The simulation results match to the experimental results, demonstrating the efficacy and

significance of the idea. Novel frequency-independent, equivalent circuit models for small loops and FMR enhanced ESAs have been developed in this paper to guide the design of highly efficient ESAs in the future. The circuit models prove to be trustworthy in predicting Z_{in} and E_{rad} by comparing with full-wave simulations and agreed.

The dissertation of Wei Gu is approved.

Tatsuo Itoh

Gregory P. Carman

Kung Yao

Yuanxun Wang, Committee Chair

University of California, Los Angeles

2019

TABLE OF CONTENTS

LIST OF FIGURES

LISTS OF TABLES

Biographical Sketch

Wei Gu received his B.S. degree in Electrical and Electronic Engineering from Beijing Institute of Technology, Beijing, China, in 2013 and the M.S. degree in Electrical Engineering from the University of California at Los Angeles (UCLA), Los Angeles, USA, in 2016. He joined the Digital Microwave Laboratory at UCLA in 2014 to pursue the PhD degree in Electrical and Computer Engineering and conduct research on dynamic characterizations for magnetic materials and novel electrically small antenna design with magnetic materials, as a Graduate Student Researcher, under the supervision of Prof. Y. E. Wang. He has also served as a Teaching Assistance in ECE230A at UCLA for three years. His current research interests include antenna theory and design, micro-magnetism for RF applications and circuit modeling of RF devices.

CHAPTER I

INTRODUCTIONS

1.1 Demands and Definitions for Electrically Small Antennas

The topics regarding electrically small antennas (ESAs) have drawn continual attentions in the wireless communication society starting from the early 20s. As the concept of internet of things (IOT) is prevailing nowadays [1], the demand for efficient small antennas has also peaked to a level higher than it ever was before. The realization of solid connections among those physical devices inside IOT relies on the promising performances of ESAs installed on them [2]. Most of the time, applications within IOT are either portable or mobile. So it is not practical to have an antenna even larger in size than the application itself. Then the primary goal for the antenna design in those applications is to have the dimension of the antenna as small as possible without degrading its performance [3].

Figure 1. Internet of things and three examples of its applications with small antennas: fit-bits, smart shirts and VR oculus.

However, unlike integrated circuits, antennas don't follow Moore's Law. In other words, it is physics principles rather than manufacturing techniques that puts constrains on the size miniaturization of an antenna. But again even though the challenge in the ESA design is severe, engineers never stop trying to find different and innovative approaches to optimize the performance of the ESA while shrinking its size.

Before jumping to those physical limits for the antenna size, it is necessary to review the definitions of electrically small antennas [4]. Generally speaking, the largest physical dimension of an antenna $D_{max} = 2a$ is on the order of a quarter of its operating wavelength λ in extent or less is considered electrically small, such as $D_{max} < 0.25\lambda$. A more precise and physical definition for ESAs starts from Wheeler [5] and has been widely adopted. An imaginary sphere of radius r with $\beta r = 1$, named *radiansphere,* is introduced to specify how much small is small enough. Any antenna can be completely enclosed by *radiansphere* falls to the electrically small category.

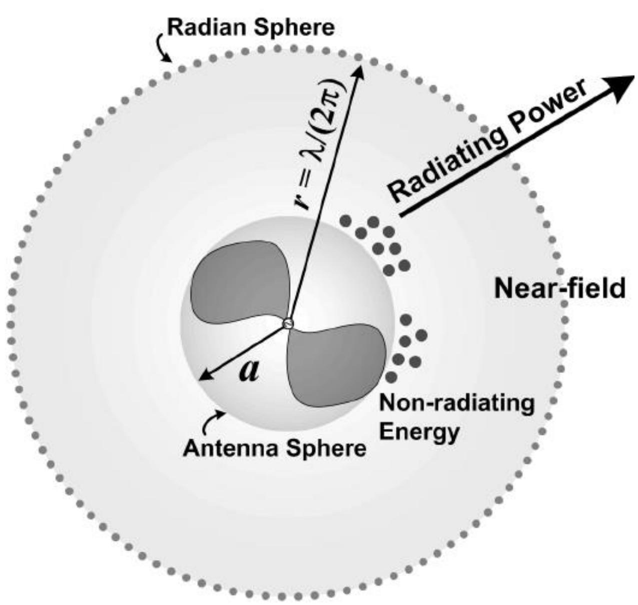

Figure 2. Wheeler's *radiansphere* and definition of electrically small antennas.

The significance of *radiansphere* is that it marks the boundaries between ESAs' near-field and far-field regions. Inside the *radiansphere* is where the near-field reactive energy of ESAs is stored, while outside of it is where the far-field, radiating power of ESAs propagates.

1.2 Two Types of ESAs and Their Radiation Sources

Based on which type of near-field, reactive, stored energy is dominant, magnetic energy W_m or electrical energy W_e, ESAs can be separated into two kinds, inductive and capacitive ones. Observing from a point quite far from ESAs, the actual geometric structures of ESAs no longer matter to the far-field distributions. Therefore, from a far-field perspective, any ESA can be either modeled as an ideal electric dipole or an ideal magnetic dipole (small loop), which are also the two simplest elements that consist of antenna systems and arrays. What is worth to be mentioned is that two ideal dipoles' near-field components are also good approximations to the nearfields of any ESA for one of the corresponding types mentioned above. This is also known as the Wheeler's Approximation [6], which is one of the important foundations for conducting field analysis to ESAs and a very useful and convenient tool to model ESAs as well.

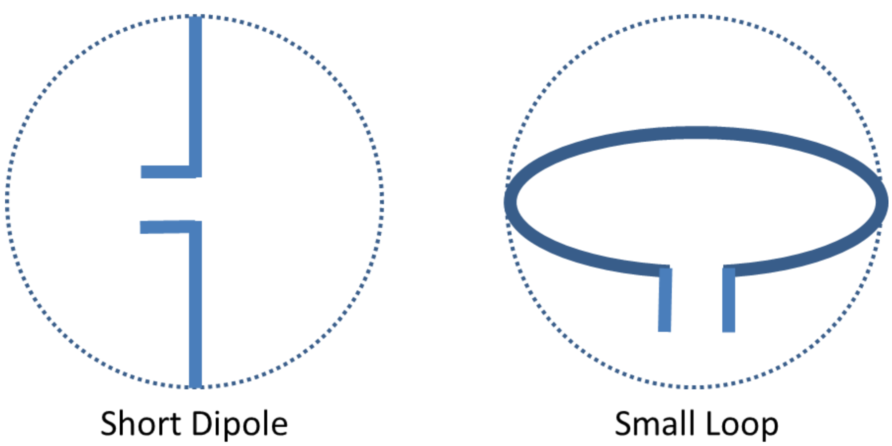

Figure 3. Two ideal models for two types of ESAs: short dipoles for capacitive ESAs and small loops for inductive ESAs.

Technically different types of ESAs have different radiation sources which have been indicated in the two curl ones of the Maxwell equations [7]:

$$\nabla \times \mathrm{H} = J \tag{1.1}$$

$$\nabla \times \mathrm{E} = -\mathrm{M} \tag{1.2}$$

Capacitive ESAs are stimulated by electrical currents J supported by the antenna structure, while inductive ESAs are excited by the magnetic currents M. Since there is only free electric charges existing in the nature but no physical magnetic charges, we have two types of electric currents, the impressed conduction current J_e and the electric displacement current $\frac{\partial D}{\partial t}$, as the radiation sources of an ideal electric dipole. On the other hand, the magnetic displacement current $\frac{\partial B}{\partial t}$ is the one and only type radiation source for inductive ESAs.

$$\mathrm{J} = \frac{\partial D}{\partial t} + J_e \tag{1.3}$$

$$\mathrm{M} = \frac{\partial B}{\partial t} \tag{1.4}$$

The most common practice of forming an equivalent magnetic current or magnetic dipole is to apply a time-varying conduction current to a loop conducting structure.

In this dissertation, small loop antennas and their transformations are the main type of ESAs investigated here. The logic behind the choice of type of ESAs for this research project can be summarized as below:

First, small loop antennas have their unique advantages when it comes to conformal antenna designs, compared to small electric dipole antennas. One of common realizations for a small electric dipole is a small wipe or blade antenna. Basically it is a small monopole vertically placed over a very large conducting surface, like the exterior of an air-plane or a vehicle. According to the image theory, it shares the same field distributions above the conducting platform as a small electric dipole. This stand-out antenna operates over a narrow frequency band at VHF or UHF. So it usually needs multiple antennas of this kind to form an array in order to accomplish certain functions, such as navigation or communication. The array formation makes these antennas even more protruding. And putting a small electric dipole in the horizontal direction is not an option for its invisibility with a conspicuous reason that its image source associated with the conducting plane, will have an opposite orientation and cancel most of its radiating field if not all when it is located very close to the conducting surface. Unless the horizontal small electric dipoles are placed at a height of one fourth of the operating wavelength $\frac{\lambda}{4}$ to the metallic ground. However, that goes against the initial purpose of using horizontal small electric dipoles which is to make the antenna much more low-key.

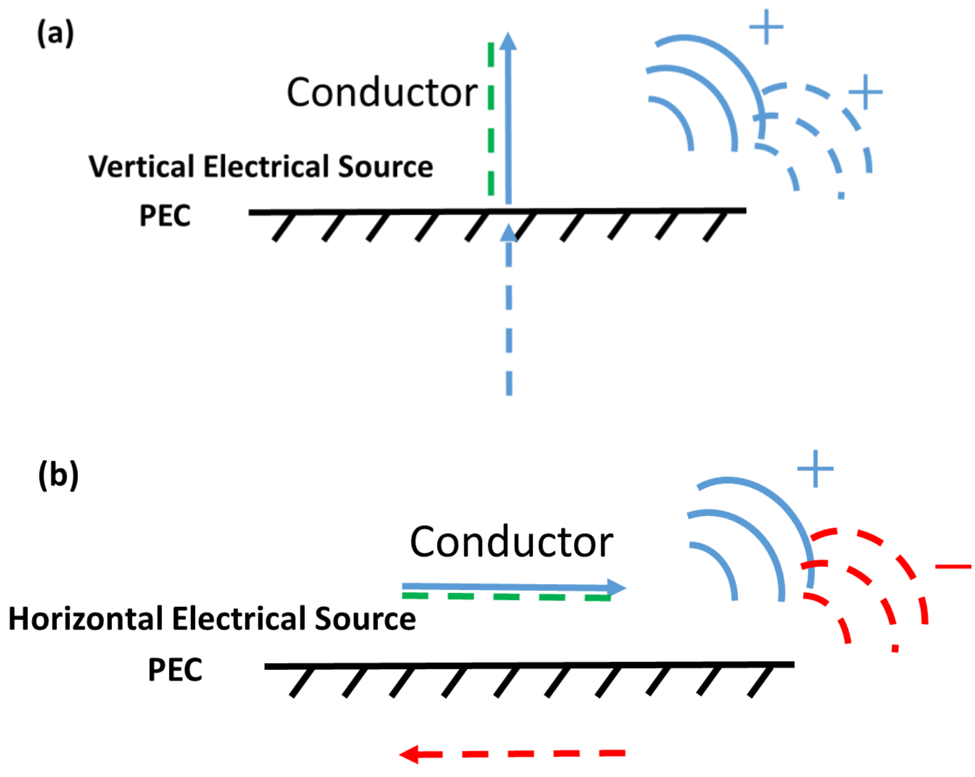

Figure 4. Image theory of electrical sources and PEC: a) vertically placed and b) horizontally placed.

In the image theory [7], the situation where a small magnetic dipole or small loop is placed horizontally neighboring to the conducting surface has also been investigated. Instead of having the image source neutralize the radiation from the original small electric dipole, the image source of a small loop exists to the benefit of the radiation from the original small loop. The orientation of its image source aligns with the small loop, which provides a path to circumvent the ground plane effect problem occur in the horizontal small electric dipole case. It is reasonable to design a high efficient, conformal ESA starting from a small metallic antenna in the shape of a single loop. Furthermore, adjustments to the geometry of a small loop should be made accordingly in favor of its radiation performance improvement.

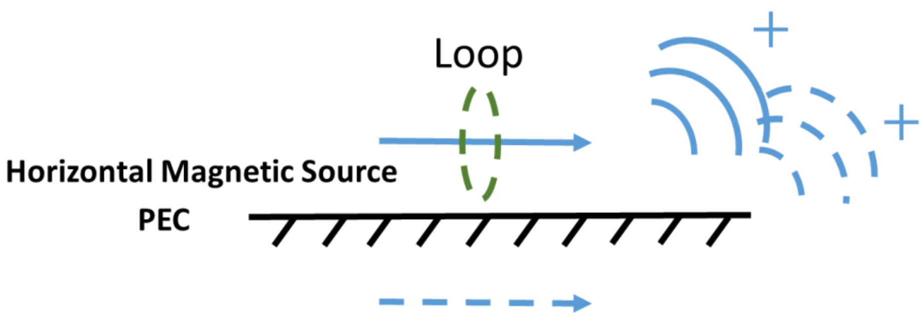

Figure 5. Image theory of the horizontal magnetic source and PEC.

Second, penetrable ferrite materials are suggested to enhance the radiation performance of ESAs. Ferrite materials are inductive, magnetic materials. The interactions between RF signal fields carried by the ESA and ferrite materials are built up through a significant amount of magnetic anisotropy which ferrites have. Magnetic anisotropy is also known as tensor permeability. By further expend the magnetic displacement current expression in Faraday's Law with respect to H field density and permeability, we will see exactly how ferrites contribute to magnetic radiation sources by separating out the magnetic polarization current density term $\mu_0(\mu_r - 1)\frac{\partial H}{\partial t}$.

$$\mathrm{M} = \frac{\partial B}{\partial t} = \mu_0 \frac{\partial H}{\partial t} + \mu_0(\mu_r - 1)\frac{\partial H}{\partial t} \tag{1.5}$$

The wisdom of using ferrites to enhance radiation sources can be comprehended as either utilizing a magnetic conductor to carry the magnetic current (the loop) for radiation or use ferrites as a direct radiation sources added to the original loop. Choosing inductive ESAs will substantiate the benefits of ferrites for radiation to maximum. On the contrary, capacitive ESAs might mitigate or cannot take advantage of the positive role ferrites play in improving radiation of ESAs. After all, capacitive ESAs have totally different mechanism from inductive ones when interact with loaded materials. They work actively with permittivity, instead of permeability, of the core medium.

1.3 Two Challenges for Small Antenna Designs

No matter it is an inductive ESA or a capacitive one, there are two common major challenges in designing them. One is the physical limit mentioned at the end of the first paragraph that prevents antennas' size shrinking along with integrate circuits without the cost of its efficiency and bandwidth [8], the other is an obstacle that RF engineers frequently come across when form a system involving the participation of small antennas, called impedance matching [9].

The input impedance of ESAs are extremely hard to be matched since ESAs usually have small resistive components and large reactive components in their input impedance. Small resistance mainly comes from the metallic structure. Since the metallic structure is also physically small most of the time, no wonder the value of the resistance is small. If there are materials accompanied with the metallic structure to help radiation, the resistance of the material, resulting in power consumptions for both lost and radiating, will also contributes to the resistive part of the input impedance of the entire antenna. For large reactive components, capacitive ESAs have large capacitance, while inductive ESAs have large inductance. If the ESA is a non-self-resonant one, a driving circuit will be introduced here to create a resonance for system impedance matching. Large inductance of ESAs needs a large capacitor from the matching circuit to achieve resonance in the lower frequency band, vice versa. These capacitors or inductors are hard to be integrated with ESAs due to their enormous volume. To avoid matching circuits and create a self-resonant ESA, the size and complexity of the metallic antenna structure itself will be dramatically increased. The ESA as such can also be integrated unfriendly. For example, more turns should be added to a non-self-resonant small single loop antenna to generate a self-resonant helix antenna.

When talking about impedance matching, another concept of efficiency corresponding to impedance matching to describe the ratio between the total power to excite the antenna system and the actual power accepted by the antenna should be defined first and distinguished from the efficiency to characterize the radiating performance of the antenna, which is total efficiency E_{total} and radiation efficiency E_{rad}, respectively. The total efficiency of the antenna system is most definitely no larger than the radiation efficiency of the antenna. Small resistance of ESAs requires a large resistor in the exterior circuit to make up for the difference between 50 Ohm and the original small resistance of ESAs. There is no doubt that more power will be wasted on that resistance of the impedance matching circuit which will affect the total efficiency further.

The radiation efficiency limit on ESA relating to size starts from Wheeler [10], where antenna quality factor $Q_{rad} = \frac{\omega W}{P_{rad}}$ is rigorously defined and W is the total energy stored in the antenna. And the bandwidth-efficiency product (BWEP) is proportional to the reciprocal of Q_{rad}, as one of the important conclusions in Wheeler's paper, had been pointed out for the first time.

$$\text{BWEP} = \text{BW} \times E_{ff} \ \propto \ \frac{1}{Q_{rad}} \tag{1.6}$$

Then in 1984, L. J. Chu [8] developed an approximate expression for minimum Q_{rad}^{min} with respect to the largest physical dimension of an ESA $D_{max} = 2a$, where a is the radius of the smallest sphere that can fully enclose the ESA, through an equivalent RLC ladder network to separate the non-propagating energy from the total energy in his classic paper.

$$Q_{rad}^{min} \approx \frac{1}{(ka)^3} \tag{1.7}$$

Chu also showed in his paper that the TE_{10} mode has the lowest possible Q_{rad} for a linear polarized antenna, which is equivalent to a small loop. Another reason to select small single loop antenna to carry out the ESA design for this project.

Subsequent works on Chu's limit are conducted by J. S. McLean [11] who gives the exact expression for the minimum radiation Q_{rad} based on full wave analysis for the TM_{10} mode.

$$Q_{rad}^{min} = \frac{1}{(ka)^3} + \frac{1}{ka} \tag{1.8}$$

The bottom line is whenever comes to design efficient ESAs, the trade-off between BWEP and size miniaturization always exists.

In practical, not only the size of the small antennas but also the quality of the material used to construct small antennas also determine the radiation performance of the ESA[12]. The relationship between the quality factor of the material $Q_{material}$ and the radiation efficiency E_{rad} is derived as below:

$$Q_{material} = \frac{2\omega W}{P_{loss}} \tag{1.9}$$

$$E_{rad} = \frac{P_{rad}}{P_{rad} + P_{loss}} \tag{1.10}$$

Express E_{rad} in terms of the $Q_{material}$ and Q_{rad}, we have:

$$E_{rad} = \frac{Q_{material}}{Q_{rad} + Q_{material}} \tag{1.11}$$

As in all the power consumption other than radiation will be caused by the material whether it is metal, dielectrics or ferrites. Judging from (1.11), the higher the quality of the material is, the better radiation efficiency the ESA will achieve.

To find proper ways to resolve the impedance matching problem and approach to or even extend beyond the radiation performance governed by the Chu's limits are the motivations for antenna engineers to keep putting unremitting efforts in investigation of ESAs. This dissertation is composed under the condition that I also shares the motivation mentioned above.

1.4 Previous Attempts to the State of the Art

Besides a few methods briefly described before in the section 1.3 when pointing out the impedance matching challenge for ESA designs, like introducing external matching circuits and changing the geometry of the ESA, material loading is the most popular method for ESAs' size reduction.

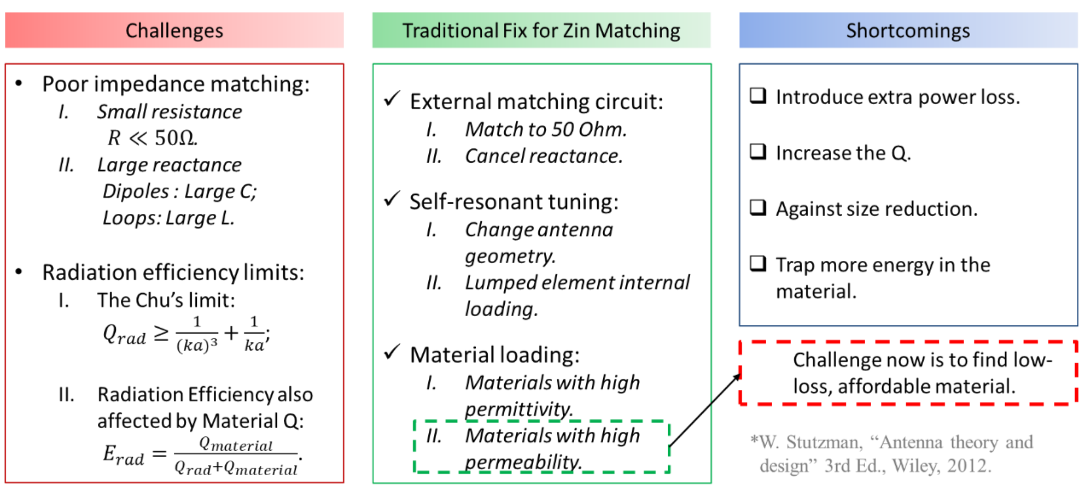

Figure 6. The summarization of challenges for ESAs, the corresponding fix and shortcomings.

The history of loading material for solving the impedance matching issue of small antennas can go way back [13] and the study of this particular area is still active [14] and prosperous due to the development of varies of materials with fancy properties which are potentially good for ESA designs.

Go back to the fundamentals of the electromagnetic theory, which are Maxwell's equations, antenna engineers realized that there are two direct ways of enhancing radiation performance, which are adding extra $\frac{\partial D}{\partial t}$ and $\frac{\partial B}{\partial t}$ to the radiation sources. Logically, loading dielectric and permeable materials separately to the metallic antenna structure becomes the first two attempts that antenna engineers tried out. With the permittivity and permeability of the loaded materials way larger than 1, electric flux D and magnetic flux B will be elevated according to the constitutive relations.

Tremendous efforts have been made to enhance the performance of ESAs by inserting materials with high permittivity or permeability into the metallic antenna structure. Based on the types of ESAs (capacitive or inductive) and material (dielectric or permeable), previous attempts to optimize the ESA design can be classified into two categories: small electric dipoles loaded with dielectrics, and small magnetic dipoles (small loops) loaded with ferrites.

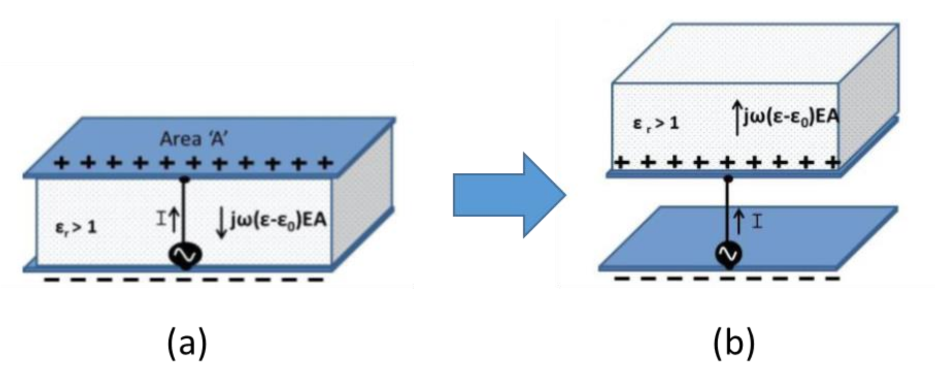

Figure 7. Two types of capacitor antennas: a) dielectrics filled in between; b) dielectrics placed above.

Two of various dielectric material loaded dipole antennas are capacitor antennas and dielectric resonator antennas.

In the 1950s, Wheeler [6] and Schelkunoff's [4] investigations into small dielectric dipoles shown in the Fig. 7 (a). However, capacitor antennas were immediately disregard by prominent engineers in this area. Because the design is to implement the dielectric material in between two dipole caps, which will have the direction of the displacement current carried by the dielectric material contradicts to the conduction current that feeds the dipole antenna. The displacement current produces radiating fields just like the conduction current and in this case, they mutually weaken each other which will leads to a poor radiation performance. Instead of locating the dielectric material inside the dipole, putting it outside like shown in the Fig. 7 (b) will aid radiation but no good to the idea of conformal design.

Most important, in 1977, a comprehensive summary of theoretical analysis and experiments by Smith [15] on these type of capacitor antennas had concluded that within the electrically small scale, it is impossible for a dielectric dipole to do better than a metallic one of the same size in radiation efficiency. This can be interpreted as a lossless small metallic dipole is an extreme special case for a small dielectric dipole when $\varepsilon'' = \frac{\sigma}{\omega} \to \infty$.

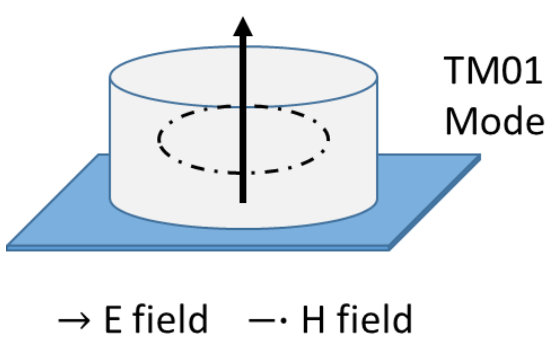

Figure 8. The most basic form of DRA.

For dielectric resonator antennas (DRA), even though they have been widely found in mobile phones and potentially efficient, their length is usually greater than $\frac{\lambda}{4}$, so technically they are not electrically small. The study of the DRA starts from the eighties with Long [16]. And not until recently, a comprehensive summary on the history of DRAs which includes the current state of the art was given by Petosa [17] in 2010. Based on years of years' research on this subject, we can summarize that DRA's operating frequency is normally way above 1GHz, commonly between 2 GHz to 40 GHz. And they are intrinsically narrowband due to the resonance of the dielectric loaded to them [3]. The most basic form of DRA is shown in the Fig. 8.

As soon as the engineers understand the limit of the dielectric loaded ESA designs, they start to look into the other way, which is the ferrite loaded ESAs, as stated before. One of the most favorable future of the ferrite loaded ESAs is that its main radiation source is the magnetic displacement current which is much less lossy, compared to the conducting current serves as the main radiation source for dielectric loaded ESAs.

The first investigation of ferrite loaded small loop antennas can be traced back to 1950s [18] when bulk ferrites, like ferrite rods, are firstly used as antenna cores to improve ESAs' performance. Rumsey [19] is the first engineer use the reaction concept to derive the expression of the radiation efficiency for an electrically small ferrite loaded multi-turn loop antenna:

$$E_{rad}^{Rumsey} = \frac{1}{1 + \frac{1 - D}{\frac{4}{3\pi^2} \cdot \frac{\pi \rho^2 l}{\lambda^3}} \cdot \frac{\mu''}{(\mu')^2}} \tag{1.12}$$

where l is the length of the ferrite rod, ρ is the radius of the ferrite rod, $\mu = \mu' - j\mu''$ is the complex permeability of the ferrite, λ is the wavelength in free space and D is the demagnetization factor. What needs to be emphasized is that the derivation is conducted under the presumption that the ferrite core possess low loss i.e. $\mu' \gg \mu''$. Without losing generality, and also to stay within the scope of the subject, the dielectric loss is ignored (real ε) here for simplicity.

Sooner after DeVore [20] derives the radiation efficiency of the same type of ESAs through radiation resistance R_{rad} and loss resistance R_{loss} perspective. The expression of E_{rad} yields as below:

$$E_{rad}^{DeVore} = \frac{1}{1 + \frac{R_{loss}}{R_{rad}}} = \frac{1}{1 + \frac{\omega \mu_0}{20k^4 l \pi \rho^2} \cdot \frac{\mu'' / \left(1 + D(\mu' - 1)\right)^2}{\left(1 + (\mu' - 1)/\left(1 + D(\mu' - 1)\right)\right)^2}} \tag{1.13}$$

where k is the wave number in the free space.

For bulky ferrite, the demagnetization factor D is approximately zero, two efficiency expressions are reduced to identical:

$$E_{rad}^{Rumsey} = E_{rad}^{DeVore} = \frac{1}{1 + \frac{\mu''}{(\mu')^2} \cdot \frac{6}{\left(\frac{\rho}{l}\right)^2 (kl)^3}} \tag{1.14}$$

Which means Rumsey and DeVore independently derived and mutually validated the relationship between the permeability of the loaded ferrites and the radiation efficiency of the ESA from two different approaches. This provides a very good example of strategy to develop new theories in the ESA design, which is verifying them from the view of both field analysis and equivalent circuit model.

After a unified expression of E_{rad} is reached, two important conclusions can be immediately drawn from (1.14):

First, increasing μ' of the ferrite rod improves ESA's radiation efficiency;

Second, reducing μ'' of the ferrite rod enhances ESA's radiation efficiency.

Basically, a standard of ferrite choosing for loaded to the ESA has been formed with these two conclusions.

Since in the traditional sense of ferrites' permeability, μ'' directly reflects the level of loss in ESA due to the ferrite. Therefore, only low loss ($\mu'' \ll \mu'$) ferrites with very large μ'can be implemented to achieve highly efficient designs of ESAs. This standard has been quickly spread and well accepted in the scientific community back then. Unfortunately, ferrites which can meet the criteria for practical use in order to reach certain level of efficiency are not available at that time. Combining the unavailability of applicable ferrites and the "unshakeable" standard, the research on ferrite loaded ESAs soon reached to a ceiling and as a result, the interest in ferrite rod ESAs decrease rapidly.

With the improvement of fabrication technique for both high-quality bulky and thin-film ferrites nowadays, interest in loading ferrites to ESAs has risen again.

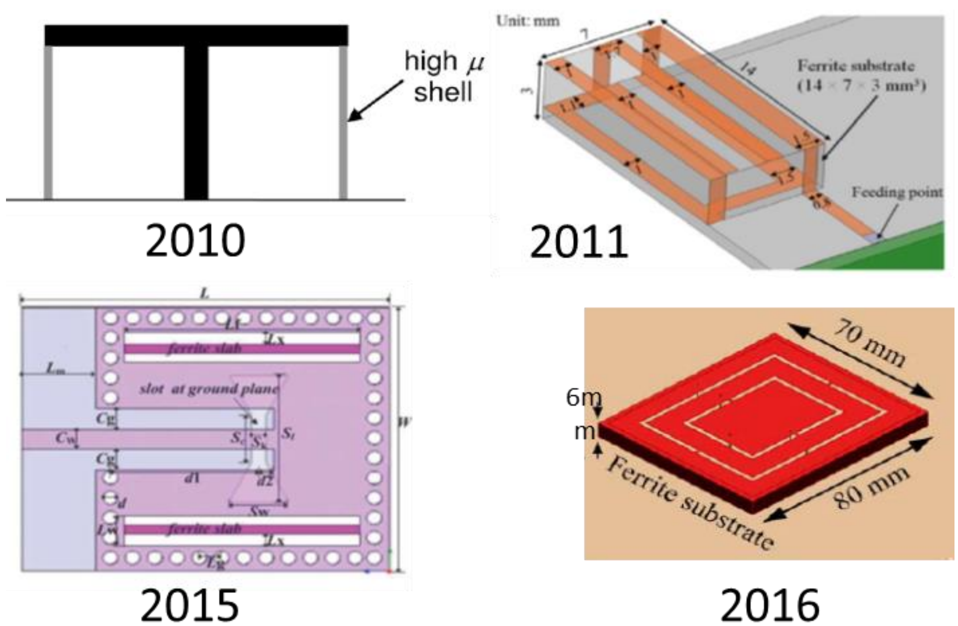

Figure 9. Four showcases of recent works on ferrite loaded ESAs.

A few recent attempts of ESA designs with novel ferrite materials are shown in Fig. 9. In 2010 [21], the effect of surrounding electrically small, top-loaded, electric-dipole antennas with a thin shell of high-permeability magnetic material was studied. And the study yields to a conclusion that the magnetic polarization currents induced in the thin shell of magnetic material reduce the internal stored energy, resulting in a lower Q as compared to conventional designs. In 2011 [22], a long-term evolution MIMO ferrite antenna was fabricated and characterized for antenna performance on ferrite substrate Ni0.5Mn0.2Co0.07Fe2.23O4. In 2015 [23], a tunable ferrite-loaded substrate integrated waveguide antennas in bowtie-shaped radiation slot is proposed to realize broad operating frequency band by simultaneously changing the location of ferrite slabs in the antennas (mechanical tuning) and bias magnetic fields (magnetic tuning). In 2016 [24], miniature low-profile multiband ferrite antennas were designed with various BaCo1.4Zn0.6Fe16O27 hexaferrite loading configurations and fabricated for telematics applications.

By reviewing more recent permeable ESA designs published within nine years from now [21]-[25], three features can be observed from but not limited to the four examples listed above:

First, most of tryouts made these days for ferrite loaded ESAs are still performed based on bulky ferrite substrates;

Second, the complex permeability of the loaded ferrite in the ESA designs is still assumed to be constant at operation frequencies;

Third, almost all efforts are made to reduce the loss (μ'') of the ferrite by either changing the geometry and feedings of the ESAs or adjusting the shape and recipe of the ferrites if not both.

In a word, the nature of the studies and designs for ferrite loaded ESAs remains the same as those in the 1970s. There is no fundamental change only persistence to the original and debatable conclusion drawn by Rumsey and DeVore.

The reason for accusing the theory, formed by Rumsey and Devore on E_{rad} with ferrites, debatable is because of the assumption they made before the derivation, which is $\mu'' \ll \mu'$. It was and still is not fair to jump to the conclusion that ferrites should be low loss when the presumption had already indicated the derivation is under the condition a low loss ferrite is involved. It is only fair when there is no constrain been posted on the permeability of the ferrite and the conclusion that ferrites should be low loss can be drawn from the equation of E_{rad}, either through field analysis or circuit modeling, which will be shown in the following chapters of this dissertation.

Nevertheless, considering the state of art about the ferrite loaded ESAs and the reasonable doubts on the derivation of the E_{rad} for permeable ESAs, I proposed a completely different approach to optimize the performance of the ferrite loaded ESAs by utilizing thin-film ferrites and the ferromagnetic resonance (FMR) generated from it under a certain amount of DC magnetic bias field. At FMR, the permeability of the ferrite is no longer constant and μ'' is extremely high. At the end of this dissertation, the design of the FMR enhanced ESAs shows great potential and incomparable advantages compared to any other attempts reported in the ferrite loaded ESA studies so far.

CHAPTER II

MOTIVATIONS AND A NEW APPROACH

2.1 A False Assumption for Ferrites Loaded ESAs

In light of recent experimental results on conformal antennas with lossy ferrite cores reaching unexpectedly high-level efficiency, Engineers like McLean [26] [27] and Hansen [28] started to question the authenticity of Rumsey's conclusion about E_{rad} and μ . In 2016, Investigators from ASU [29] [30] discarded the priori assumption made in the derivation of (1.14) and revised it only from the view of a circuit model for small permeable dipoles.

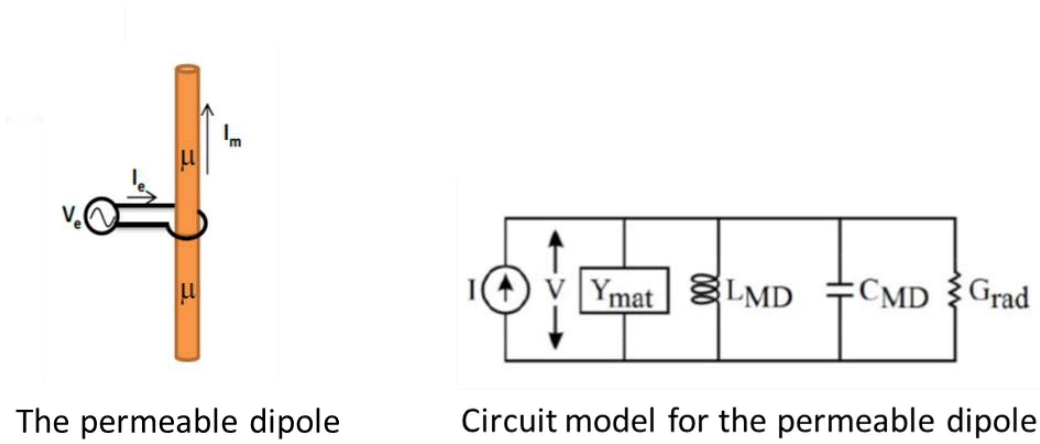

Figure 10. The physical and corresponding model of the permeable dipole.

As shown in Fig. 10, the physical permeable dipole is fed by driving electric current through a loop at its center. In its corresponding equivalent circuit model, the magnetic voltage V is corresponding to the current in the loop I_e, and the magnetic current I is the voltage at the feed of the loop V_e, so that the magnetic input impedance is just the conventional input admittance seen at the feed of the loop. In other words, according to Faraday's law:

$$\mathrm{I} = -\iint_S \frac{\partial B}{\partial t} \cdot dS = \oint_C E \cdot dl = \mathrm{V}_e \tag{2.1}$$

Where S is the area of the loop and C is the perimeter of the loop. Similarly, based on Ampere's law, we have:

$$I_e = \iint_S \frac{\partial D}{\partial t} \cdot dS = \oint_C H \cdot dl = \mathrm{V} \tag{2.2}$$

So we can have the expression for each element in the circuit model as [29]:

$$L_{MD} = \frac{\frac{\mu_0 \pi l}{2}}{\ln\left(\frac{l/2}{\rho}\right)} \tag{2.3}$$

$$C_{MD} = \frac{\varepsilon_0 l}{6} \ln\left(\frac{l/2}{\rho}\right) \tag{2.4}$$

$$G_{rad} = \frac{20\Omega (kl)^2}{\eta_0^2} \tag{2.5}$$

$$Y_{mat} = G_{mat} + jB_{mat} \tag{2.6}$$

$$G_{mat} = -\frac{1}{\frac{\omega \mu_0 \pi \rho^2}{l}} \frac{\mu''}{|\mu_r - 1|^2} \tag{2.7}$$

$$B_{mat} = \frac{1}{\omega \mu_0 \pi \rho^2 / l} \frac{\mu' - 1}{|\mu_r - 1|^2} \tag{2.8}$$

Here, again without losing generality and for simplicity, the dielectric loss (ε_r is real) is ignore during the derivation of E_{rad}. ρ and l are the radius and length of the ferrite rod.

Therefore, the power lost in the permeable antenna can be calculated as:

$$P_{loss} = \frac{1}{2} |V|^2 G_{mat} \tag{2.9}$$

And similarly, the radiating power can be obtained through:

$$P_{rad} = \frac{1}{2}|V|^2 G_{rad} \tag{2.10}$$

Substitute (2.5) to (2.10), (2.7) to (2.9) and (2.9), (2.10) to (1.10). And simply it. We have the revised and more general expression of E_{rad} in terms of μ' and μ'' for the ferrite loaded ESAs as following:

$$E_{rad}^{revised} = \frac{1}{1 + \frac{\mu''}{(\mu'-1)^2 + (\mu'')^2} \cdot \frac{6}{\left(\frac{\rho}{l}\right)^2 (kl)^3}} \tag{2.11}$$

which indicates that high E_{rad} for loaded ESAs can result from two additional combinations of the complex permeability of ferrites: 1) very large $\mu''(\mu'' \gg \mu')$, marked as Region I in Fig. 11; or 2) μ' and μ'' are comparable and both very large, marked as Region II in Fig. 11.

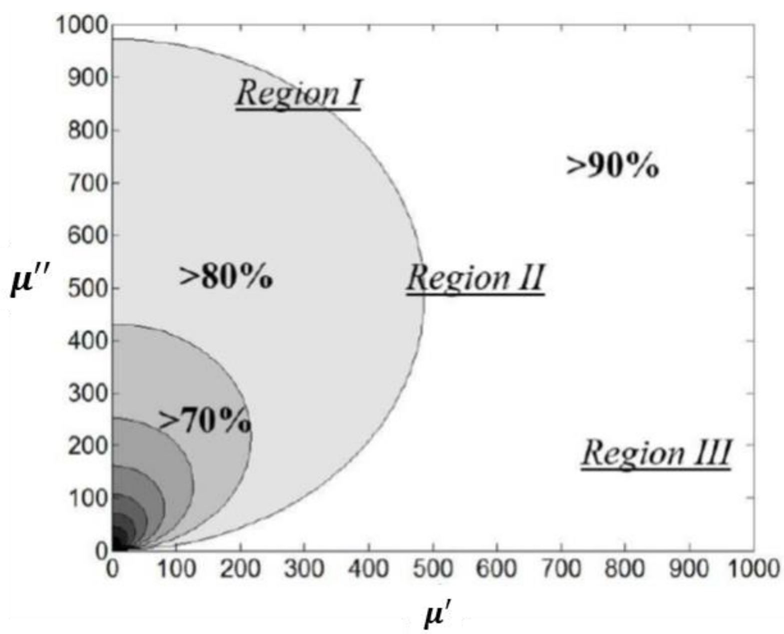

Figure 11. Contours of E_{rad} vs μ' and μ''.

As suggested before the new revised expression of E_{rad} should also be able to derived and validated through field analysis. So in this dissertation, an expression of E_{rad} similar to (2.11) will be derived in a closed form through field modeling of an ideal thin-film ferrite radiator, like [18] and unlike [20]. The agreement in form of the E_{rad} exhibited in this dissertation to (2.11) will further substantiate the situation where ferrites with very large μ'' can reach high efficiency in ESA designs. Besides, the enhancement in E_{rad} for ESAs due to large $\mu''$from the thin-film ferrite core will be realized and validated at once through a practical design of ferromagnetic resonance (FMR) enhanced ESAs.

2.2 Permeability Tensor and Ferromagnetic Resonance of Thin-film Ferrites

In the spirit of DRA, which is to utilize the resonance created through dielectrics to design ESAs, it is very nature for an antenna engineer to wonder why not use ferrite to generate resonance instead since dielectrics and ferrites have a dual relationship in the sight of electromagnetism. The answer to that question is positive. The resonance is referred here is ferromagnetic resonance (FMR). However, with the false assumption in the way before, engineers not only did not use FMR to design antenna but also intentionally avoid it [13] because at FMR, μ'' is high, which is not good in the traditional opinion of choosing ferrites. Under certain magnetization process, the ferrites can induce FMR at a much lower frequency band compared to the DRA [31], which opens the possibility of designing efficient ESA operating below 1 GHz. So before apply FMR to the actual ESA design, it is necessary to review the theoretical basis of permeability tensor and ferromagnetic resonance of ferrites [31] [32].

In free space, a simple relation hold between the magnetic field intensity $\overline{H}$ and flux density $\overline{B}$:

$$\overline{B} = \mu_0 \overline{H} \tag{2.12}$$

where $\mu_0 = 4\pi \times 10^{-7}$ henry/m is the permeability of free space. This relation is commonly known as one of the constitution relations. However, if there are media presented other than free space, the total constitution relation above will be affected by the electromagnetic fields existing in the media. For a magnetic material, applying a magnetic biasing field H_0, a magnetic polarization or magnetization $\bar{M}$ which augments the total magnetic flux, $\bar{B}$, will be produced inside. Then we have the constitution relation as:

$$\bar{B} = \mu_0(\bar{M} + \bar{H}) \tag{2.13}$$

In the preceding discussion, $\bar{M}$ is a vector in the same direction as $\bar{H}$, which means it is assumed that the material is isotropic. For more general case, which means the anisotropic materials have been included, an even more complicated constitution relation has been characterized by a rank two permeability tensor, which is given in matrix form as:

$$\bar{B} = [\mu]\bar{H} \tag{2.14}$$

, which is extended as:

$$\begin{bmatrix} B_x \\ B_y \\ B_z \end{bmatrix} = \begin{bmatrix} \mu_{xx} & \mu_{xy} & \mu_{xz} \\ \mu_{yx} & \mu_{yy} & \mu_{yz} \\ \mu_{zx} & \mu_{zy} & \mu_{zz} \end{bmatrix} \begin{bmatrix} H_x \\ H_y \\ H_z \end{bmatrix} \tag{2.15}$$

If the intensity of the biasing field increases till all the unbalanced electron spins are aligned, the material is considered to be magnetically saturated, while M_s indicates the saturation magnetization. In order to obtain the expression of $\bar{M}$ in terms of $\bar{H}$ under the condition that the material reaches magnetically saturation, the equation of motion for the magnetic dipole moments, which is the simplest form of LLG equation, needs to be derived based on the definition of torque exerted on the magnetic dipole and solved.

To derive the simplest form of the LLG equations, we start from the spin dynamic of a single electron inside the magnetic material as shown in Fig. 12. The spin of an unbalanced electron creates the magnetic dipole moment which contributes to the magnetic properties of the interested material. The expression of the magnetic dipole moment $\bar{m}$ can be given as:

$$\bar{m} = \frac{q\bar{h}}{2m_e} \tag{2.16}$$

, where $\bar{h}$ is Planck's constant divided by 2π. q is the electron charge and m_e is the mass of the electron. And the expression of a spin angular momentum $\bar{s}$ can be written as:

$$\bar{s} = \frac{\bar{h}}{2} \tag{2.17}$$

From quantum mechanical perspective, the magnetic dipole moment of an electron $\bar{m}$ and its angular momentum $\bar{s}$ has a relationship written as follow:

$$\bar{m} = -r\bar{s} \tag{2.18}$$

, where r is gyromagnetic radio. Negative sign indicates that the magnetic dipole moment has an opposite direction to its angular momentum. Comparing (2.16) and (2.17) with (2.18) gives the following relation:

$$\gamma = \frac{q}{m_e} \tag{2.19}$$

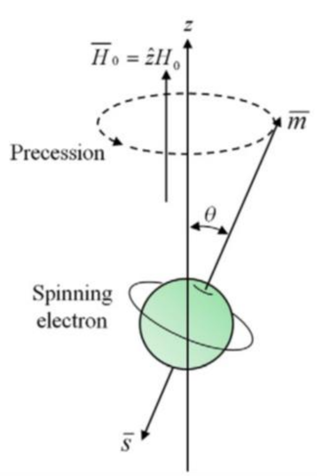

Figure 12. The spin dynamic of a single unbalanced electron.

The torque $\bar{T}$ of a single spin equals to the first order derivative of angular momentum with respect to time, we have:

$$\bar{T} = \frac{d\bar{s}}{dt} \tag{2.20}$$

The torque $\bar{T}$ that impact on the magnetic dipole can also be described as:

$$\bar{T} = \mu_0 \bar{m} \times \bar{H}_0 \tag{2.21}$$

Combine (2.20) and (2.21), we can easily build up the equation of motion for a single magnetic dipole moment as:

$$\frac{d\bar{s}}{dt} = \mu_0 \bar{m} \times \bar{H}_0 \tag{2.22}$$

Provided there are N unbalanced magnetic dipoles per unit volume, then the total magnetization contributes by these unbalanced electron spins can be calculated as:

$$\bar{M} = N\bar{m} \tag{2.23}$$

Based on the calculation of the total magnetization, the equation of motion for a single magnetic dipole moments can be easily transferred to the equation of the motion for the total magnetization of the material, which is:

$$\frac{d\bar{M}}{dt} = -\mu_0 r \bar{M} \times \bar{H} \tag{2.24}$$

When a small AC magnetic signal $\bar{H}$ interacts with the magnetically saturated material, total magnetization $\bar{M}$ and total field $\bar{H}$ can be decomposed as:

$$\bar{M}_t = M_s \hat{z} + \bar{M} \tag{2.25}$$

$$\bar{H}_t = H_0 \hat{z} + \bar{H} \tag{2.26}$$

Assumed there is a time harmonic dependence e^{jwt} in the small AC signal, substitute (2.25), (2.26) into (2.24) then the first order differential equation will be further reduced to two ordinary phasor equations. Solving them, give us:

$$(\omega_0^2 - \omega^2)M_x = \omega_0\omega_m H_x + j\omega\omega_m H_y \tag{2.27}$$

$$(\omega_0^2 - \omega^2)M_y = -j\omega_0\omega_m H_x + \omega\omega_m H_y \tag{2.28}$$

$$\bar{M} = [\chi]\bar{H} = \begin{bmatrix} \chi_{xx} & \chi_{xy} & 0 \\ \chi_{yx} & \chi_{yy} & 0 \\ 0 & 0 & 0 \end{bmatrix} \bar{H} \tag{2.29}$$

, where $\omega_0 = \mu_0 r H_0$ and $\omega_m = \mu_0 r M_s$ are called $\mathcal{Larmor}$ or $\mathcal{precession}$ frequency. $[\chi]$ is denoted as the tensor susceptibility. Compared with the constitution relation, tensor permeability $[\mu]$ can be expressed as：

$$[\mu] = \mu_0([U] + [\chi]) \tag{2.30}$$

Then the element of the tensor permeability is：

$$\mu = \mu_0(1 + \chi_{xx}) = \mu_0\mu_r \tag{2.31}$$

, where $\chi_{xx} = \frac{\omega_0\omega_m}{\omega_0^2 - \omega^2}$, which is given by turn the two ordinary phasor equations into its matrix form.

What need to emphasized here is that, to induce FMR and guarantee the best interaction between the RF signal and the magnetized ferrite, the small AC magnetic field is always applied perpendicularly to the DC magnetic bias fields as shown in the Fig. 13. And this will be the excitation setup for any simulation and measurement of FMR enhanced ESAs, involved in this dissertation from this point behind.

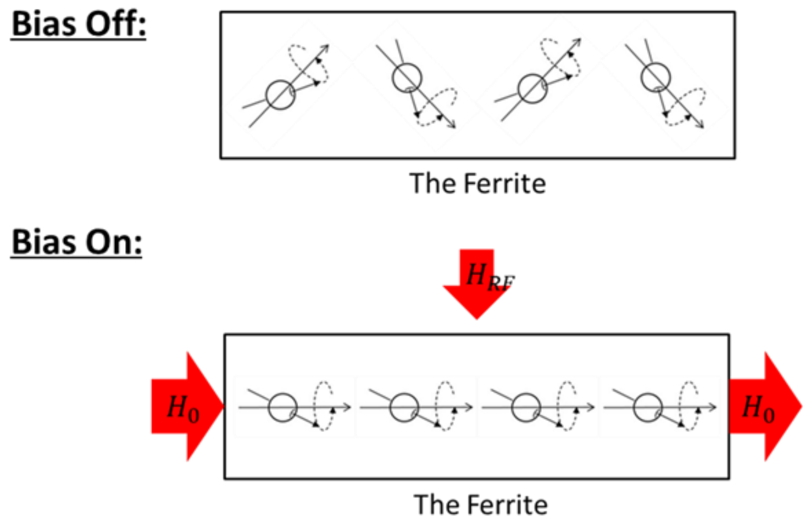

Figure 13. The dynamic of excitations to induce FMR: Bias field placed orthogonally to RF signal.

By this point, the derivation of permeability tensor for ferrite is still ideal, which means no loss is consider and any effect cause by the geometry of the ferrite is neglect. To reach a more precise prediction of how FMR is going to influence the radiation performance of the ESA and perform a meaningful field analysis of the FMR enhanced ESAs, loss in the ferrite and out of plane demagnetization effect due to the nature of the thin-film substrate must be included.

In the previous derivation of tensor permeability, it is assumed that the DC magnetic bias field external to the thin film magnetic material is the same as internal. But practically, the magnetic field stimulated inside the sample is always different from the bias magnetic field outside due to the boundary conditions at the surface of the sample. In general, the shape of the magnetic material and the orientation of the DC bias field will decide the variation between the magnetic field inside and out. To quantify this distinction, the demagnetization factor $N = N_x, N_y \; or \; N_z$ for certain direction is introduced here. And N is defined to satisfy that $N_x + N_y + N_z = 1$. So the adjusted expression of the magnetic field inside $\overline{H}$ can be written as:

$$\bar{H} = \bar{H}_e - N\bar{M} \tag{2.32}$$

Expand equation (2.32) in the Cartesian coordinate system:

$$H_x = H_{xe} - N_x M_x \tag{2.33}$$

$$H_y = H_{ye} - N_y M_y \tag{2.34}$$

$$H_z = H_{ze} - N_z M_z \tag{2.35}$$

Substitute (2.33)-(2.35) into equation (2.29) to eliminate H_x and H_y and solve for M_x and M_y:

$$M_x = \frac{\chi_{xx}\left(1 + \chi_{yy}N_y\right) - \chi_{xy}\chi_{yx}N_y}{D} H_{xe} + \frac{\chi_{xy}}{D} H_{ye} \tag{2.36}$$

$$M_y = \frac{\chi_{yy}(1 + \chi_{xx}N_x) - \chi_{xy}\chi_{yx}N_x}{D} H_{ye} + \frac{\chi_{yx}}{D} H_{xe} \tag{2.37}$$

where

$$D = (1 + \chi_{xx}N_x)\left(1 + \chi_{yy}N_y\right) - \chi_{yx}\chi_{xy}N_x N_y \tag{2.38}$$

For a finite magnetic material, at the gyromagnetic resonance frequency ω_r, D is set as 0. Substitute the expression of the element of tensor susceptibility into equation, which gives:

$$\left(1 + \frac{\omega_0\omega_m N_x}{\omega_0^2 - \omega^2}\right)\left(1 + \frac{\omega_0\omega_m N_y}{\omega_0^2 - \omega^2}\right) - \frac{\omega^2\omega_m^2}{(\omega_0^2 - \omega^2)^2} N_x N_y = 0 \tag{2.39}$$

Solve for ω, then we get the Kittel's equation as:

$$\omega_r = \sqrt{(\omega_0 + \omega_m N_x)\left(\omega_0 + \omega_m N_y\right)} \tag{2.40}$$

In the simulation and measurement of FMR enhanced ESAs, if we set the biasing field H_a is applied tangentially to the surface of the thin-film along y direction. The direction perpendicular to the surface of the thin-film ferrite is set as z direction. $H_0 = H_a - NM_y$ is the internal biasing field inside the thin-film ferrite. According to the coordination of the thin-film ferrite, we set $N_y = N_z = 0$ and $N_x = 1$, then we have:

$$\omega_r = \sqrt{\omega_0(\omega_0 + \omega_m)} \tag{2.41}$$

Rewrite χ_{xx} in terms of ω_r, we introduce the demagnetization effect to the susceptibility, as well as the permeability of the thin-film ferrite:

$$\chi_{xx} = \frac{\omega_m}{\omega_0} \cdot \frac{\omega_r^2}{\omega_r^2 - \omega^2} \tag{2.42}$$

For any resonant system, equations to describe lossless system can be easily transfer to lossy ones by introducing a damping factor α, which makes both the $\mathcal{Larmor}$ frequency and element of the tensor susceptibility complex:

$$\omega_0 \leftarrow \omega_0 + j\alpha\omega \tag{2.43}$$

$$\chi_{xx} \leftarrow \chi_{xx} = \chi'_{xx} - j\chi''_{xx} \tag{2.44}$$

The expressions of the real and imaginary part can be induced by substituting the complex $\mathcal{Larmor}$ frequency into the original χ_{xx}, then we have:

$$\chi_{xx} = \frac{\omega_m}{\omega_0} \cdot \frac{\omega_r^2}{\omega_r^2 - \omega^2 + j\alpha\omega(2\omega_0 + \omega_m)} \tag{2.45}$$

$$\chi'_{xx} = \frac{\omega_m}{\omega_0} \cdot \frac{\omega_r^2(\omega_r^2 - \omega^2)}{(\omega_r^2 - \omega^2)^2 + [\alpha\omega(2\omega_0 + \omega_m)]^2} \tag{2.46}$$

$$\chi''_{xx} = \frac{\omega_m}{\omega_0} \cdot \frac{\omega_r^2[\alpha\omega(2\omega_0 + \omega_m)]}{(\omega_r^2 - \omega^2)^2 + [\alpha\omega(2\omega_0 + \omega_m)]^2} \tag{2.47}$$

, where we have approximated $1 + \alpha^2 \approx 1$. As for most magnetic material, the loss is small.

And the damping factor α can be determined by the linewidth ΔH of the complex susceptibilities:

$$\alpha = \frac{\Delta H \mu_0 r}{2\omega} \tag{2.48}$$

So the real and imaginary part of the complex relative permeability of the magnetic material with loss can be obtained by substituting (2.46) and (2.47) into (2.31):

$$\mu_r = \mu_r' + j\mu_r'' \tag{2.49}$$

$$\mu_r' = 1 + \chi_{xx}' \tag{2.50}$$

$$\mu_r'' = -\chi_{xx}'' \tag{2.51}$$

$$\mu' = \mu_0 \cdot \left(1 + \frac{\omega_m}{\omega_0} \cdot \frac{\omega_r^2(\omega_r^2 - \omega^2)}{(\omega_r^2 - \omega^2)^2 + [\alpha\omega(2\omega_0 + \omega_m)]^2}\right) \tag{2.52}$$

$$\mu'' = \mu_0 \cdot \frac{\omega_m}{\omega_0} \cdot \frac{\omega_r^2[\alpha\omega(2\omega_0 + \omega_m)]}{(\omega_r^2 - \omega^2)^2 + [\alpha\omega(2\omega_0 + \omega_m)]^2} \tag{2.53}$$

Plot the complex permeability of YIG vs frequencies under two different biases as shown in Fig. 14. Two sharp spikes clears show resonance effect. The FMR frequency can be well predicted by Kittel's equation (2.41). Both extremely high μ' and μ'' happen around FMR.

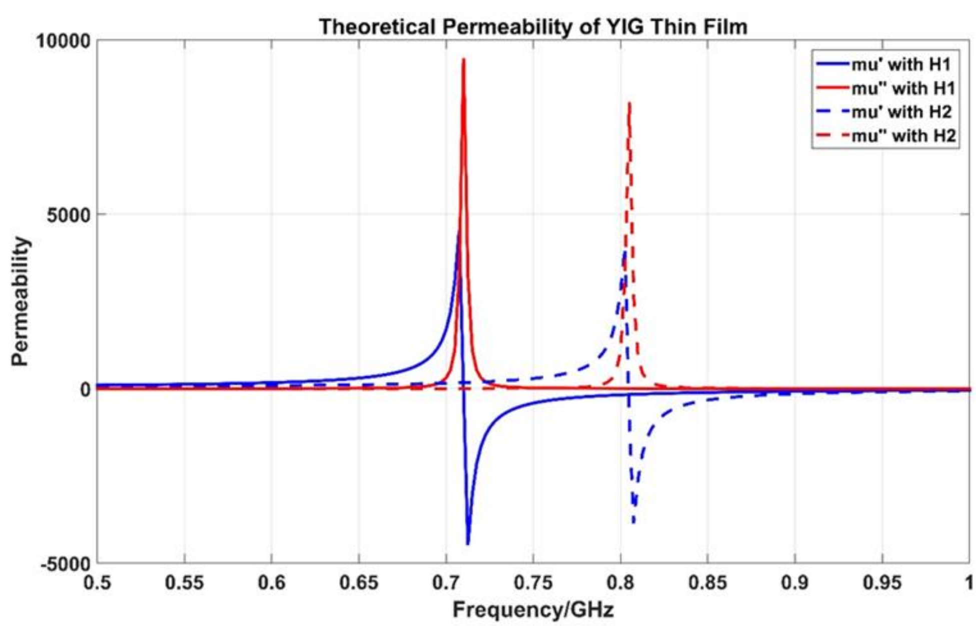

Figure 14. The permeability of thin-film YIG under two different biases.

To conclude, FMR arises from the precessional motion of the magnetization in ferrites under an external magnetic bias field. At FMR, ferrites will interact the strongest with the magnetic field induced by the RF signal, which is applied perpendicularly to the bias field. The precession of the electrons are described by the LLG equation. And the effect due to the precession will be reflected in ferrites' permeability, which is planned to be taken advantage of in the ESA design.

2.3 A New Approach for Ferrite Loaded ESA Designs

Considering the state of the art, most of the studies and realizations of permeable ESAs are still based only on bulky ferrites [23]-[25]. Thin-film ferrites have been wildly utilized in RF circulators and isolators, but not successful in radiators [32], because of its strong magnetic anisotropy when certain DC magnetic bias fields are applied as shown in the Fig. 15. But other distinct properties of thin-film ferrites, such as high in-plane permeability and FMR frequency due to the out-of-plane demagnetization effects, do make them perfect candidates to use in the design of loaded ESAs according to (2.41). Recently there are some micro strip patch ESA design integrated with thin-film ferrites [25] [33], however, the design and performance are not optimized.

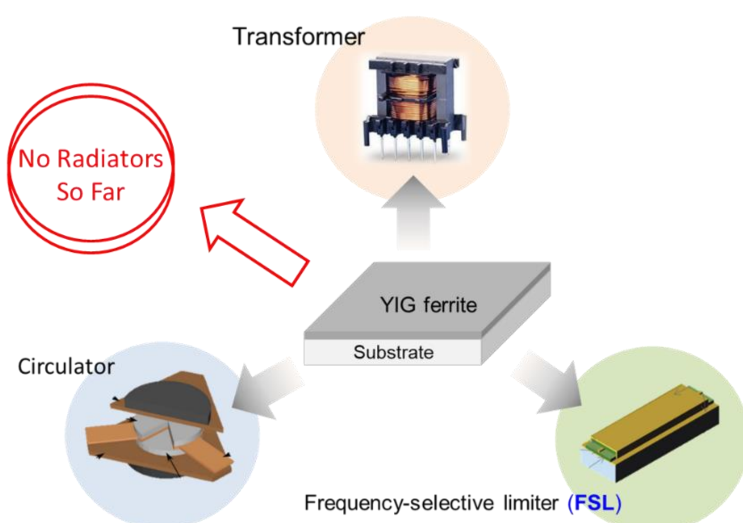

Figure 15. An exhibition of some common applications based on thin-film YIG.

In early studies of ferrite rod antennas, the permeability of ferrite cores was considered to be constant. Engineers in [29] did include two classic frequency-dependent susceptibility models in analysis when specify the material selection rules for penetrable antenna cores, but their antenna prototype was not designed to operate in the bandwidth where resonance shown in the two classic models for susceptibility was involved. So the role that resonance plays in affecting ESA's performance was not examined. Besides, the antenna fabricated in [29] [30] is still physically large. Even though more and more modern studies [24] [33] of ferrite loaded ESAs has started to take the dispersive behavior of ferrites' permeability into account, the nature of using high μ' and avoiding high μ'' or resonance for the ESA design remains the same. This dissertation proposes for the first time to combine the merits of thin-film ferrites and FMR in the design of ESAs.

FMR provides a unique advantage in improving impedance matching for ESAs. The resonance in Z_{in} of FMR enhanced ESAs will be generated directly from the thin-film ferrite. Because the magnitude and bandwidth of impedance resonance are independent of the ESAs' metallic parts, and solely determined by the properties of the core material, FMR provides extra room for geometry simplification and size reduction of ESAs. The external matching circuit is no longer needed either, which prevents unnecessary power loss being added into the design. Also, the FMR frequency f_0 can be controlled through changing the strength of DC magnetic fields H_0 applied perpendicularly to the RF signal. The adjustability of the FMR frequency also makes FMR enhanced ESAs tunable antennas, which compensates, to a certain degree, for the shortcoming of ESAs normally being narrowband. Additionally, the large μ' and μ'' of the thin-film ferrite around FMR frequency will produce a stronger magnetic flux to enhance the radiation performance of loaded ESAs. This is because the magnetic moments from the orbital and spin of electrons in the ferrite interacts strongest with RF signal at the FMR frequency and serves directly as part of radiating sources. Additionally, with the presence of the thin–film ferrite in the ESA, the antenna will have better immunity to the ground plane effect at FMR, which will be elaborate in details in Chapter III.

It is obvious that thin-film ferrites are better choice than bulky ones for designing FMR enhanced ESAs. Smaller volume, higher permeability magnitude and FMR frequencies than those of bulky ferrites under the same DC magnetic bias are evidently assets of thin-film ferrites for the design of ESAs. The thin-film ferrite used in the dissertation is yttrium iron garnet (YIG).The reason for me to choose YIG is because it has better properties than the other ferrites tested in [34] including lower loss in the microwave frequency region and it is also easily acquired on the market.

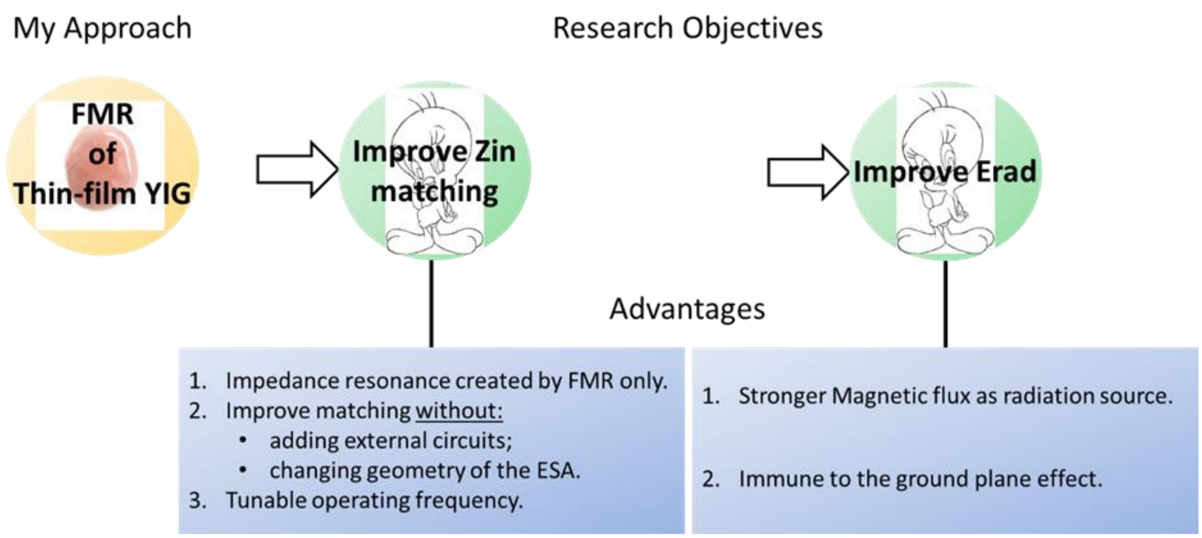

Figure 16. The proposed approach to solve two major challenges in ESA designs simultaneously.

To summarize and clarify the goals and the approach of my PhD dissertation, I would like to emphasize that the method and idea proposed in this paper is to load a thin-film YIG substrate into a metallic ESA and use the FMR generated from the ferrite core to improve the impedance matching ability and radiation efficiency of the ESA simultaneously. The size of the ESA will be extremely minimized to the millimeter level at an operating frequency tunable between 0.5 GHz and 1 GHz, which is not only electrically small but also physically small.

2.4 Strategies and Structures of the Study

Field theory analysis, equivalent circuit models, and radiation pattern integration (mostly for Arrays), are three most common approaches to investigate ESA. I intend to use them all if applicable here to reach an effect of mutually assurance. Strategy wise, the final design of the FMR enhanced ESA presented in this dissertation is built, modeled, optimized and validated in four ways, which is shown in Fig. 17. The theory of high $\mu^{"}$ can actually help improving the radiation efficiency of ESAs is first examined through modeling an ideal thin-film ferrite radiator and realized it in HFSS to check the robustness of this physics model. During the process, the accuracy of the circuit model for thin-film ferrites in characterizing ferrite antenna parameters is also verified. Then, the conducting structure of the FMR enhanced ESA as a novel single loop antenna is designed and used to compare the full-wave simulation results with and without thin-film YIG loaded. Multi-turn loop antennas as the conducting structure of the FMR enhanced ESA is also tried out to check the impact of the number of turns to the optimization effect by FMR and determine the best conducting structure for the ESA discussed in this dissertation. To provide effective guidance for optimizing the design of FMR enhanced ESAs in the future and to give detailed explanation about why the conducting structure determined in Chapter IV is better than any other geometry mentioned in this dissertation, a novel circuit model for small loop antennas and a comprehensive circuit model for FMR enhanced ESAs are developed. Eventually, prototypes based on designs simulated in HFSS for single and two-turn small loop antennas enhanced by FMR are fabricated and tested for final validation.

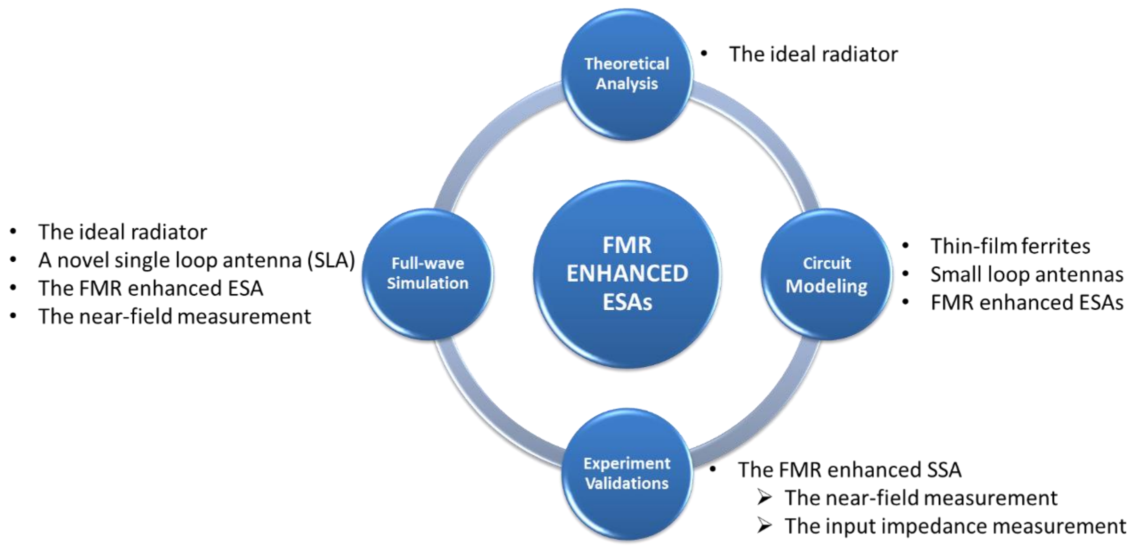

Figure 17. Strategies and the logic to design FMR enhance ESAs.

In Chapter III, the expression of E_{rad} is obtained from modeling an ideal radiator, which consists of an infinitely large thin-film ferrite backed with a ground plane, based on assumed field distributions inside the material. The ideal radiator with thin-film YIG is simulated in HFSS. The equivalent circuit model for this ideal radiator is structured by importing the RLC tank for spin motion [35]. Radiating power calculated through the physics model, the full-wave simulation and the circuit model are compared to validate the accuracy of the physics model and the spin-motion circuit model in characterizing ferrite antenna parameters. The ground plane effect isolation due to the presence of thin-film ferrite is elaborated through image theory.

In Chapter IV, an FMR enhanced ESA is designed in the form of a modified, stripe-pattern small single loop accommodating a YIG thin-film. The input impedance Z_{in} and radiation efficiency E_{rad} of this ESA with and without thin-film YIG loaded are simulated in HFSS and compared. The theory arisen from Chapter III will be verified by this practical design of an FMR enhanced ESA. Improvements in ESA's performance due to FMR can be clearly observed from the full-wave simulation results. Multi-turn stripe-pattern loop antennas are also examined in HFSS for the purpose of optimizing the design of the conducting structure. However, it turns out to be that the less turn, the better.

In Chapter V, a few existing and popular models for ESAs are checked and compared. A novel, frequency-independent equivalent circuit model for small magnetic dipoles is developed by means of re-examining the E-field component of an ideal small loop. The new circuit model is able to predict Z_{in} and E_{rad} of magnetic ESAs to the first self-resonance frequency. A comprehensive, lump-element equivalent circuit model for FMR enhanced ESAs is formed by introducing the RLC tank for spin motion to the new circuit model for small loops. The two circuit models are both validated by comparing full-wave simulations with circuit calculations for Z_{in} and E_{rad} respectively. Reasons for why the single-turn, strip-pattern, loop antenna structure can achieve the best improvement in radiation performance for FMR enhanced ESAs are given from the view of the newly developed circuit model.

In Chapter VI, prototypes are fabricated and displayed based on the design in Chapter IV. Setups for conducting impedance and communication link measurements (S parameters) of prototypes are demonstrated. Full-wave simulations for S parameter measurements are performed. Adjustments are made to the HFSS models in Chapter IV to mimic the exact environment of measurements based on the look of actual prototypes. The close matches between HFSS simulations and measurements show the feasibility of the idea discussed in this dissertation and the correctness of the relationship between FMR and the enhancement of radiation performance and impedance matching.

In chapter VII, a complete summary of all achievements presented in this dissertation is given.

CHAPTER III

MODELS FOR AN IDEAL THIN-FILM RADIATOR

3.1 The Physics Model for Field Analysis

Examining an ideal, simplified thin-film ferrite radiator yet containing all essential characteristics pertaining to FMR enhanced ESAs is the pre-step to take for the purpose of theory validation before moving on to the actual design.

To derive the expression for E_{rad} and authenticate the role of large μ'' in radiation improvement, an infinitely large ferrite film with thickness h is mounted on a PEC plane as shown in Fig.18. A uniform electric current sheet with the density J is placed on the top surface of the ferrite film to excite the model for radiation. Since the planar dimensions (along x and y axes) of this ferrite film are of infinity, the model fits strictly to the definition of thin-film radiators. The thickness h is also supposed to be much smaller than the wavelength (kh ≪ 1), which makes the model count as a 1D electrically small radiator, observed along z axis.

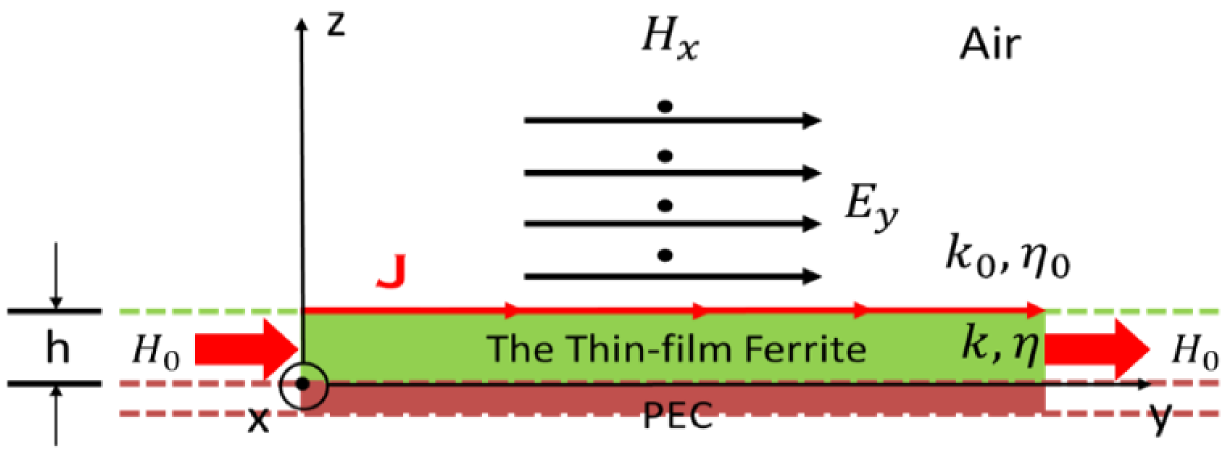

Figure 18. The physics model for the ideal radiator.

With the premises now established on the physical size and excitation of the model, as well as the enforcement on field distributions cast by boundary conditions at the interface between the thin-film ferrite and PEC plane, electromagnetic (EM) waves inside the ferrite approximately propagate in a plane-wave fashion, and their magnitude roughly decays linearly with respect to the z axis. Therefore, the expressions of the field components along the z axis can be written as follows:

For $z < h$,

$$E_y = E_0 \, sin(kz) \approx E_0 kz \tag{3.1}$$

$$H_x = -E_0/j\eta \, cos(kz) \tag{3.2}$$

For $z \geq h$,

$$E_y = E_0 si\,n(kz)\, e^{-jk_0 z} \tag{3.3}$$

$$H_x = -E_0/j\eta_0 \, co\,s(kz)\, e^{-jk_0 z} \tag{3.4}$$

where $k = \omega\sqrt{(\mu' - j\mu'')\varepsilon}$ is the propagation constant inside the thin-film ferrite, and $\eta = \sqrt{(\mu' - j\mu'')/\varepsilon}$ is the intrinsic impedance of the ferrite. Without losing generality, and also to stay within the scope of this paper, the dielectric loss is ignored (real ε) here for simplicity. In this way, the power loss P_{loss} and stored energy W_H of the model is mainly magnetic ($W_E \ll W_H$). So the radiating power P_{rad}, P_{loss} and W_H can be calculated as below:

$$W_H = \frac{1}{2} \iiint\limits_{z<h} \mu' |H|^2 \, dv \approx \frac{1}{2} \mu' |H|^2 hS = \frac{1}{2} \mu' \frac{E_0^2}{\left| \sqrt{\frac{(\mu' - j\mu'')}{\epsilon}} \right|^2} hS \tag{3.5}$$

$$P_{rad} = \frac{1}{2\eta_0} \iint_{z>h} \left|E_y\right|^2 ds \approx \frac{1}{2} E_0^2 h^2 S \omega^2 \varepsilon |(\mu' - j\mu'')| / \eta_0 \tag{3.6}$$

$$P_{loss} = \frac{1}{2}\omega\mu'' \iiint_{z<h} |H_x|^2 dv \approx \frac{1}{2} E_0^2 hS\omega\varepsilon\, \mu''/|\mu' - j\mu''| \tag{3.7}$$

where S is the area of the ferrite surface along the x-y plane, which has been pushed to infinity in this case. The quality factor Q_{total} and Q_{rad} can be calculated respectively as:

$$Q_{total} \approx \omega \frac{W_H}{P_{rad} + P_{loss}} = \frac{1}{\frac{h\omega}{\eta_0}\frac{\mu'^2 + \mu''^2}{\mu'} + \frac{\mu''}{\mu'}} = \frac{\mu_r{}'}{hk_0(\mu_r'^2 + \mu_r''^2) + \mu_r''} \tag{3.8}$$

$$Q_{rad} \approx \omega \frac{W_H}{P_{rad}} = \frac{1}{\frac{h\omega}{\eta_0}\frac{\mu'^2 + \mu''^2}{\mu'}} = \frac{\mu_r{}'}{hk_0(\mu_r'^2 + \mu_r''^2)} \tag{3.9}$$

Hence, the radiation efficiency for this ideal radiator can be defined by:

$$E_{rad} = \frac{P_{rad}}{P_{rad} + P_{loss}} = \frac{Q_{total}}{Q_{rad}} = \frac{1}{1 + \frac{\mu''}{(\mu')^2 + (\mu'')^2} \cdot \frac{1}{k_0 h}} \tag{3.10}$$

Comparing (3.10) with (2.11), two similar expressions sharing the term $\mu''/(\mu')^2 + (\mu'')^2$ in the denominator of e_{rad} suggests that high radiation efficiency will be achieved under the same three circumstances regarding the complex permeability of the thin-film ferrite, mentioned in [29] and [30]: 1) high μ' and low μ''; 2) low μ' and high μ''; 3) comparably high μ' and μ''. The different scaling factors in (3.10) and (2.11), $1/k_0 h$ and $6/[(\rho/l)^2(kl)^3]$ respectively, are due to discrepancies in the geometry of the two ferrites (film vs cylinder) and the corresponding conducting structures (sheet vs loop) in [29] [30] and this dissertation, which is trivial for determining the impact of μ'' on the radiation efficiency of ESAs.

After applying a uniform H_0 to the thin-film ferrite layer along y axis as shown in Fig. 18, FMR can be induced inside this ideal radiator. Around FMR frequency, μ' and μ'' of the ferrite are no longer independent, the expressions for both of them can be obtained by solving the LLG equation along with the out-of-plane demagnetization and damping effect taken into consideration, which have already been listed in Chapter II.

Define $f(\mu) = \mu''/(\mu')^2 + (\mu'')^2$, then we have:

$$(\mu')^2 + \left[\mu'' - \frac{1}{2f(\mu)}\right]^2 = \left[\frac{1}{2f(\mu)}\right]^2 \tag{3.11}$$

According to (2.52) and (2.53), we have:

$$\mu'' = \mu' \frac{\left[\dfrac{\alpha\omega(2\omega_0 + \omega_m)}{\omega_r^2}\right]}{\left[1 - \left(\dfrac{\omega}{\omega_r}\right)^2\right]} \tag{3.12}$$

Substitute (3.12) into (3.11) and solve for μ', we get:

$$\mu' = \frac{\dfrac{\dfrac{\alpha\omega(2\omega_0 + \omega_m)}{\omega_r^2}}{1 - \left(\dfrac{\omega}{\omega_r}\right)^2} \cdot \dfrac{1}{f(\mu)}}{1 + \left\{\dfrac{\dfrac{\alpha\omega(2\omega_0 + \omega_m)}{\omega_r^2}}{1 - \left(\dfrac{\omega}{\omega_r}\right)^2}\right\}^2} \tag{3.13}$$

Compare (3.13) and (2.52), we realize:

$$f(\mu) = \alpha\omega \cdot \frac{\omega_0}{\omega_m} \cdot \frac{2\omega_0 + \omega_m}{\omega_r^2} \tag{3.14}$$

So the expression of E_{rad} is revealed as:

$$E_{rad} = \frac{1}{1 + \alpha\omega \cdot \dfrac{\omega_0}{\omega_m} \cdot \dfrac{2\omega_0 + \omega_m}{\omega_r^2} \cdot \dfrac{1}{k_0 h}} \tag{3.15}$$

From (3.15), it is pretty clear that the enhancement of E_{rad} for this ideal radiator from FMR is solely dictated by the damping fact α of the thin-film ferrite when the strength of the magnetic bias and the geometry of the ferrite are fixed.

3.2 The Geometric Model for Full-wave Simulations

The robustness of the physics model for delineating the relationship between radiation enhancement and the presence of thin-film ferrites can be readily verified using a commercial full-wave EM simulator i.e. HFSS.

In HFSS, this infinitely large radiator is replicated through a flat square unit cell with periodic boundaries vertically attached to all its edges in the x-y plane as shown in Fig.19, with dimensions of $5\text{mm} \times 5\text{mm} \times 3.08\mu\text{m}$. The thickness of the unit cell has been deliberately set to match that of the ferrite layer on the actual thin film applied to the prototype of the FMR enhanced ESA to be discussed in Chapter VI.

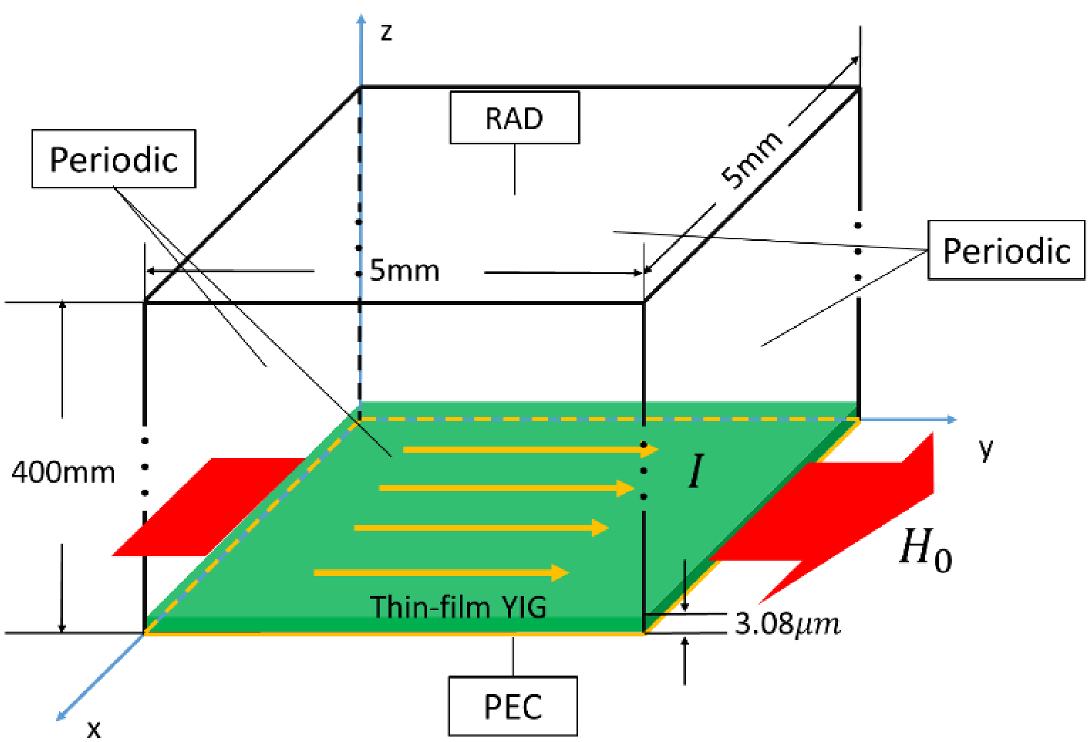

Figure 19. The HFSS model for the ideal radiator.

Hence, the parameters of YIG [36], i.e. $4\pi M_s = 1750\,Gauss$, $\Delta H = 5\,Oersted$ (linewidth), $\varepsilon_r = 13$ are assigned to the thin-film unit cell. According to [37], HFSS will solve Maxwell's equations inside the unit cell with YIG's complex permeability following the dispersive pattern of Polder's tensor. A surface current I_0 of 1A is assigned on top of the unit cell along the y axis for excitation. The thin-film cell is also magnetized by an in-plane $H_0 = 36\,Oe$ parallel to the surface current so that FMR will appear near $f_0 = 0.7\,GHz$, known from equation (2.41). To evaluate the power radiating from the model to the far-field region over the spectrum of 0.5 to 1 GHz, the unit cell is placed on the bottom surface of a vacuum simulation region with dimensions of $5\text{mm} \times 5\text{mm} \times 400\text{mm}$ at $\text{z} = 0$. The bottom surface is assigned with a PEC boundary, while a radiation boundary is allocated to the top surface of this vacuum region at z = 400mm. Four sidewalls embedded with periodic boundaries force the exciting current to be uniform. The simulation result of the HFSS simulation are exhibited and analysis in section 3.4.

3.3 Circuit Models for Thin-film ferrites and The Ideal Radiator

As planed in the strategy section, the ideal radiator should also be modeled by an equivalent circuit. However, before constructing the circuit model for the ideal radiator, a simple but elegant model to only present the thin-film ferrite is needed.

In [35], a physics-based equivalent circuit model for the spin motion of electrons inside thin-film ferrites was developed, which was then applied successfully to model the response of frequency-selective limiters.

This linear behavior circuit model for thin-film ferrites is derived from the simplest structure that can induce FMR inside a thin-film ferrite and also be used to measure the complex permeability in practical, which is a one-port strip line permeameter mentioned in [38] and indicated in Fig. 20. The logic behind this method is to compare the difference between the input impedance or reflection coefficient with and without thin-film ferrite present.

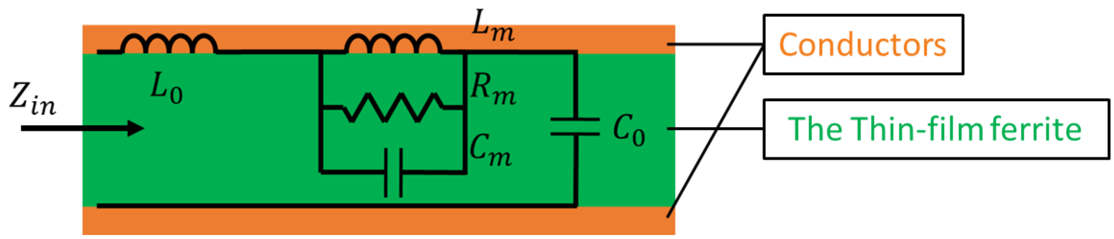

Figure 20. Illustration of the equivalent circuit of the thin-film ferrite corresponding to the parallel plate micro strip line structure.

According to the well-known equivalent circuit model for micro strip lines described in [32], the inductance L_0 and capacitance C_0 per unit length of micro strip lines are listed as below:

$$L_0 = \mu_0 \mu_r \frac{h}{w} \ (H/m) \tag{3.16}$$

$$C_0 = \varepsilon_0 \varepsilon_r \frac{w}{h} (F/m) \tag{3.17}$$

Focus on the inductance part of the input impedance. This is because that the thin-film ferrite that completely fills the space between the parallel-plate micro strip line will contributes to the input impedance of the whole structure through its susceptibility and mainly changes the inductance part of Z_{in}, so:

$$\mathrm{Z_{thin\_film}} = j\omega L = j\omega\mu_0 \left(\chi' - j\chi"\right) \frac{h}{w} \tag{3.18}$$

As shown before in Fig. 14, the permeability (real and imagine) of the thin-film ferrite has the same pattern with the input impedance (imagine and real) of a parallel connected RLC tank. Besides, at the resonance the resistance part of the input impedance reaches to maximum, which will be shown in the later simulation results of the FMR enhanced ESA, also suggests the resistance in the RLC tank should be connected in the way shown in Fig. 20.

After determine the structure of the equivalent circuit model, we relate the expression of the input impedance of the RLC circuit block to Kittel's equation and solve for C_m, L_m and R_m, we have:

$$\mathrm{Z_{RLC}} = \frac{1}{\frac{1}{R_m} + \frac{1}{j\omega L_m} + j\omega C_m} \tag{3.19}$$

$$\frac{Z_{RLC}}{j\omega\mu_0} = \frac{1/\mu_0}{\left(\frac{1}{R} + \frac{1}{j\omega L} + j\omega C\right) j\omega} = \frac{\frac{1}{\mu_0} \cdot \frac{1}{C_m}}{\omega_r^2 - \omega^2 + \frac{j\omega}{R_m C_m}} \tag{3.20}$$

Compare (3.19) and (3.20), then,

$$C_m = \frac{\omega_0}{\omega_r^2 \mu_0 \omega_m} \cdot \frac{w}{lh} \tag{3.21}$$

$$L_m = \frac{\mu_0 w_m}{\omega_0} \cdot \frac{lh}{w} \tag{3.22}$$

$$R_m = \frac{\mu_0 \omega_m \omega_e^2}{\alpha(2\omega_0 + \omega_m)\omega_0} \cdot \frac{lh}{w} \tag{3.23}$$

Where the length, width, and thickness of the thin-film ferrite are l, w, h, respectively. In this case, the corresponding sizes of the unit cell and parameters of YIG in HFSS will be substituted into (3.21), (3.22), and (3.23) to determine the value of each element in RLC tank for the radiation power calculation.

At this point, the derivation of the equivalent circuit model for the thin-film ferrite has been established.

In order to test the transferability of this circuit model and also in preparation for developing a comprehensive equivalent circuit model to accurately predict the input impedance and radiation efficiency response of FMR enhanced ESAs later in Chapter V, a circuit model is constructed here based on the geometry of the ideal radiator where the spin-motion circuit model is implemented to represent the thin-film ferrite, as shown in Fig. 21. Along the traveling directions of the magnetic fields in the physics model, which corresponds to the direction of current flows in the circuit, a steady current source and radiation resistance R_{rad} are added and connected in parallel with the RLC tank to form the equivalent circuit for the infinitely large thin-film radiator.

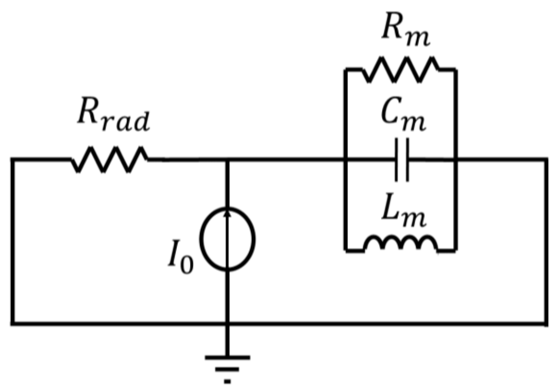

Figure 21. The circuit model for the ideal radiator.

The value for each element in the circuit model for this ideal radiator is shown in TABLE I. As mentioned in [35], a single RLC resonator has its limitation to represent all properties of thin-film ferrites, only those with uniform precessions. Factors, which include exchange coupling between spins, non-uniform field distributions in antenna structures, infinite volume and so on, can alter the values of R_m, L_m and C_m. In this paper, the initial values of the circuit model are first calculated by analytical or empirical equations, and then further optimized by using the differential evolution (DE) algorithm to curve-fit the circuit model calculation with the HFSS simulation results. Developing more sophisticated circuit models to fully model thin-film ferrites for ESA designs will be discussed in future publications.

TABLE I
CIRCUIT MODEL PARAMETERS

Symbol	Quantity	Value
R_{rad}	radiation resistance	120π Ω
R_m	effective resistance of the thin-film YIG	163.53 Ω
L_m	effective inductance of the thin-film YIG	0.1882 nH
C_m	effective capacitance of the thin-film YIG	0.2671 nF

Table 1. Parameters of the circuit model for the ideal radiator.

3.4 Result Comparisons among All Three Models

Plot the radiation power of the physics model for the ideal radiator calculated based on equation (2.41) under three different bias magnetic fields, which are 36 Oersted (Oe), 41 Oe and 48 Oe, vs frequency along with the complex permeability as shown in Fig. 22.

It is obvious that three peaks in the radiation power of the ideal radiator at three different FMR frequencies, as expected, align with three resonances in the real and imaginary part of the complex permeability of the thin-film ferrite, which indicates FMR can improve the radiation performance. Three peaks in μ'' matches three peaks in the radiation power specifically proves that extremely high μ'' can be a good thing to the ESA design, which agrees with the conclusion drawn by engineers from ASU. In the Fig. 22, it appears that at FMR, μ''can go as high as 4200 and the magnitude of the narrow peak at each FMR frequency is about 18W. Radiation power decays from f_0 and reaches almost zero at both ends of the observing frequency band due to strong cancellation from the image source of I_0 against PEC.

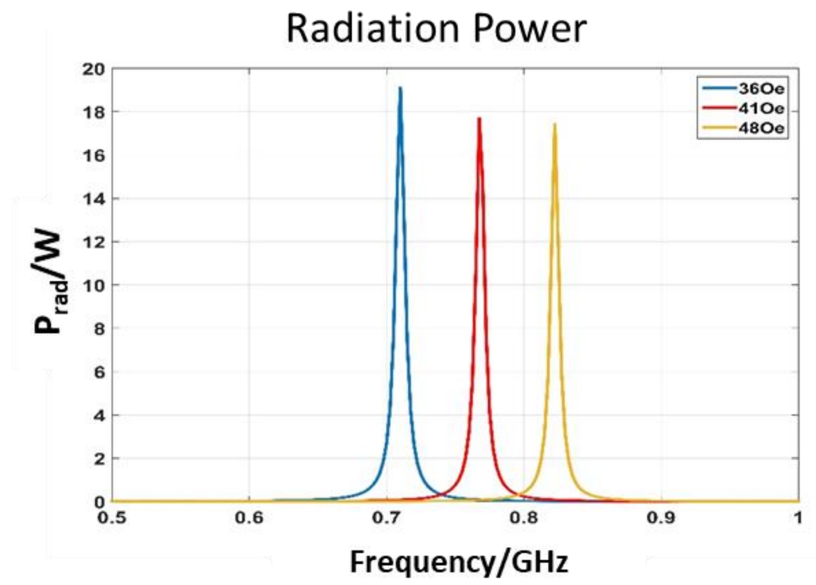

(a)

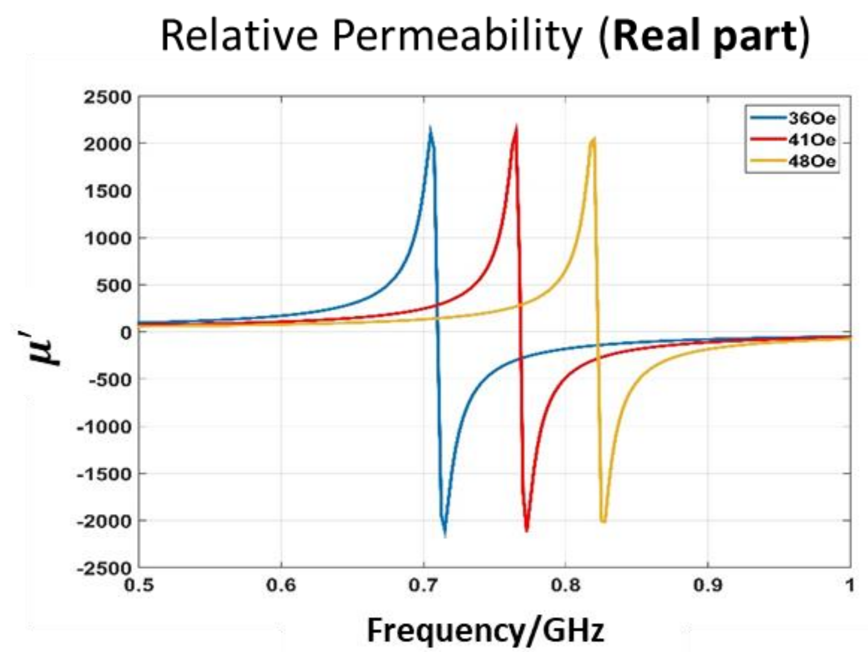

(b)

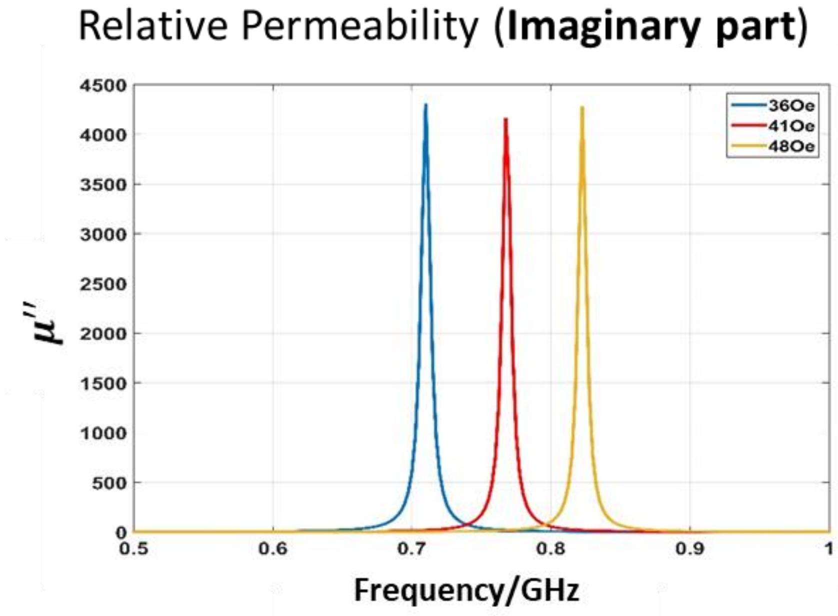

(c)

Figure 22. Comparisons between the permeability (b) and (c) of the thin-film ferrite and (a) the radiation power at three different FMR frequencies.

A physical explanation for the radiation enhancement from FMR of the thin-film ferrite can be stated as follow: at FMR frequency, μ'' is extremely high. The thin-film ferrite is no longer trapping energy inside, instead more EM fields will be pushed to the surface of the ferrite and it will function as a magnetic conductor. Like large ε''can be converted to large σ, i.e. $\varepsilon'' = \sigma/\omega$; large μ'' can be translated to large σ_m by $\mu'' = \sigma_m/\omega$. Taking the augment of ε'' and μ'' to infinity, it is a well-known fact that a small dipole made of PEC is lossless and its radiation efficiency approaches 100%. Analogously, a small dipole made of PMC is also lossless with 100% radiation efficiency. In this particular scenario where a PEC ground plane is located closely to the exciting conduction current, another benefit for the thin-film ferrite with infinitely high μ'' (PMC) placed in between the excitation and the PEC ground plane is to flip the image source of the conduction current from an opposite direction to the same one with the original source. Then radiation power should be boosted, as the equivalent radiation sources have been doubled as shown in Fig.23.

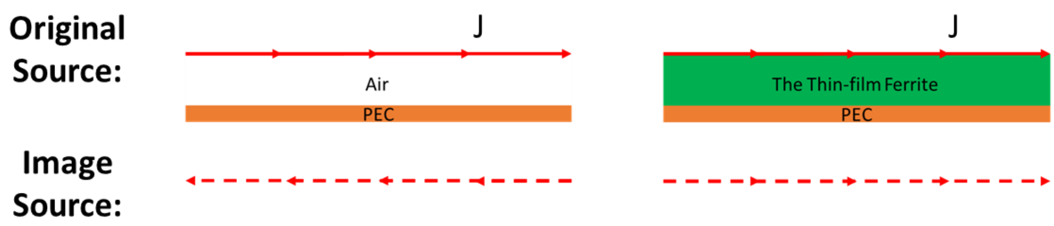

Figure 23. The change in the direction of the image source due to the presence of the thin-film ferrite at FMR frequencies.

On the other hand, the appearance of high μ' close to FMR indicates a strong involvement of the magnetic moments of electron spins in radiation as extra radiation sources, besides just conduction currents. As a result, a larger magnetic flux is induced to improve radiation.

Fixed the Bias field at 36 Oe, and plot the radiation power simulated through the HFSS model mentioned in the section 3.2 and that predicted by the newly developed circuit model in Fig. 21 together with the previous theoretical calculation of it all in Fig. 24. The perfect match among results generated from all three models developed so far verifies the authenticity of them and the feasibility of using FMR produced by thin-film ferrite core to design high efficient ESAs.

After the theory has been proved to be sound, the process of creating the actual design for FMR enhanced ESA can be created.

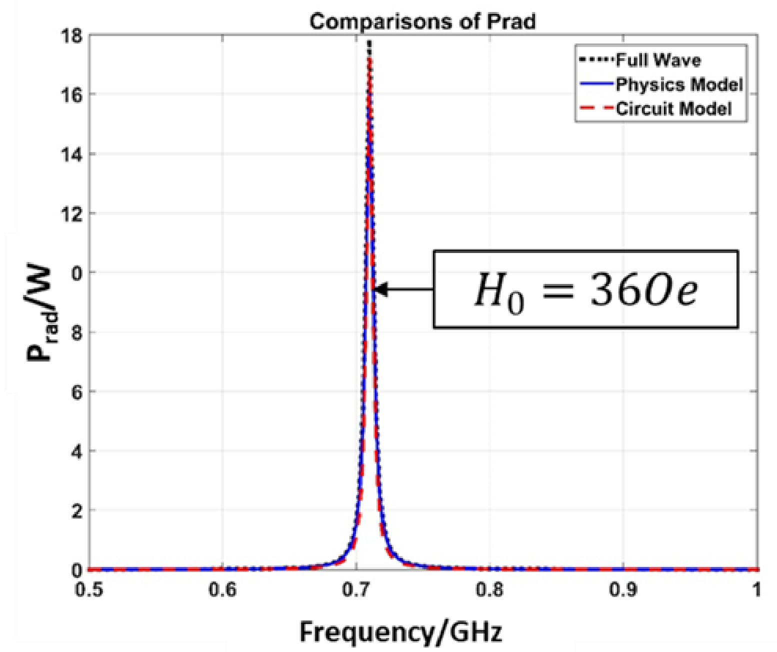

Figure 24. Radiation power comparison of the unit cell: HFSS vs Circuit model.

CHAPTER IV

DESIGNS OF FMR ENHANCED ESAS

4.1 An FMR Enhanced Single-turn Small Loop Antenna

A small single loop is one of the simplest yet most efficient ESAs, which has been pointed out in [8][11], so that the practical design for an FMR enhanced ESA proposed in this dissertation starts from a stripe-pattern, single-loop ESA. A few adjustments have been made in the geometry of the loop structure based on the nature of the thin-film YIG core and to achieve optimized radiation performance.

The YIG thin film on hand for prototype fabrication as aforementioned is a 3.08um thick layer of YIG coating grown on GGG substrate, which makes the thickness of the whole film 0.5mm. Its length and width are 6mm and 5mm, respectively. Dimensions of the practical thin-film are directly imported into HFSS.

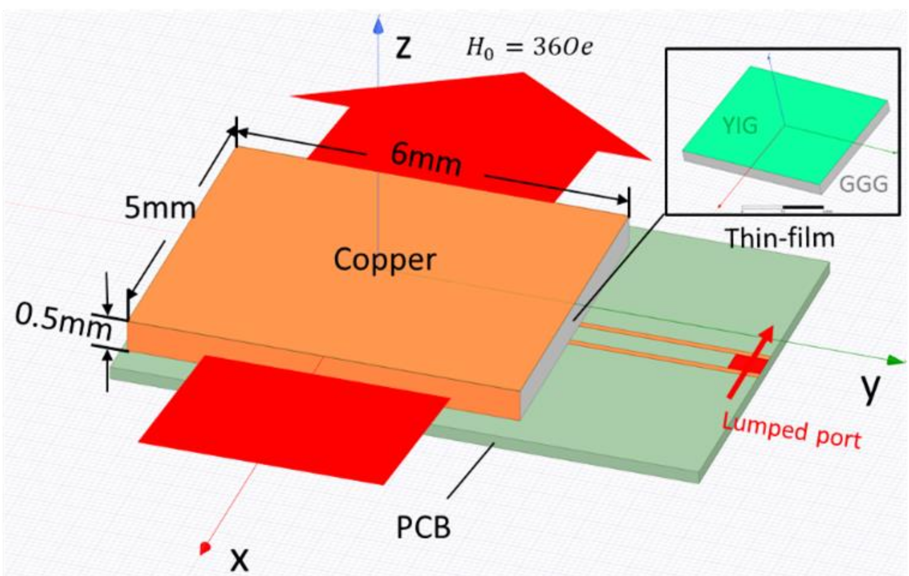

Figure 25. The trimetric view of the FMR enhanced small loop antenna design in HFSS: Top and Excitations.

To tightly accommodate the thin-film YIG core so that the FMR enhanced ESA in design can be as conformal as possible, the metallic structure of this ESA is designed to be a 6mm wide copper stripe closely wrapping around the thin-film YIG core along the direction of its width as shown in Fig. 25. The thickness of the copper stripe is set as 3μm (larger than the skin depth at 0.7 GHz).

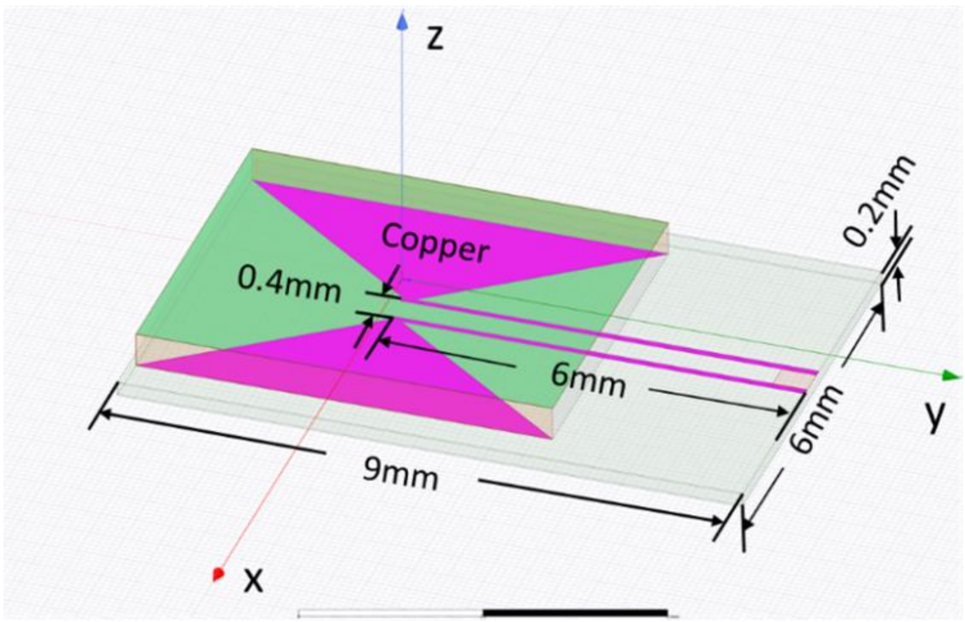

Figure 26. The trimetric view of the FMR enhanced small loop antenna design in HFSS: Bottom on PCB.

On the bottom surface of this ESA, the copper stripe has been taped into an isosceles triangular shape from two longer edges of the surface to the middle. At both ends of the stripe, a pair of 6 mm long copper feeding lines are connected to it, like displayed in Fig. 26. The gap between two feeding lines is 0.4mm. The width of the feeding line is 0.1mm.

In brief, the conducting structure of this FMR enhanced small single loop antenna looks like a small tunnel, built over a bow-tie antenna with two side walls and a rectangular roof, to guide the RF signal. All dimensional parameters of this modified single-loop shell frame are determined through an extensive examination of full-wave simulations with different modifications in geometry for optimizing efficiency enhancement of this ESA and field distribution inside the thin-film core. A box in sizes of $6\text{mm} \times 9\text{mm} \times 0.2\text{mm}$ are created in HFSS under the ESA, assigned with parameters of Rogers RO4003C [39], for including the influence of the print circuit board (PCB) used in Chapter VII on the performance of the ESA into the full-wave simulation. A lump-port excitation is assigned to the other end of the feeding lines with the direction of I_0 along x axis. Like the excitation setup of the ideal radiator, a DC magnetic bias field H_0 of 36 Oersted parallel to I_0 is assigned to the thin-film YIG as indicated in Fig. 25. So this FMR enhanced ESA is also designed to operate around 0.7GHz. What needs to be emphasized here is that this ESA is not only physically small but also extremely electrically small, whose largest physical dimension is just approximately one hundredth of its operating wavelength. Under this circumstance, any improvement in its radiation efficiency and input impedance will be considered as significant elevation. Let alone the change shown in Fig. 27 to 29 is indeed prominent in their absolute values. Controlling the strength of the DC magnetic bias field to change the FMR frequency, which is the operating frequency of this FMR enhanced ESA, makes this ESA tunable. The metallic part of this FMR enhanced ESA and the ferrite thin-film is not glued together, which means this device is reusable for any other thin-film ferrite than YIG, as long as the physical dimension of it fits to the internal volume of the external modified single loop antenna shell.

The S11, Z_{in} and E_{rad} of the modified small single loop antenna with and without the thin-film YIG are exhibited through Fig. 27 to 29.

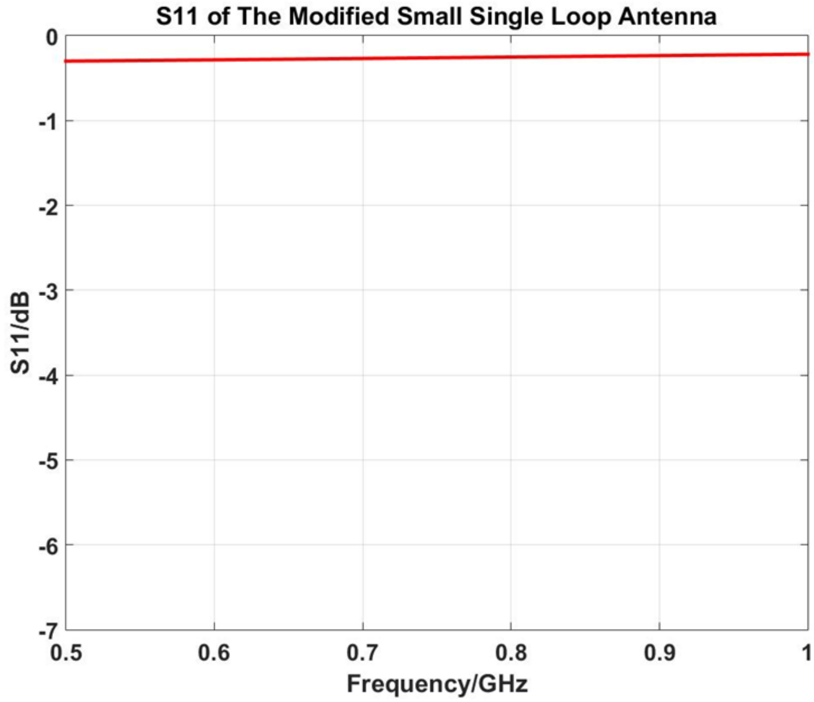

(a)

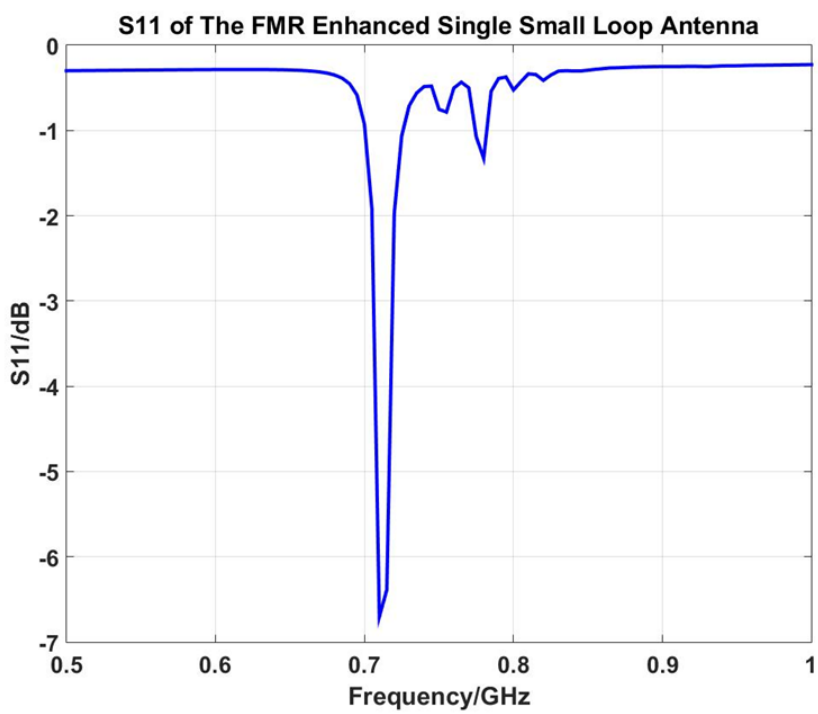

(b)

Figure 27. S11 of the modified single small loop antenna: (a) Air-core; (b) FMR enhanced.

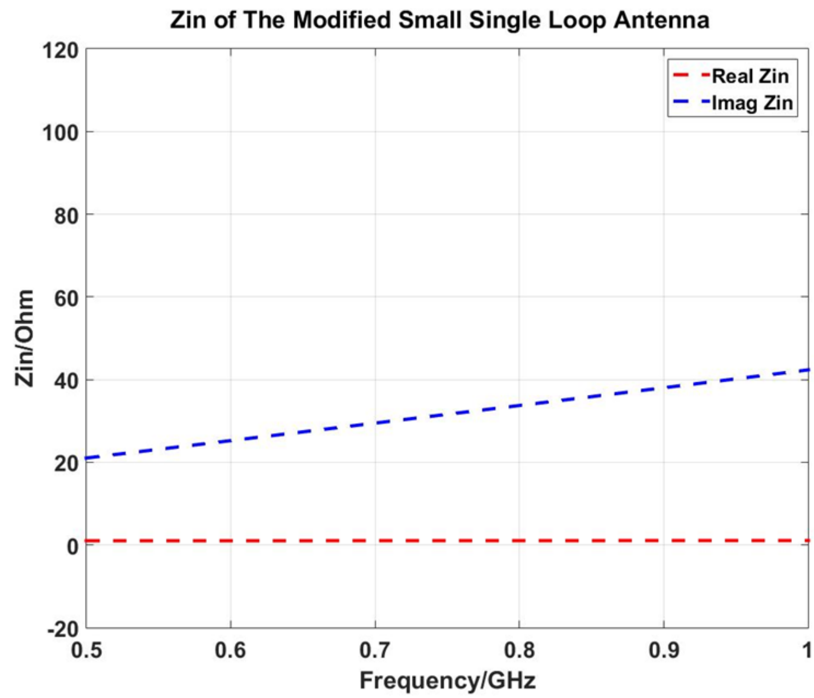

(a)

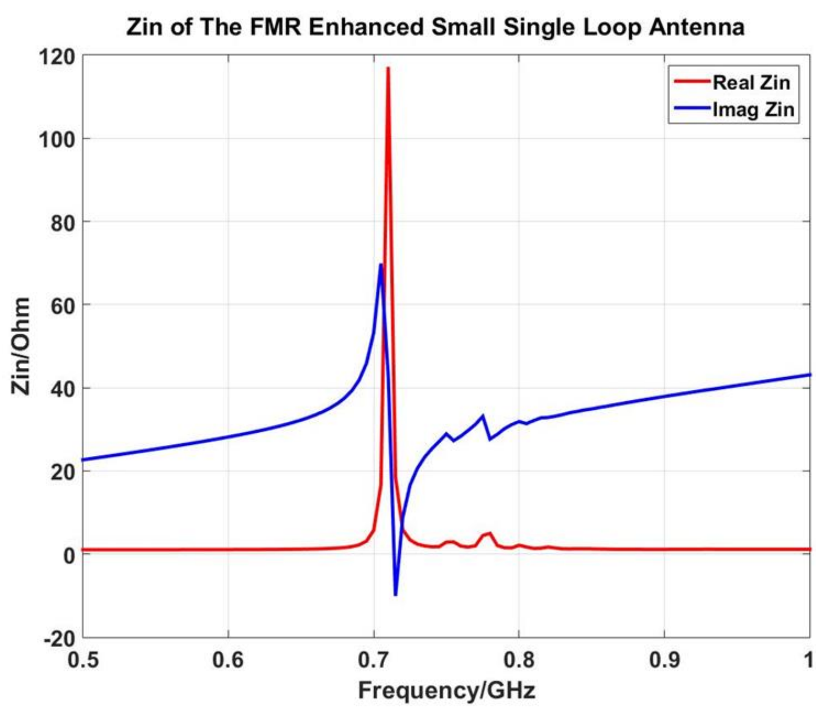

(b)

Figure 28. Z_{in} of the modified single small loop antenna: (a) Air-core; (b) FMR enhanced.

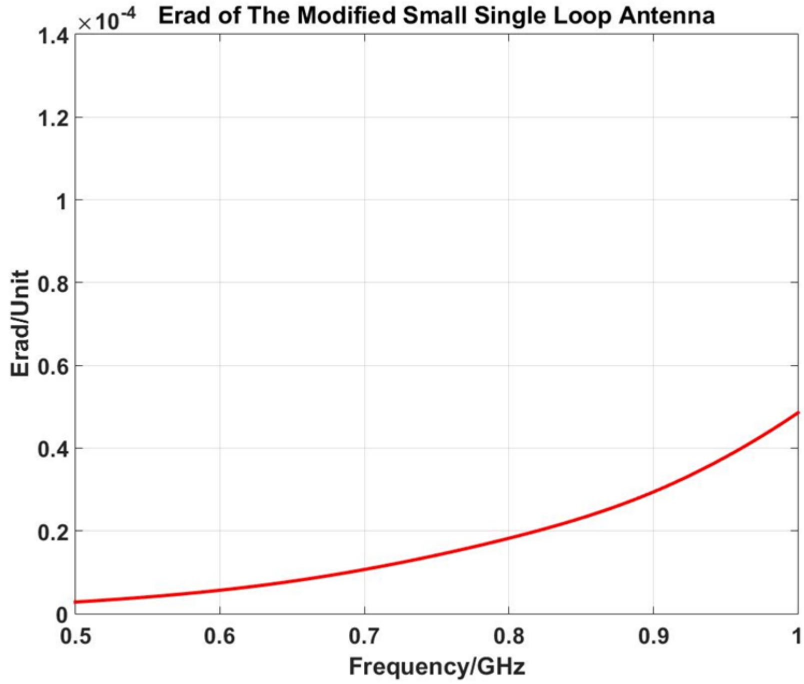

(a)

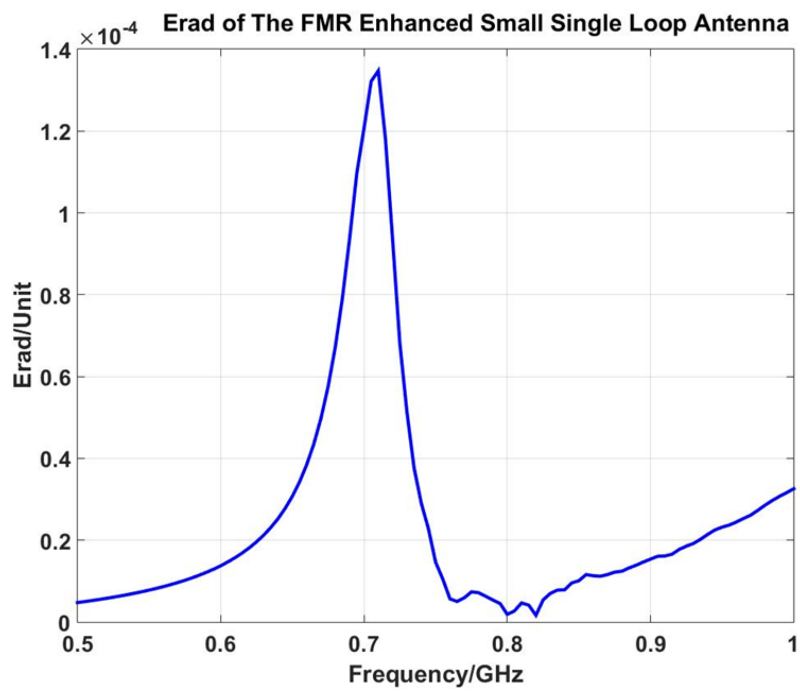

(b)

Figure 29. E_{rad} of the modified single small loop antenna: (a) Air-core; (b) FMR enhanced.

Compare Fig. 27 (a) and 27 (b), it can be seen that without FMR enhancement, its S11 is quite flat and close to zero, which means that most of the input power is being reflected. With FMR enhancement, a dip of nearly –7 dB can be seen at the expected FMR frequency, which means the ESA now is absorbing more power due to the FMR.

The change in S11 after the involvement of the thin-film YIG shows how much the input impedance matching has been improved by FMR.

Compare Fig. 28 (a) and (b), it can be seen that without FMR enhancement, there is no resonance in Z_{in} across the frequency band of interest. The resistance of this modified single loop antenna is only about 1.04 Ohm. However, a resonance due to FMR does appear around 0.7GHz. The real component of the input impedance Z_{in} increases to 118 Ohm at FMR frequency. The magnitude of the resonance in ESA's imagine Z_{in} is 80 centered on about 30. The simulation results of input impedance in Fig.28 not only shows the improvement in impedance matching but also the potential of matching loaded ESAs' input impedance directly to the convenient 50 Ω or 75 Ω with the proper thin-film ferrites.

In Fig. 29, there is a peak in the radiation efficiency E_{rad} due to FMR as well. The radiation efficiency has been improved from 0.0013% to 0.013% at FMR frequency, which is approximately 10 times larger than the original value of the radiation efficiency before inserting the thin-film YIG core. Since the magnitude of FMR can be adjusted through the linewidth of the thin-film YIG by changing its lattice structure, the improvement of E_{rad} still has room to grow in the future.

For additional information, some other antenna parameters like the realized gain and total efficiency are also given here with and without the FMR enhancement as shown in Fig. 31 and Fig. 32. From the simulation report of the radiation pattern, it is obvious that with FMR's impact, the gain is also been elevated from -59.7 dB to -36.8 dB with a 30 dBm input power driving the antenna. From Fig. 32, the total efficiency E_{total} is slightly lower than the E_{rad} as expected. According to $E_{total} = (1 - |S_{11}|^2)E_{rad}$, the better impedance matching, the higher E_{total}.

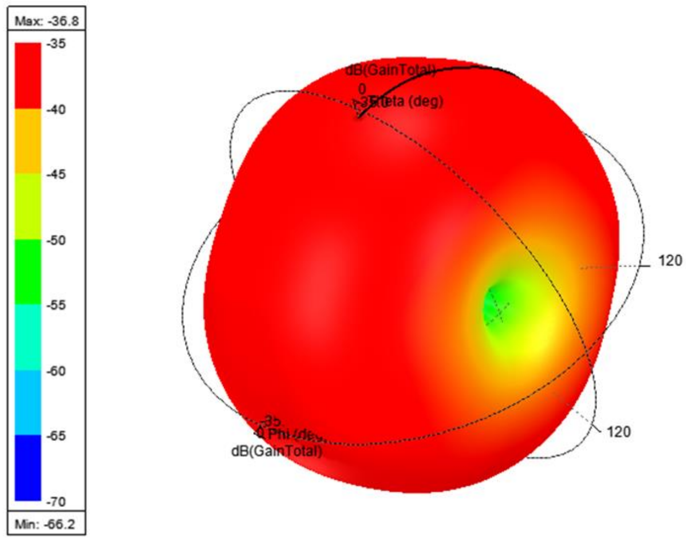

Radiation Pattern (Realized Gain) of **YIG-Core**

(a)

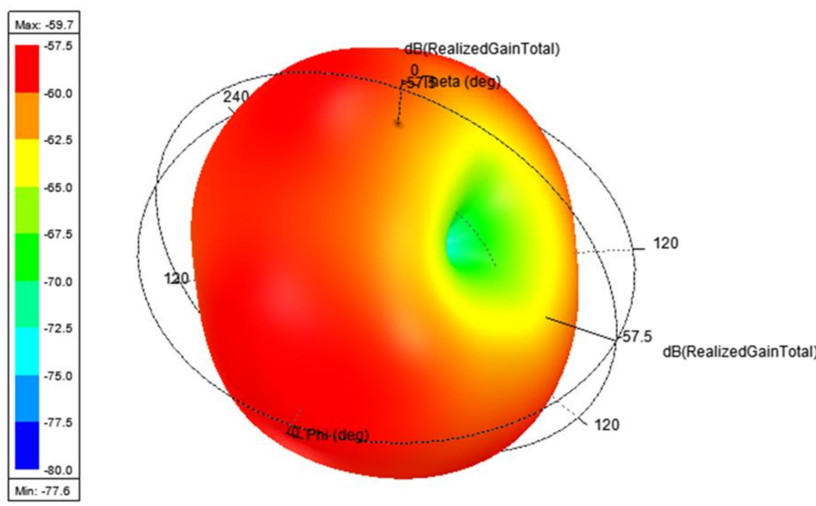

Radiation Pattern (Realized Gain) of **Air-Core**

(b)

Figure 30. The realized gain of the FMR enhanced small single loop antenna: a) with FMR; b) no FMR.

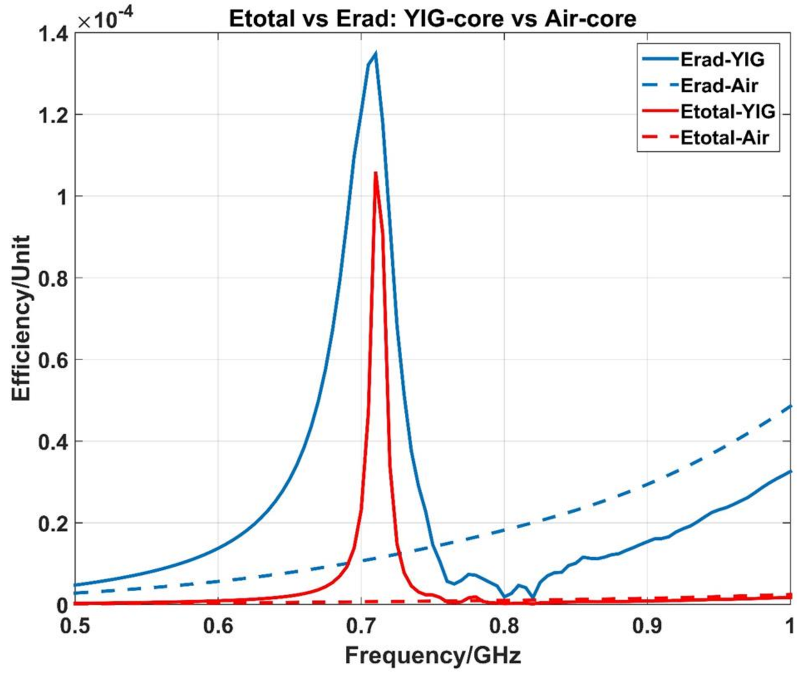

Figure 31. The comparison of E_{total} and E_{rad} with and without FMR.

4.2 FMR Enhanced Multi-turn Small Loop Antennas

An ideal, two-turn, strip pattern loop antenna model with and without thin film ferrite loaded is also built and simulated using HFSS, which are shown in Fig. 32. The model is built based on the exact same YIG sample used to design the single loop antenna described in the previous section, so the parameter of the YIG thin film will be transferred directly. The width of copper stripes consist of each turn of the loop structure is 2.2mm. The thickness of the copper strip stays as 3um. A lumped port excitation is assigned to the green part in Fig. 32 (b) with the integration direction pointing along the x axis. For comparison purpose, a DC magnetic bias of the same strength (36 Oe) is applied to the ESA, also along x axis. Like the investigation done to the single loop antenna, three parameters S11, Z_{in} and E_{rad} for each cases are reported here from Fig. 33 to 35. Different from the previous investigation, the observing frequency band has been enlarged from 0.5 GHz to 10 GHz. And the case where only GGG substrate been loaded to the ESA is added to embed the impact solely by GGG.

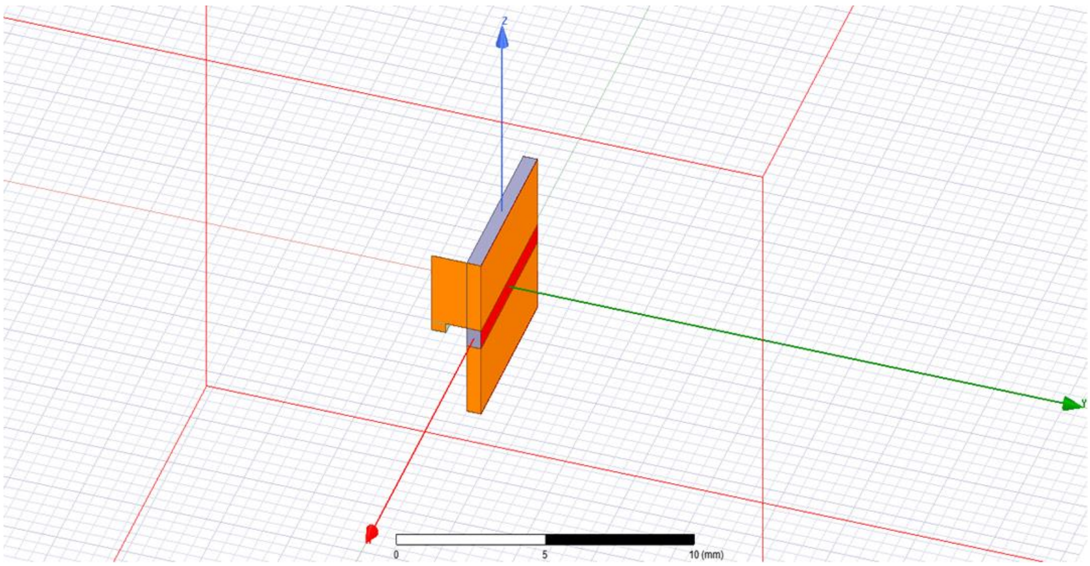

(a)

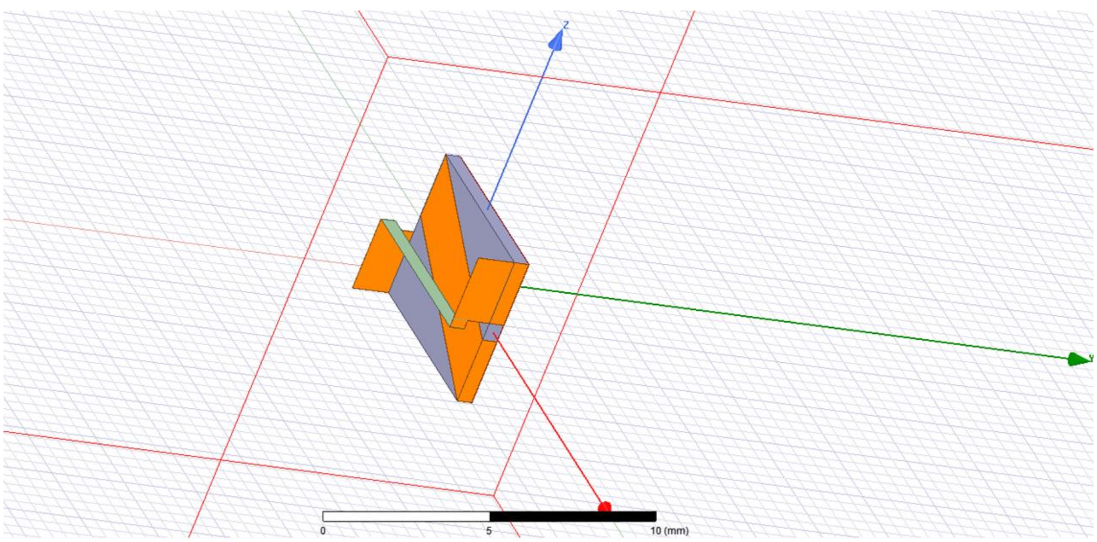

(b)

Figure 32. The FMR enhanced two-turn, small loop antenna in HFSS: a) front view; b) back view.

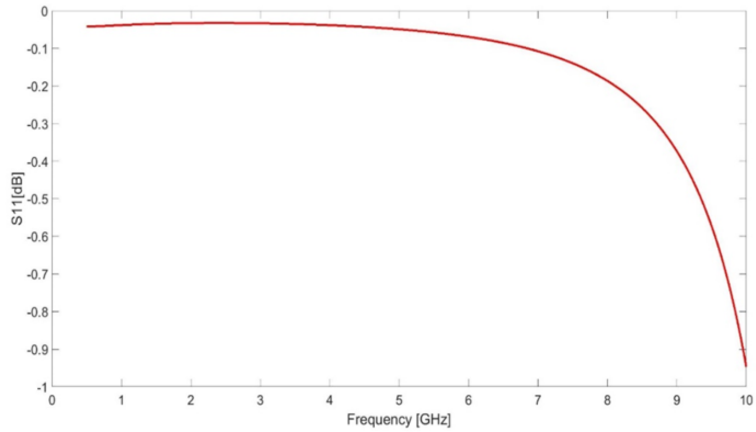

(a)

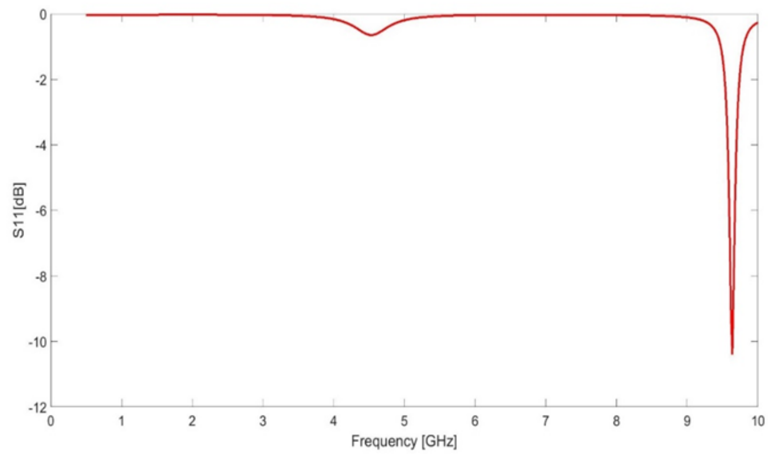

(b)

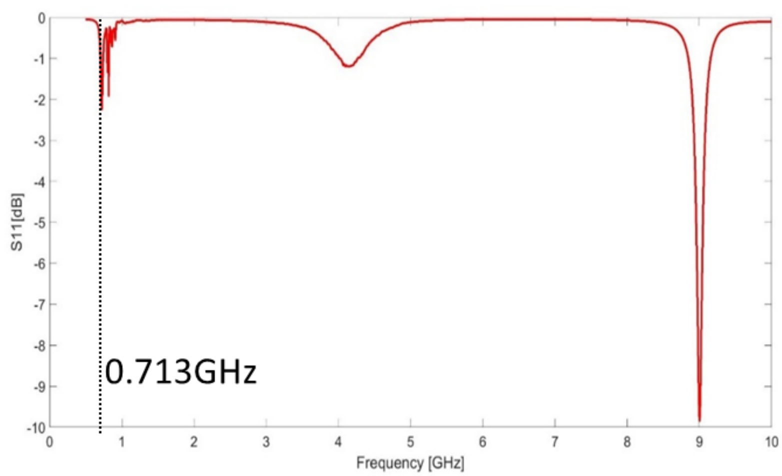

(c)

Figure 33. S11 of the two-turn, small loop antenna: a) Air-core; b) GGG only and c) with FMR.

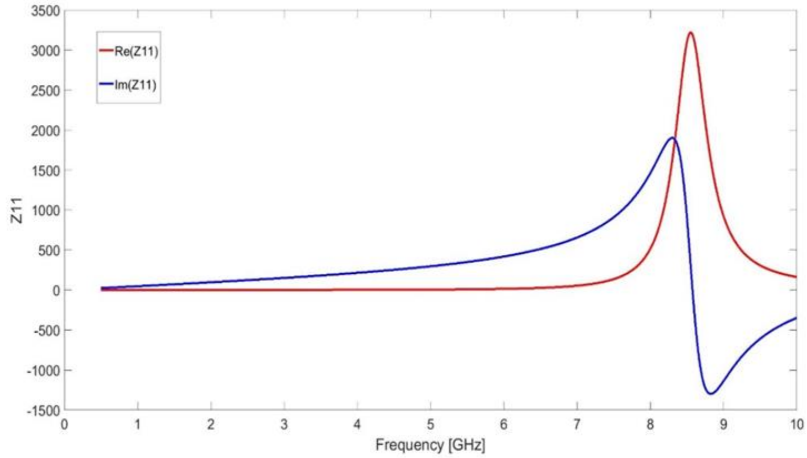

(a)

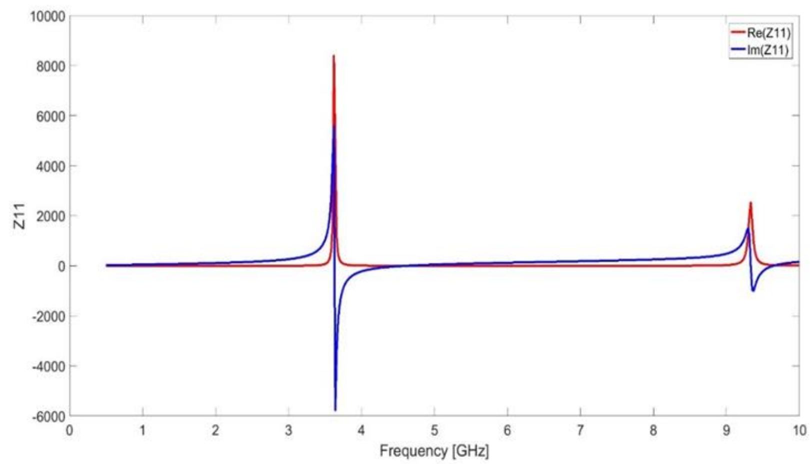

(b)

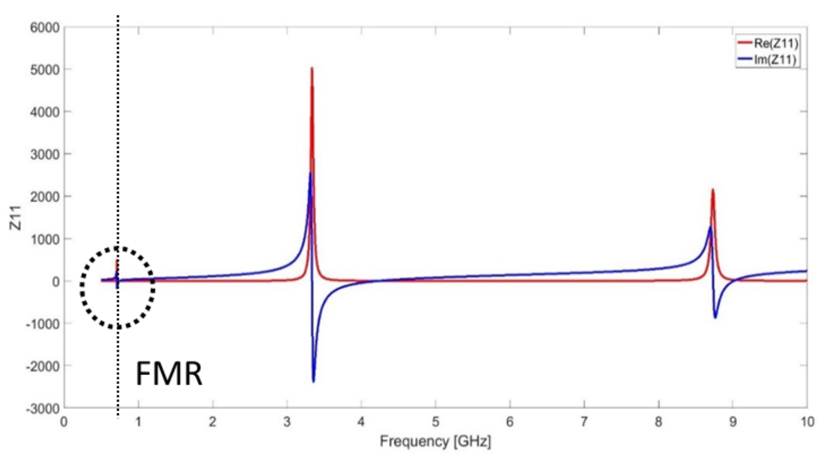

(c)

Figure 34. Z_{in} of the two-turn, small loop antenna: a) Air-core; b) GGG only and c) with FMR.

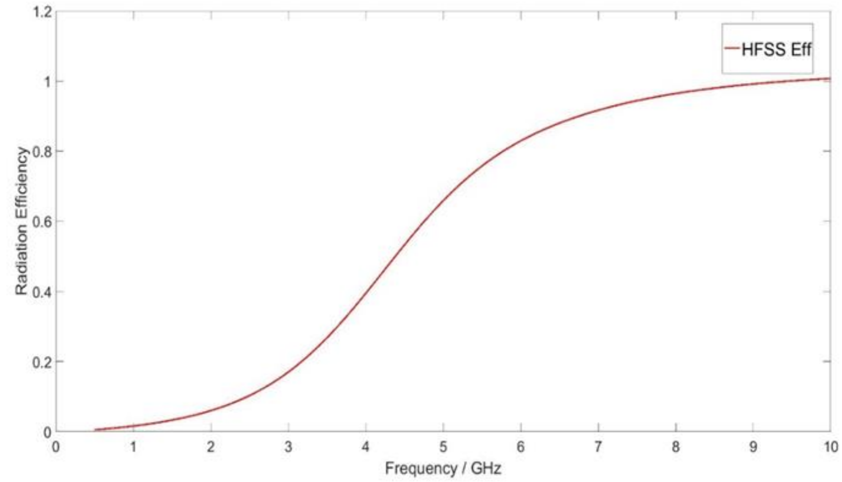

(a)

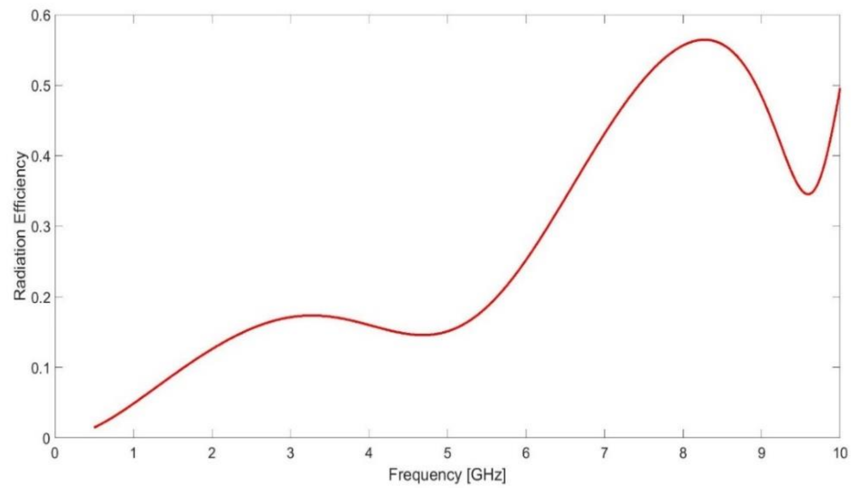

(b)

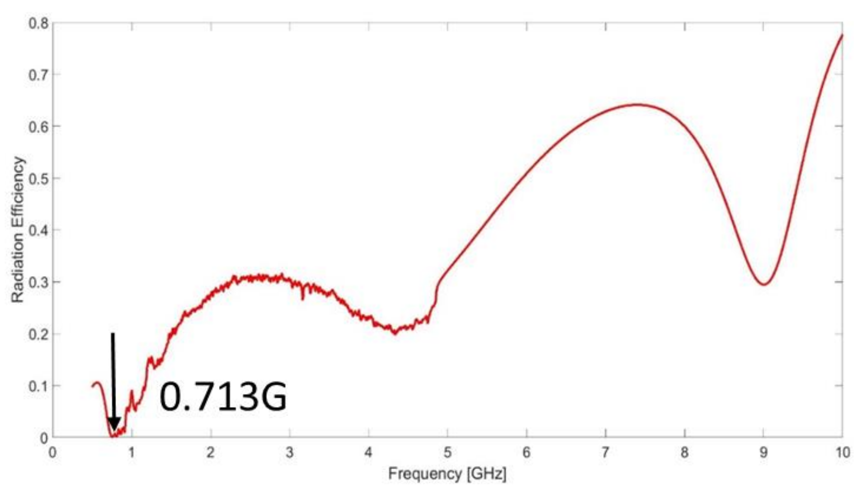

(c)

Figure 35. E_{rad} of the two-turn, small loop antenna: a) Air-core; b) GGG only and c) with FMR.

Judging from the simulation results of all three parameters shown above, the conclusion can be easily drawn that for the two-turn loop antenna, FMR can only improve the impedance matching ability but no help to the radiation efficiency perspective. The Four-turn design as shown in Fig. 36 has also be examined in this dissertation. Unfortunately, the phenomenon observed in Z_{in} and E_{rad} is the same as that in two-turn case. There is no need to exhibit all simulation results of the four-turn design for simplicity.

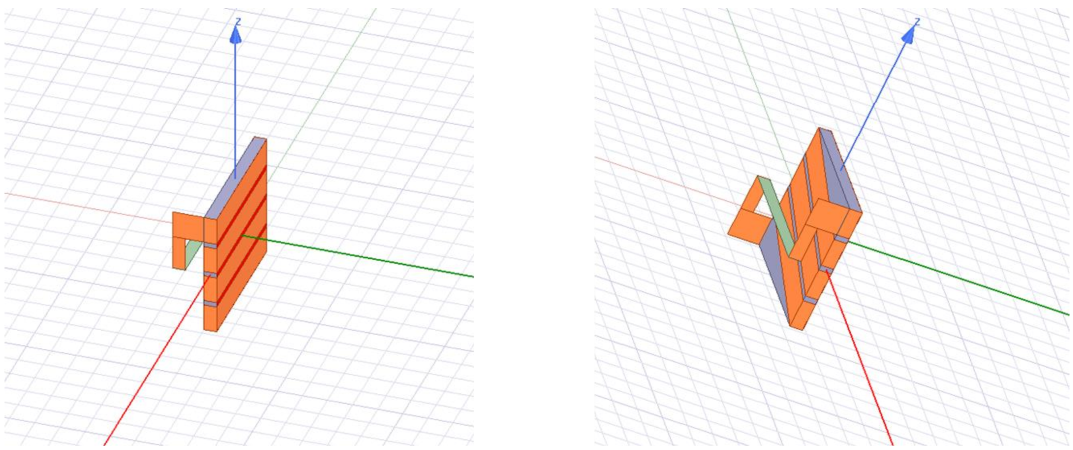

（a） （b）

Figure 36. The design of the four-turn, small loop antenna: a) front view; b) back view.

It appears that increasing turns of the loop structure does not optimize the enhancement from FMR to the radiation efficiency of ferrite ESAs, which contradicts to the conventional theory about the way to increase ferrite rod antennas$'$ E_{rad}. A detailed explanation about why this happened and how to optimize the conducting structure of FMR enhanced ESAs will be given in Chapter V from the view of equivalent circuit model and quality factor Q.

CHAPTER V

CIRCUIT MODELS FOR FMR ENHANCED ESAS

5.1 Existing Circuit Models for Small Antennas

The equivalent circuit model is the most common and effective method to simplify and aid the analysis and design of ESAs. Engineers who investigate ESAs independently almost all have their own circuit models for either definition explanation or parameter calculation, i.e. bandwidth, input impedance and efficiency. Some of the popular circuit models are exhibited in Fig. 37. However, these circuit models all have shortcomings.

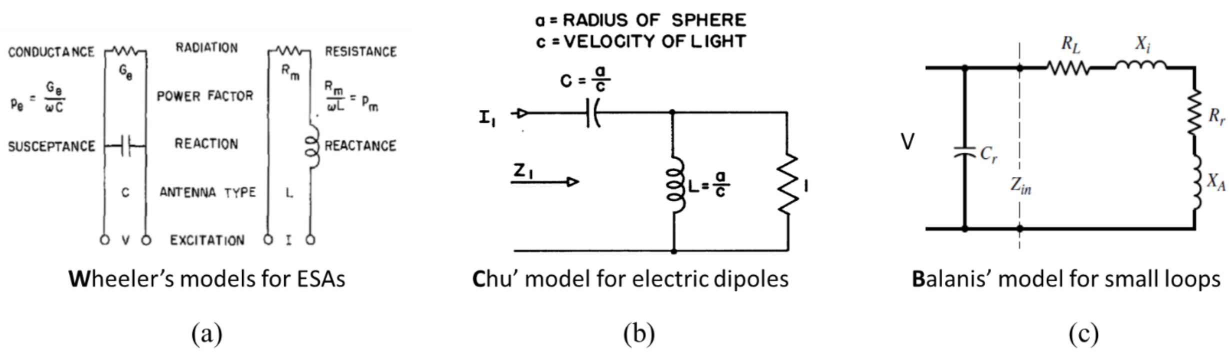

Figure 37. Three famous circuit models of ESAs: a) Wheeler's; b) Chu's and c) Balanis'.

Wheeler's model in [6] only represents the non-self-resonant ESAs. Chu's circuit model in [8] only deals with fields outside the ESA. Power dissipation as heat on ESAs are not considered in Chu's model, which is essential when it comes to efficiency modeling for ESAs. Balanis' circuit model [7] for small loops is so far the most customized and functional model to calculate radiation efficiency and input impedance, but the value of the radiation resistance in it changes with frequency, which means this model does not contain transient response information of ESAs that it mimics.

After going through a few major popular circuit models above for ESAs nowadays, a conclusion has been drawn that there is no comprehensive, frequency-independent equivalent circuit model that can predict both the input impedance and the radiation efficiency of ESAs simultaneously. Such circuit model is the foundation to build one that can further predict the same two parameters for FMR enhanced ESAs. Since the loop antenna structure is what has been implemented in the actual design, the path to obtain the final circuit model for FMR enhanced ESAs starts from developing a novel lump-element circuit model for small loops.

5.2 A Novel Circuit Model for Small Loop Antennas

Despite its drawbacks, one of Chu's model's merits is that it is frequency-independent. Therefore, the first step to structure a complete, lump-element equivalent circuit model for a small loop is to apply duality theorem to Chu's model of small electric dipoles. Then a circuit model for lossless small loops is obtained inheriting with the merit of frequency-independency. Adding a resistance R_{ohm} series-connected to the lossless circuit model represents the power loss on the conducting loop structure. Since the input impedance of the antenna is defined to the lump port connection point and the length of the feeding line in the practical design proposed in this paper is comparable to the loop structure itself in size, another inductance L_f is added in front of R_{ohm} to compensate the effect of the feeding lines.

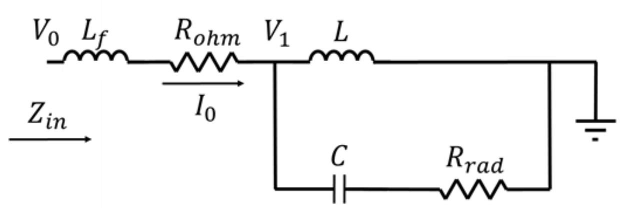

Figure 38. The circuit model for small loops.

So far the new practical, frequency-independent circuit model for small loop antennas is formed as shown in Fig. 38. The value for each element in this circuit model is obtained through curve-fitting the resulting real and imaginary part of the input impedance and radiation efficiency traces from the circuit model against those simulated by HFSS simultaneously over a frequency spectrum from 0.5GHz to 1 GHz with Differential Evolution (DE) algorithm. In Fig. 39, the maximum deviation in real Z_{in} is 0.015 Ω. In Fig.40, imaginary Z_{in} calculated through HFSS and the circuit model are identical. The error in radiation efficiency calculation between circuit model and full-wave simulation is in the order of 10^{-6}as revealed in Fig. 41. Matches through Fig. 39 to 41 fully validate the accuracy and authenticity of the new equivalent circuit model. The value for each element in the circuit model is listed in TABLE II. If there are multi-turns N in loop structure, the value of R_{ohm} will increase by a factor of N and L and C will fluctuate by the scale of N^2.

TABLE II
CIRCUIT MODEL PARAMETERS

Symbol	Quantity	Value/Unit
L_f	inductance of parallel feeding structure	5.9761 Ω
L	inductance of modified single loop structure	0.8904 nH
C	capacitance of modified single loop structure	0.1394 nF
R_{ohm}	ohmic resistance	1.0862 Ω
R_{rad}	radiation resistance	2.05 Ω
R_m	effective resistance of the thin-film YIG	122.39 Ω
L_m	effective inductance of the thin-film YIG	0.1484 nH
C_m	effective capacitance of the thin-film YIG moment	0.3381 nF

Table 2. Parameters of the circuit model for FMR enhanced ESAs.

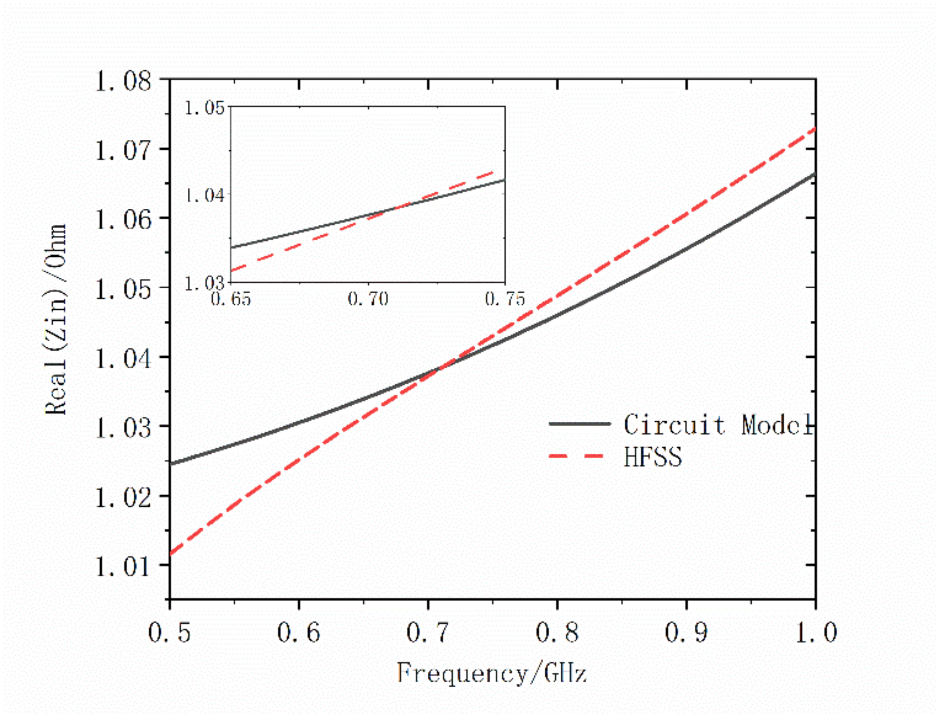

Figure 39. Real Z_{in} without YIG thin-film core: HFSS vs Circuit Model.

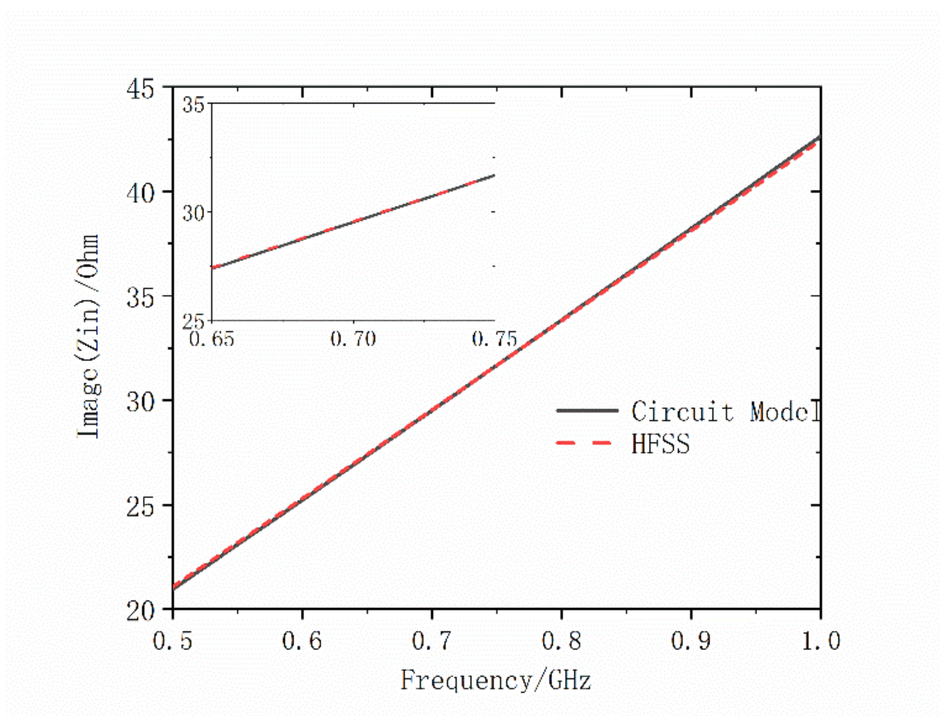

Figure 40. Imaginary Z_{in} without YIG thin-film core: HFSS vs Circuit Model.

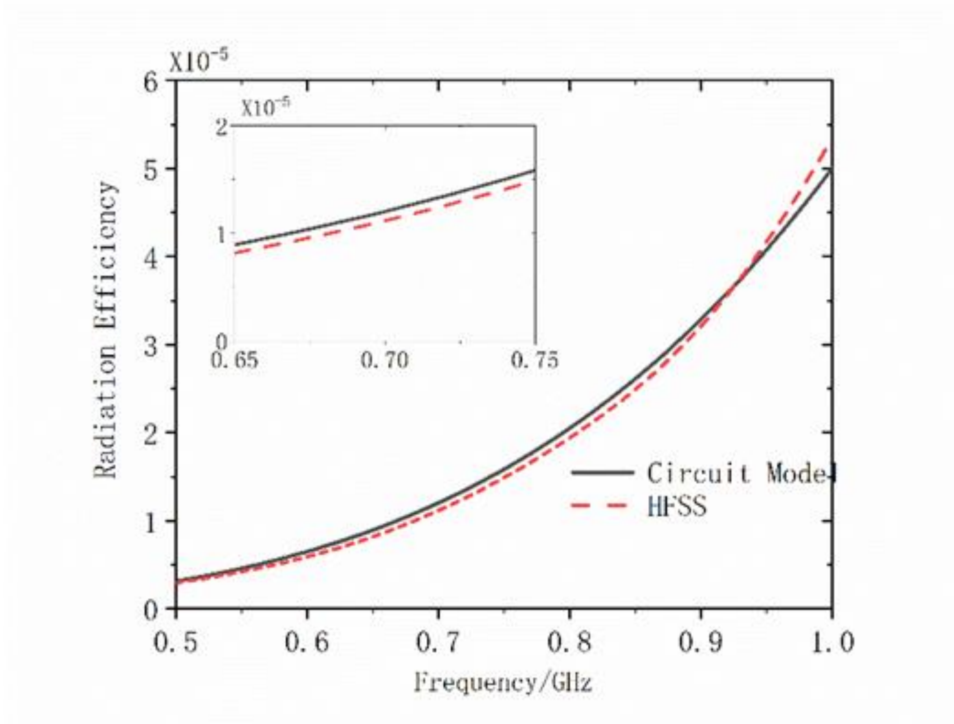

Figure 41. Radiation efficiency E_{rad} without YIG thin-film core: HFSS vs Circuit Model.

The legitimacy of this new model, especially the way that each lump element connected, can be also verified through examining the terms in the expression of the E field component of an ideal magnetic dipole:

$$E_{\phi} = E_{near} + E_{far} = \frac{I_m l sin\Theta e^{-jkr}}{4\pi r^2} + \frac{-jkI_m l sin\Theta e^{-jkr}}{4\pi r^2} \tag{5.1}$$

Clearly, the expression can be separated into one near-field term and one far-field term. The two terms are associated with stored near-field electrical energy W_e and radiating far-field power P_{rad} respectively. In the circuit model, W_e corresponds to a capacitor C and P_{rad} leads to the radiation resistance R_{rad}. The term $I_m l$ in both E_{near} and E_{far} stands for magnetic moment of a magnetic dipole in the field analysis and the voltage V_1 across L (loop structure) in the circuit model, which explains both C and R_{rad} should be parallel connect to L. Since there has already been a 90° phase off between impedances of a capacitor and a resistor and in order to keep the same 90° phase difference between voltages across C and R_{rad}, the current goes into C and R_{rad} must have the same frequency-dependency and R_{rad} is a constant, which imply the series connection between C and R_{rad} and the frequency independency of R_{rad}.

It is also a fact that if the conductor used to form the loop structure has smaller conductivity (larger R_{ohm}) than Copper which is applied here, the voltage V_1 across the loop will drop. Series connecting L and R_{ohm} in one branch of the circuit model, like in the Balanis' model, does not reflect the physics above, But, placing the R_{ohm} on the main stem does. So the connection of R_{ohm} in Fig. 38 is sound.

5.3 The Comprehensive Circuit Model for FMR Enhanced ESAs

Based on the solid circuit model for lossy small loops, the circuit model for FMR enhanced ESAs can be achieved by introducing the RLC tank validated in Section II series connected on the branch of L. Since the FMR generated from the biased thin-film YIG will mainly enhance the magnetic flux flowing through the loop structure (increase V_1) and affect the inductance in the input impedance of the ESA, the connection and location of the spin-motion model in the complete model for FMR enhanced ESAs are set as shown in Fig. 42.

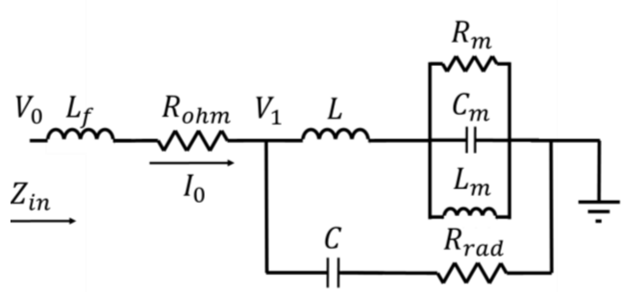

Figure 42. The circuit model for FMR enhanced ESAs.

Remaining the values for all elements in the previous circuit model for lossy small loops unchanged and setting the initial value of R_m, L_m and C_m through formulas (3.21), (3.22) and (3.23), matches through Fig. 43 to 45 in input impedance and radiation efficiency with thin-film YIG loaded between circuit modeling and full-wave simulations can be obtained simultaneously by only optimizing initial values of elements in the RLC tank with DE algorithm during curve-fitting. The optimized value for each component in the RLC tank is listed in the TABLE II.

The discrepancy between the final and starting values of R_m, L_m and C_m is small and caused by the unstandardized loop structure of the practical design and the actual distribution of H field inside it, which might not be strictly uniform.

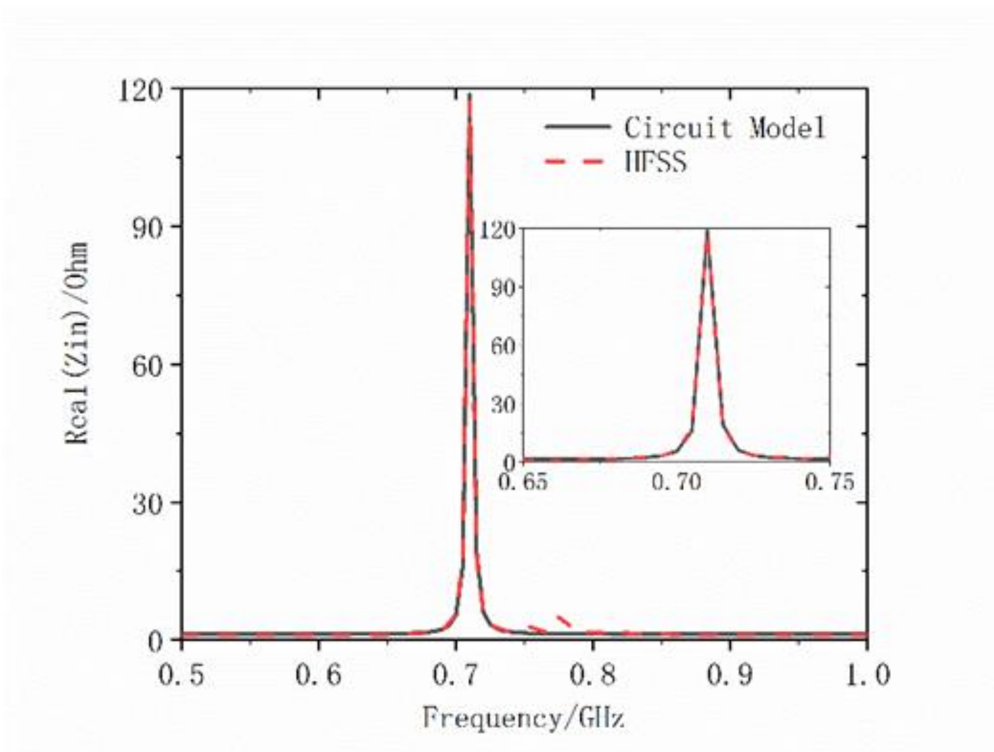

Figure 43. Real Z_{in} with FMR enhancement: HFSS vs Circuit Model.

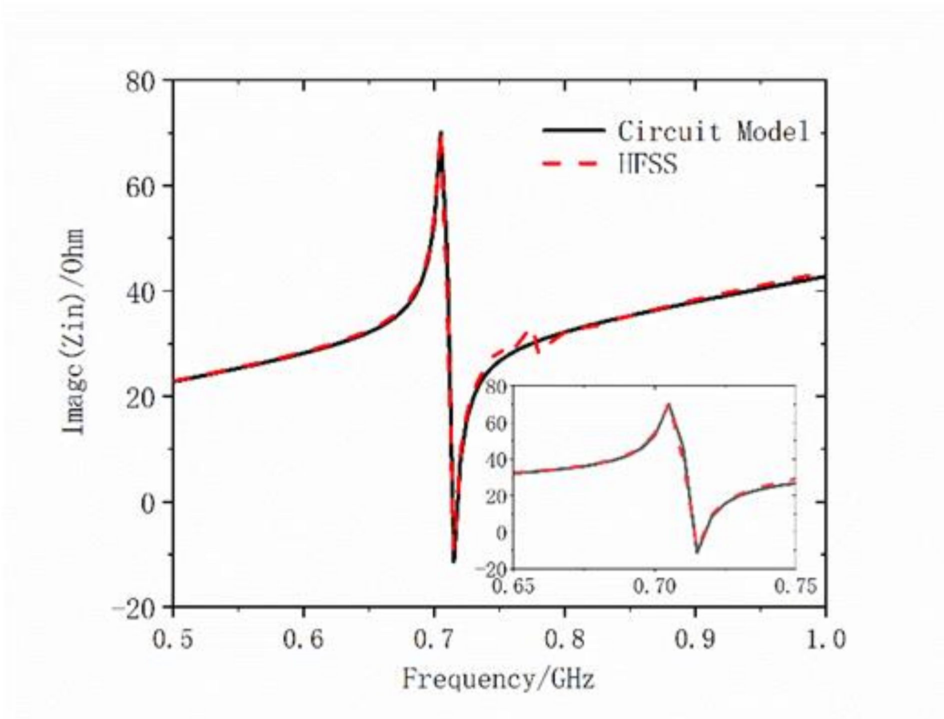

Figure 44. Imaginary Z_{in} with FMR enhancement: HFSS vs Circuit Model.

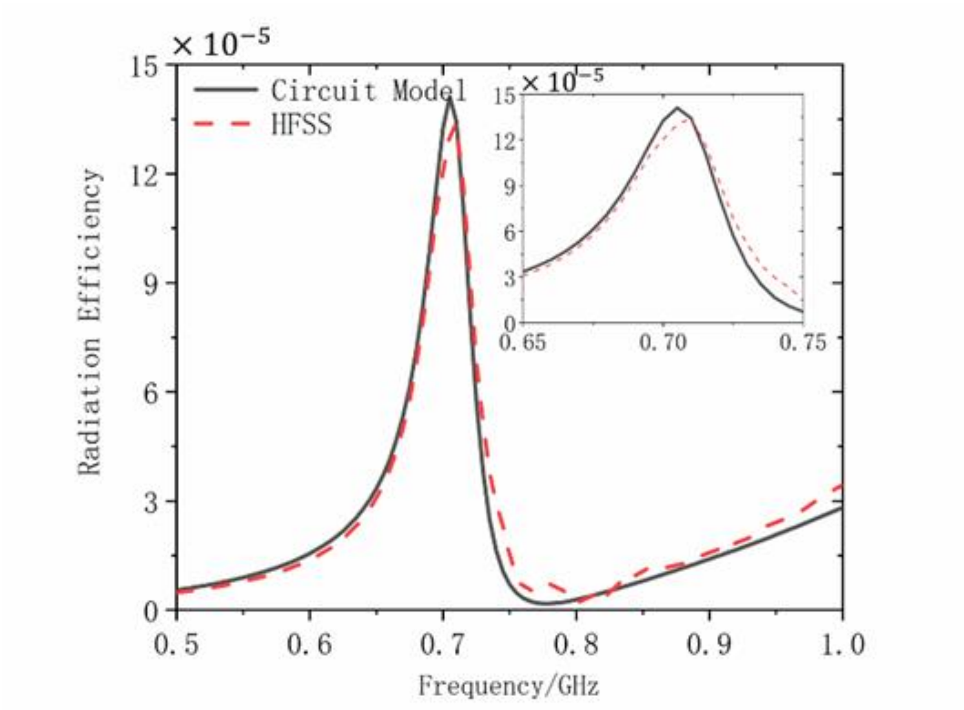

Figure 45. Radiation efficiency E_{rad} with FMR enhancement: HFSS vs Circuit Model.

The consistency in the circuit model calculations and HFSS simulations for both parameters (Z_{in} and E_{rad}) again validates the correction of the circuit model for FMR enhanced ESAs.

Further massaging the value of each element in the circuit model above, another two conclusions has been drawn as below:

First, increasing turns of the loop structure actually mitigate the radiation enhancement by FMR. Detailed analysis is demonstrated in appendix.

Second, the magnitude of the peak both in the real part of Z_{in} and E_{rad} due to FMR is mainly decided by R_m. Like R_{ohm} is with respect to σ_e, R_m is related to σ_m. The higher R_m, the larger peak value in both real Z_{in} and E_{rad}, which once again verifies the theory that high μ'' can result in high radiation efficiency for the design of ESAs.

5.4 Optimize the Design from the View of Circuit Models

As stated before in Chapter II, even though the resonance in the input impedance and the improvement in the radiation efficiency of FMR enhanced ESAs are mainly determined by the quality of the thin-film ferrite itself, proper feeding the ferrite core with EM fields induced by the RF signal for a better interaction between them in order to get desired antenna parameters are also very crucial, which can be accomplished through optimizing the metallic structure of the ESA. And to clear the ambiguity in whether the strip-pattern single loop structure discussed in this dissertation is the optimized design or at least close to the beset one for FMR enhanced ESAs and also to show what kind of the guidance that the newly developed circuit models can provide for designing such FMR enhanced ESAs as well, the condition that should meet for the quality factor of the conducting loop structure Q_{loop} and the thin-film ferrite $Q_{ferrite}$ in order to realize radiation efficiency enhancement is derived as following. Since to accomplish the input impedance matching improvement seems never to be a problem in any of the case with different number of turns which tested by HFSS before, the focus here will naturally be how to acquire radiation efficiency elevation through adjusting the conducting structure.

If the small loop antenna is assumed to be driven by a stationary voltage source V_0, the voltage associated with the $I_m l$ in E_Φ of a small loop is marked as V_1 across C and R_{rad} in Fig. 38 and V_1' in Fig. 42, separately. At any FMR frequency, $j\omega_r L_m = -1/j\omega_r C_m$, so the circuit model in Fig. 42 can be simplified by eliminating L_m and C_m in the spin-motion model for thin-film ferrites, as shown in Fig. 46.

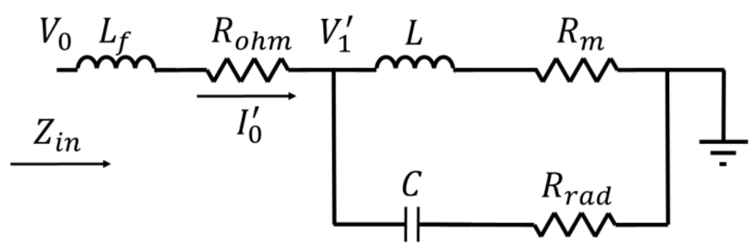

Figure 46. Simplified circuit model for the FMR enhanced single small loop at resonance.

Then the radiation efficiency of ESAs, at supposed FMR frequency, with and without thin-film ferrite loaded are given:

$$E_{Air\_core} = \frac{1}{1 + \frac{|V_0 - V_1|^2}{|V_1 \cdot R_{rad}/(R_{rad} + 1/j\omega C)|^2} \cdot \frac{R_{rad}}{R_{ohm}}} \quad (5.2)$$

$$E_{ferrite_{core}} = \frac{1}{1 + \frac{|V_0 - V_1'|^2}{|V_1' \cdot R_{rad}/(R_{rad} + 1/j\omega C)|^2} \cdot \frac{R_{rad}}{R_{ohm}} + \frac{|V_1' \cdot R_m/(R_m + j\omega L)|^2}{|V_1' \cdot R_{rad}/(R_{rad} + 1/j\omega C)|^2} \cdot \frac{R_{rad}}{R_m}} \quad (5.3)$$

In order to achieve the appropriate feeding for YIG thin-film so that the radiation efficiency enhancement due to FMR can happen, (5.3) ≥ (5.2) must be satisfied. Simplify this relationship, we have:

$$\frac{|V_0 - V_1'|^2}{\left|V_1' \cdot R_{rad}/(R_{rad} + \frac{1}{j\omega C})\right|^2} \cdot \frac{R_{rad}}{R_{ohm}} + \frac{\left|V_1' \cdot \frac{R_m}{R_m + j\omega L}\right|^2}{\left|V_1' \cdot R_{rad}/(R_{rad} + \frac{1}{j\omega C})\right|^2} \cdot \frac{R_{rad}}{R_m}$$

$$\leq \frac{|V_0 - V_1|^2}{\left|V_1 \cdot R_{rad}/(R_{rad} + \frac{1}{j\omega C})\right|^2} \cdot \frac{R_{rad}}{R_{ohm}} \tag{5.4}$$

$$\frac{|V_0 - V_1|^2}{|V_1|^2} \geq \frac{|V_0 - V_1'|^2}{|V_1'|^2} + \frac{R_m R_{ohm}}{R_m^2 + (\omega L)^2} \tag{5.5}$$

Normally, for small loops, C and R_{rad} are significantly smaller than R_m, which indicates the difference between $V_1$and V_1' are mainly caused by R_m. Therefore,

$$V_0 - V_1 \approx \frac{R_{ohm}}{R_{ohm} + j\omega L} \cdot V_0 \tag{5.6}$$

$$V_1 \approx \frac{j\omega L}{R_{ohm} + j\omega L} \cdot V_0 \tag{5.7}$$

Similarly, we have:

$$V_0 - V_1' \approx \frac{R_{ohm}}{R_{ohm} + j\omega L + R_m} \cdot V_0 \tag{5.8}$$

$$V_1' \approx \frac{j\omega L + R_m}{R_{ohm} + j\omega L + R_m} \cdot V_0 \tag{5.9}$$

So,

$$\frac{|V_0 - V_1|^2}{|V_1|^2} \approx \frac{R_{ohm}^2}{(\omega L)^2} \tag{5.10}$$

$$\frac{|V_0 - V_1'|^2}{|V_1'|^2} \approx \frac{R_{ohm}^2}{(\omega L)^2 + R_m^2} \tag{5.11}$$

Substitute (5.10) and (5.11) into (5.5), (5.5) can be further simplified as:

$$\frac{R_{ohm}^2}{(\omega L)^2} - \frac{R_{ohm}^2}{(\omega L)^2 + R_m^2} \geq \frac{R_m R_{ohm}}{R_m^2 + (\omega L)^2} \tag{5.12}$$

$$(\omega L)^2 \leq R_m R_{ohm} \tag{5.13}$$

Rewrite (5.13) as

$$\frac{\omega L}{R_{ohm}} \leq \frac{R_m}{\omega L_m} \cdot \frac{L_m}{L} \tag{5.14}$$

Borrow the concept of Q for a resonator in the circuit theory, we have Q_{loop} defined as $\omega L/R_{ohm}$, for series connection, and $Q_{ferrite}$ as $R_m/\omega L_m$, for parallel connection. So the condition to obtain improvement in E_{rad} in terms of Q_{loop} and $Q_{ferrite}$ is:

$$Q_{loop} \leq Q_{ferrite} \cdot C \tag{5.15}$$

where $C = L_m/L$ is the coupling coefficient between the inductance generated by loop structure and ferrite.

Three conclusions can be drawn from (5.15):

First, better thin-film ferrite (Higher $Q_{ferrite}$) will induce stronger radiation enhancement;

Second, if the ferrite has been selected, we need to strengthen the coupling between the loop structure and the thin-film ferrite (increase C).

Therefore, two angles can be check for improving the design of FMR enhance ESAs here:

First, have more proportions of the volume inside the loop structure occupied by the thin-film ferrite.

Second, decrease the inductance of the loop. According to $L = \mu_0 N^2 A/l$, where l is the length of the loop. Single-turn loop structure is preferred and stripe-pattern is better than wire for having larger l as shown in Fig. 47.

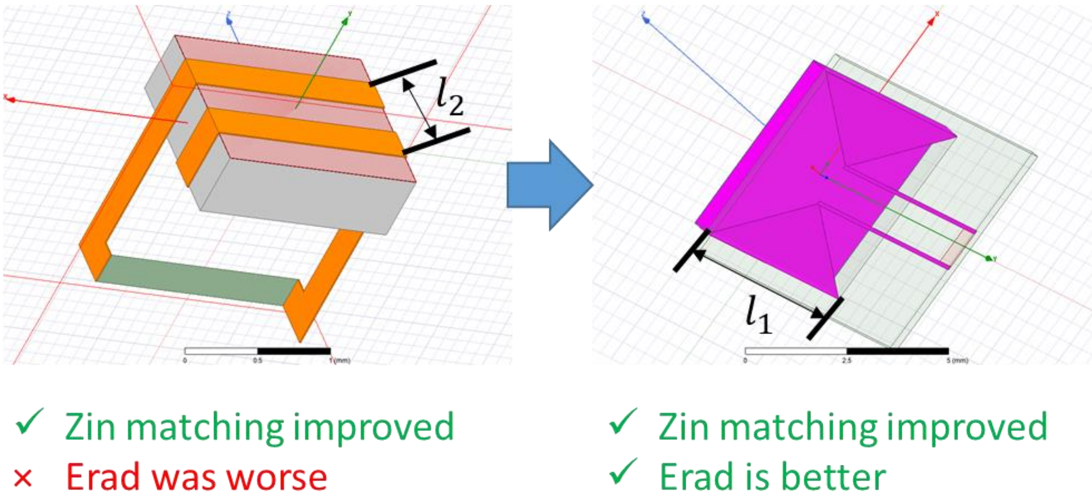

Figure 47. The guidance in designing loop structures.

Based on the conclusions drawn above, the current physical structure of the FMR enhanced ESA here provides decent enhancement in radiation, and clearly there is more room for the design to be improved by getting rid of GGG and filling the loop with pure thin-film YIG or better thin-film ferrite.

CHAPTER 6

EXPERIMENTS AND VALIDATIONS

6.1 Prototype Fabrications

A prototype of FMR enhanced small single loop antenna as designed in Chapter IV Section 3.1 is fabricated. The bottom bow-tie antenna pattern is printed on a 12 mm*20 mm Rogers RO4003C PCB. The top cover is cut from a copper shim with thickness of 0.12 mm. The prototype is ready to be tested after soldering a 50 Ω SMA connector and the top cover to the bottom PCB, as shown in Fig. 48 (b). The thin-film YIG sample as shown in Fig. 48 (a) needs to be inserted into the single loop antenna and placed under the top copper cover during measurements.

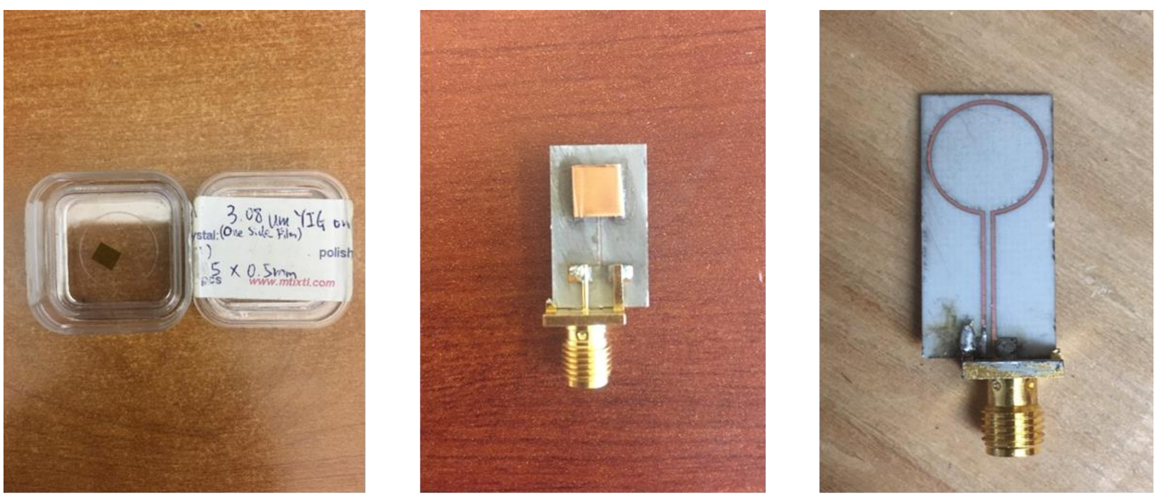

(a) (b) (c)

Figure 48. Prototypes and thin-film samples: a) YIG thin-film sample; b) The modified small single loop; c) The standard small loop.

A standard single loop antenna, serving as a receiver in the near-field measurements, with a radius of 6mm is printed out from a 14 mm*26 mm Rogers RO4003C PCB. The width of the loop copper trace is 1 mm. A pair of 15mm long feeding lines with 1mm separation attach to the single loop structure. The width of the feeding line is the same as that of the copper trace forming the loop. A 50 Ω SMA connector is also soldering to the other end of feeding lines as shown in Fig. 48 (c).

To increase the detection range for the prototype of the FMR enhanced ESA, as shown in Fig. 48 (b), when conducting the near-field measurement, a low noise amplifier (LNA) with gain of 10 dB is integrated with the ESA as shown in Fig. 49 (a). The LNA used here is the LMH5401, high performance, differential amplifier from the Texas Instruments [40], as shown in Fig. 49 (b). So in order to connect it with the network analyzer, a balun needs to be applied between the LNA and the SMA connector, as shown in the PCB layout of the LNA integrated, FMR enhance ESA, in Fig. 49 (c). The LNA is driven by a DC voltage source of 5 V. The two feeding lines of the FMR enhanced ESA are connected to the two input ports of the LNA, respectively.

(a)

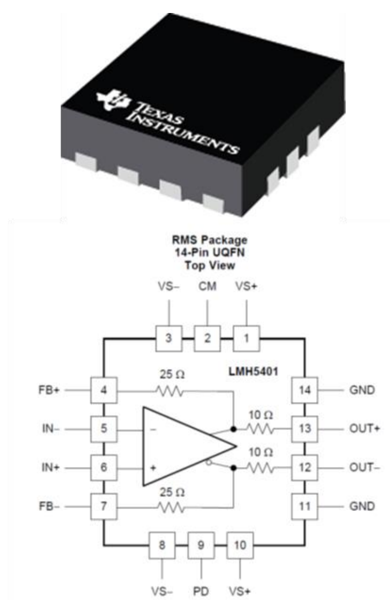

(b)

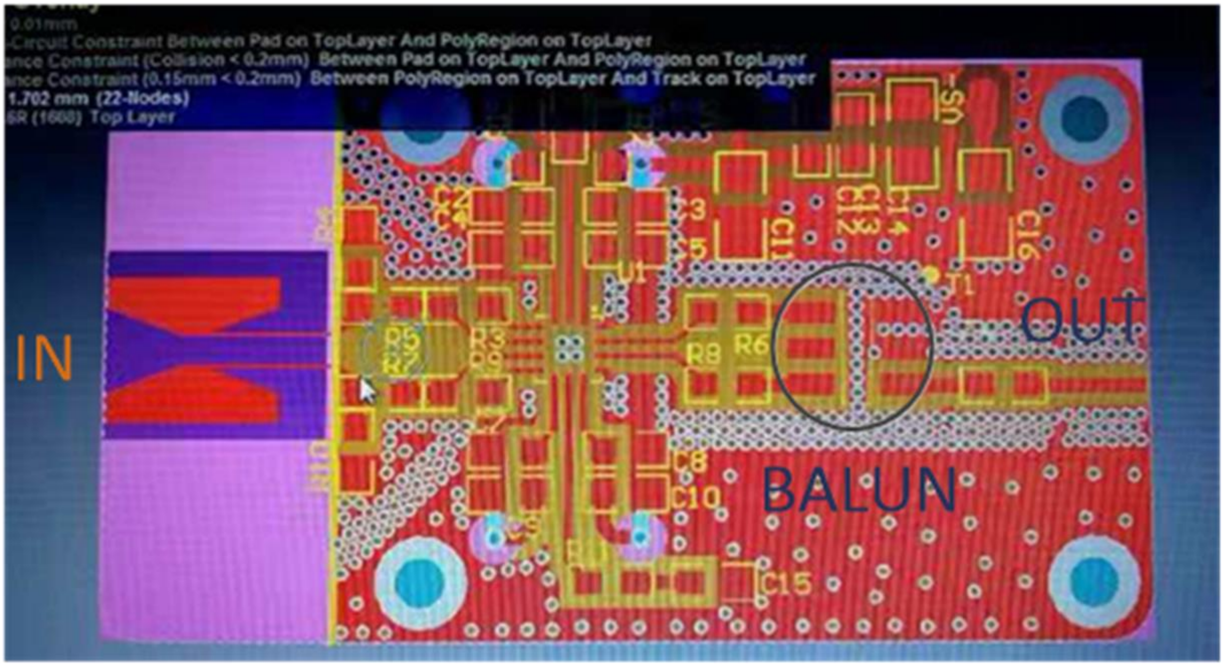

(c)

Figure 49. The prototype with the LNA: a) the fabricated model; b) the configuration of the LNA; c) the circuit layout of the LNA integrated prototype.

6.2 Measurement and Simulation Setups

In order to experimentally verify the improvement in impedance matching and radiation performance for the FMR enhanced small single loop of interest, two particular S parameters of the prototype are measured here. i.e. S11, S21.

The near-field measurement is conducted with the prototype of no LNA first. The prototype is connected to Channel 1 of the network analyzer, while the standard single loop is connected to Channel 2, when it comes to S21 measurements. The prototype is placed between a pair of small electromagnets as shown in Fig. 50. Those electromagnets which can generate up to 1 Tesla DC magnetic field are driven by an adjustable DC current source. A gauss meter is implemented between electromagnets to monitor the magnitude of the DC magnetic field applied to the prototype. The standard loop is located in front of the prototype with a distance of 20 mm. The center of these two antennas are aligned for maximum near-field coupling as shown in Fig. 51. The input power level of the network analyzer is set to -35 dBm, which is also the maximum power the prototype can handle for transmission. This is because the nonlinearity [31] [32] of its thin-film YIG core limits the prototype to only interact with RF signals of power below certain level. Beyond this threshold, the magnitude of the dip in S11 due to the FMR starts to shrink. And the larger the power is injected into the prototype, the more the energy transfers to the magnetic lattice of the thin-film YIG and dissipates as heat, which increases the quality factor of the material and decreases the radiation efficiency enhancement to the prototype. 400 sampling points are taken uniformly on a frequency band from 0.5 GHz to 1 GHz.

After the standard calibrations for each equipment involved in the measurement are carried out, the S11 and S21 parameters of the modified single loop prototype without inserting the YIG thin-film are measured and recorded first. These data of S11 and S21 will be used for three purposes: 1) for comparison; 2) to determine the noise floor of the measurement environment and 3) for post process de-embedding. Then insert the YIG thin-film sample to the prototype, apply and adjust the magnetic bias field to the prototype and measure the same S parameters again.

To compare the measurement result with the HFSS simulation, a loop model with dimensions and the relatively location described as above is added into HFSS and simulated together with the FMR enhanced small single loop to obtain the corresponding S11 and S21 parameters. The standard loop in HFSS is assigned with a lumped port excitation. The parameters and geometry of the PCB used in prototype fabrications are also loaded into the simulation space.

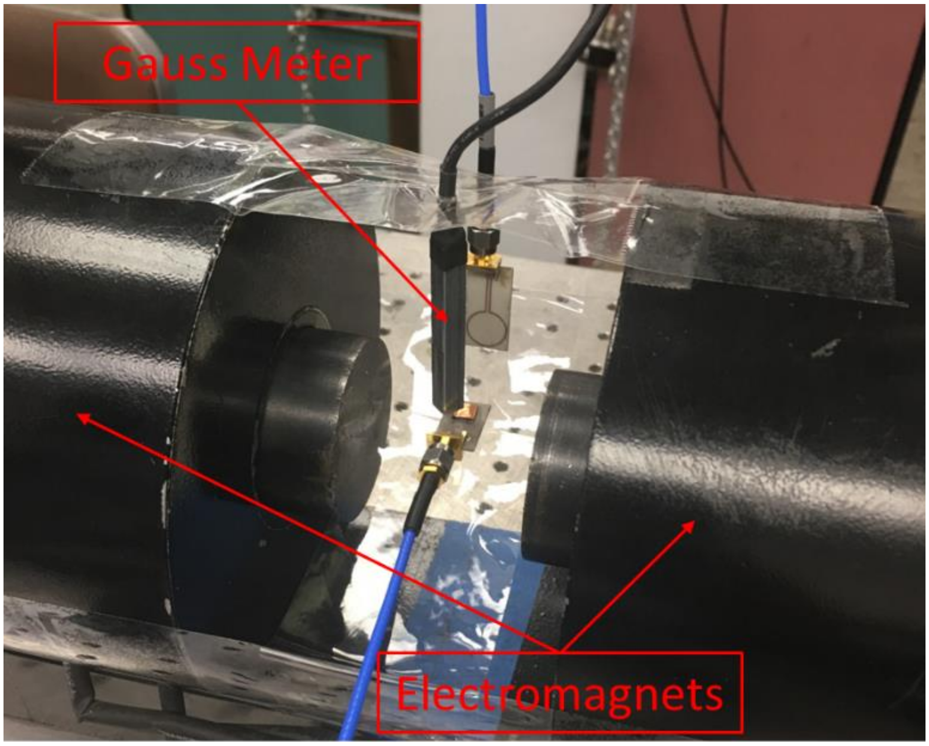

Figure 50. The measurement setup for the near-field measurement.

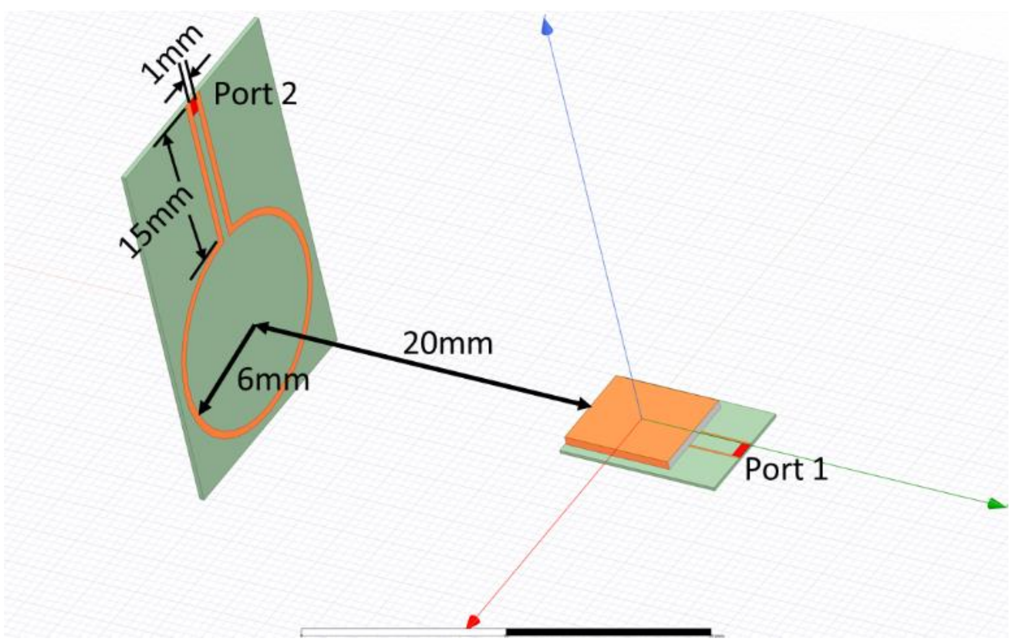

Figure 51. The HFSS model for near-field measurements.

What is worth to be mentioned is that the near-field measurement can also be conducted by measuring in S12, which means the prototype is in the receiving mode. It can free the prototype from the power limit to a certain degree, but not completely get rid of it. 20 mm is the maximum distance that the prototype can be detected when acting in the transmitting mode under current experimental condition. 35mm is the maximum range when the prototype is in the receiving mode. Since, the phenomenon will be the same in S21 and S12 when detected, only the result of S21 is studied and shown in the next section.

One of many solutions to lower the interference (the noise floor) from the coupling between the two antennas and increase the detection range of the prototype is also tried here. After the LNA is integrated with the prototype, the nearfield measurement is conducted again as the prototype in the receiving mode to check how much improvement in the detection range as shown in Fig. 52.

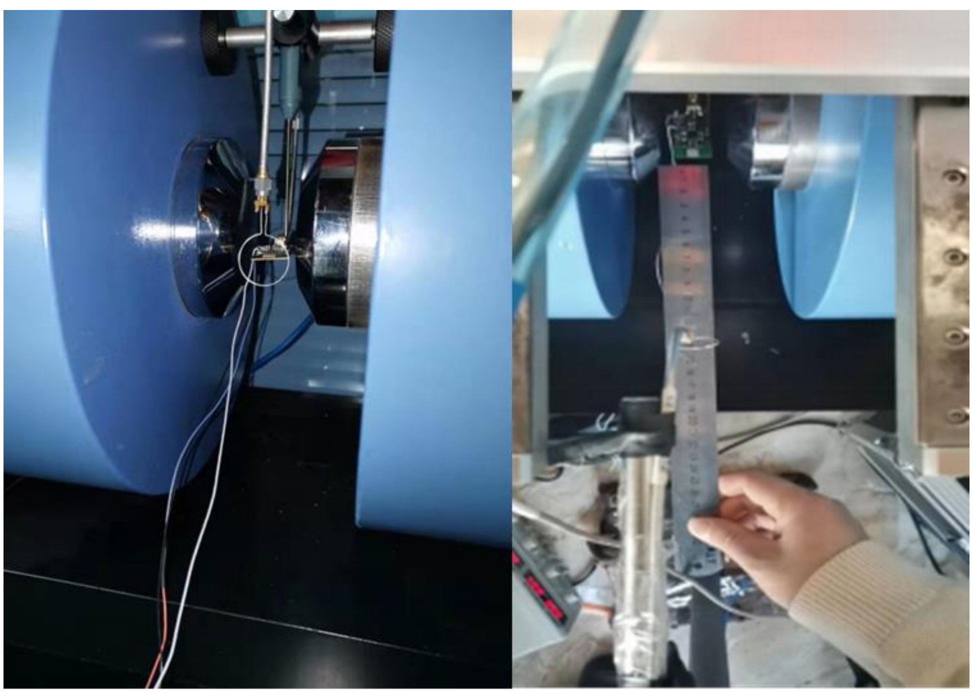

Figure 52. The near-field measurements with LNA and the test range records.

All the setups for the near-field measurement remains the same except this time the prototype is connected to port 2 of the network analyzer and the standard loop is connected to port 1. So it is again the S21 that will be examined and recorded. A DC voltage supply is also added to drive the LNA. The current maximum test range with LNA is 100 mm or more, as shown in the Fig. 52, which is almost three times longer than the one without LNA. And with such big increases in detection distance, the far-field measurement is also been performed.

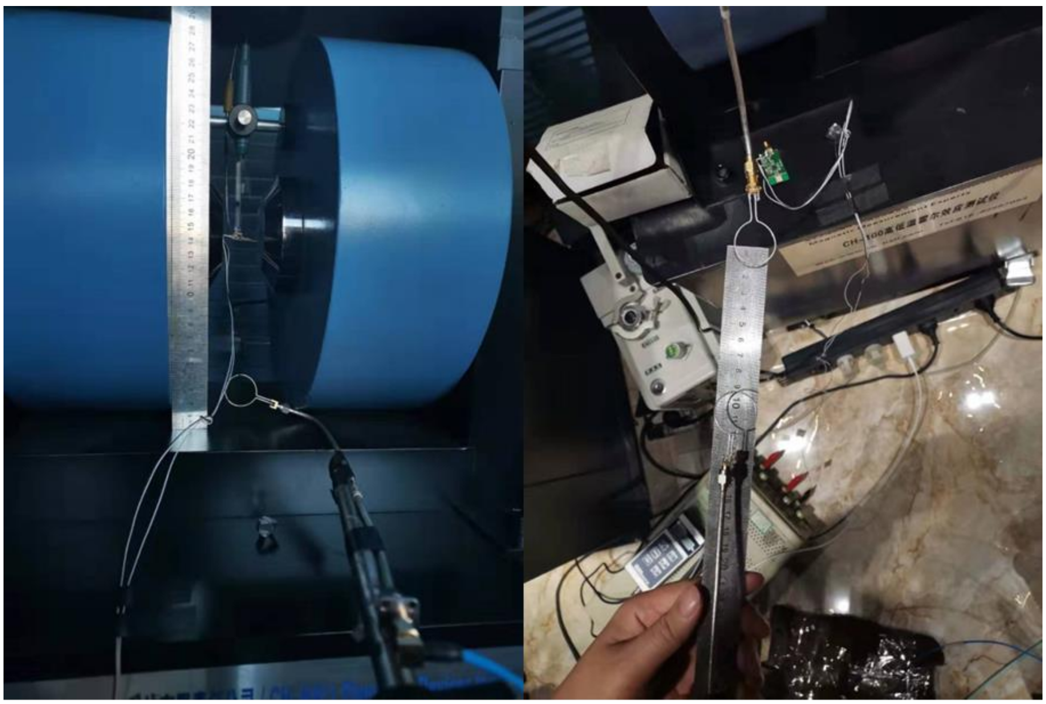

(a) (b)

Figure 53. The far-field measurement and gain comparison setups: a) the prototype with LNA and the standard loop; b) two standard loops.

The setup for far-field measurements is shown in Fig. 53 (a). The distance between the prototype and the standard loop antenna stays at 100mm. However, different from the near-field setup, the standard loop is placed below the prototype, not in front of it. The input power is set to -15dBm. The corresponding HFSS model for the far-field measurement is shown in Fig. 54. In order to extract the radiation efficiency from the far-field measurements, gain comparison method is applied here. So two identical standard loops with gap of 100 mm are also measured as shown in Fig. 53 (b). S21 of two scenarios are recorded.

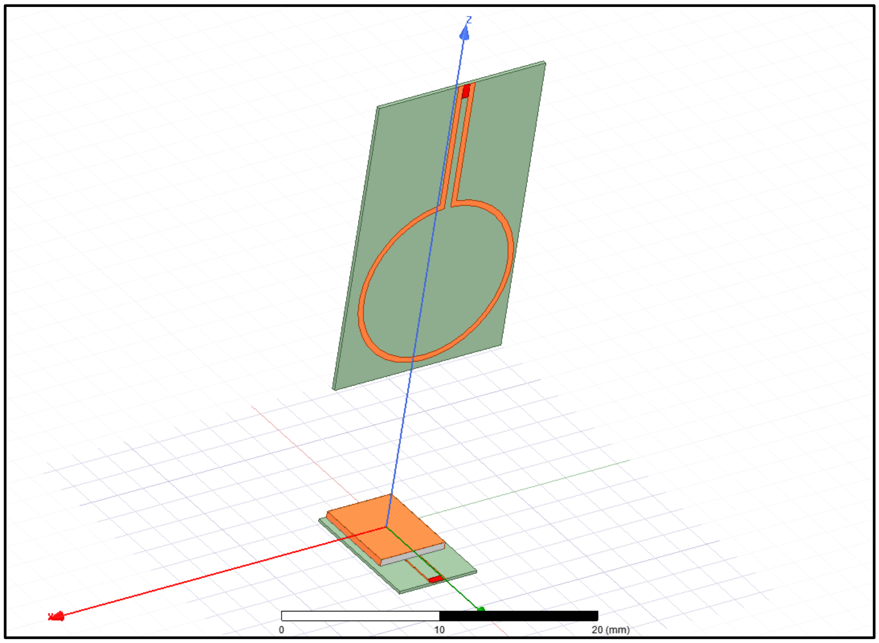

Figure 54. The HFSS model for far-field measurements.

6.3 Results Exhibitions

Measured results of two S parameters mentioned above, under three different DC magnetic bias fields: 40Oe, 45Oe and 50Oe, are recorded and shown here. The curves of S11 and S21 are plotted together in Fig. 55 for the easy identification of impacts due to FMR. Three different dips in S11, with magnitude of all about 16dB, are observed over a frequency range of 0.5 GHz to 1 GHz. The frequencies of those dips are 0.738 GHz, 0.782 GHz and 0.823 GHz, which are corresponding to the FMR frequencies associated with those three DC magnetic bias field applied to the prototype, respectively. The fact that the dip in S11 is moving along with the change of the magnetic bias field indicates that those dips are caused by the FMRs. Dips in S11 shows more input power are delivered to the prototype because of the impedance matching improvement at FMR frequencies. Peaks in S21, with magnitude of about 8 dB, around FMR frequencies are also observed along with those dips in S11. Peaks in S21 illustrate that more power transmitted from the prototype is detected by the standard loop due to the impact of FMRs. In other words, the radiation performance is enhanced at FMR frequencies. Full-wave simulation results also corroborate the story told by the experiments. However, the FMR frequencies measured under different magnetic bias fields are all slightly lower than those extrapolated by HFSS simulations or the Kittel's equation. This is because the inner field of the thin-film ferrite H_0 is usually smaller than the externally applied field H_a due to M_s , i.e. $H_a = H_0 + M_s$. The gauss meter can only measure H_a. The HFSS results shown in Fig. 55 has already taken the difference between H_a and H_0 into account. And the strength of the bias fields H_0 in HFSS has been modified accordingly to achieve better matches between measurements and simulations around FMR frequencies. The discrepancy of about 20 dB between the measured and simulated noise level in S21 happens because of the unexpected residue of two antennas' strong coupling in the experimental setup.

With the LNA, the S21s and S22 (S11) under bias field 50Oe are exhibited in Fig. 56. Move the standard loop antenna away from the prototype starting from 5mm. And record the S21 at 25 mm, 35 mm, 45 mm and 100mm. and plot them together. It is quite obvious that at the same FMR frequency, peaks in S21 can be seen at every different locations. The sight deviation in frequency between the deep in S22 and the peaks in S21 might be caused by the loading of the LNA and the balun, which is trivial.

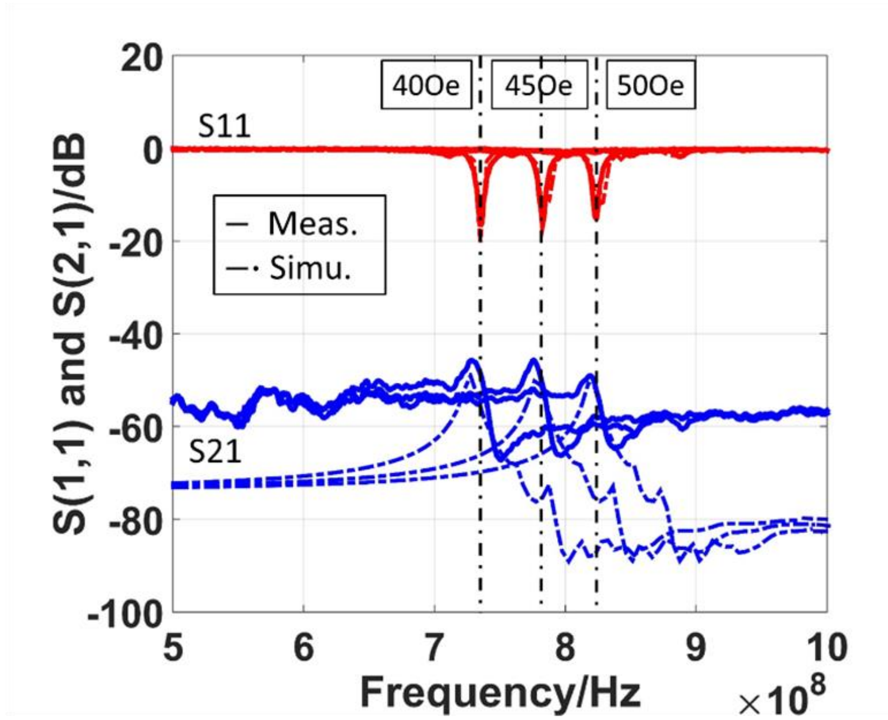

Figure 55. S11 and S21 under different bias: 40Oe, 45Oe and 50Oe: Simulations vs Measurements.

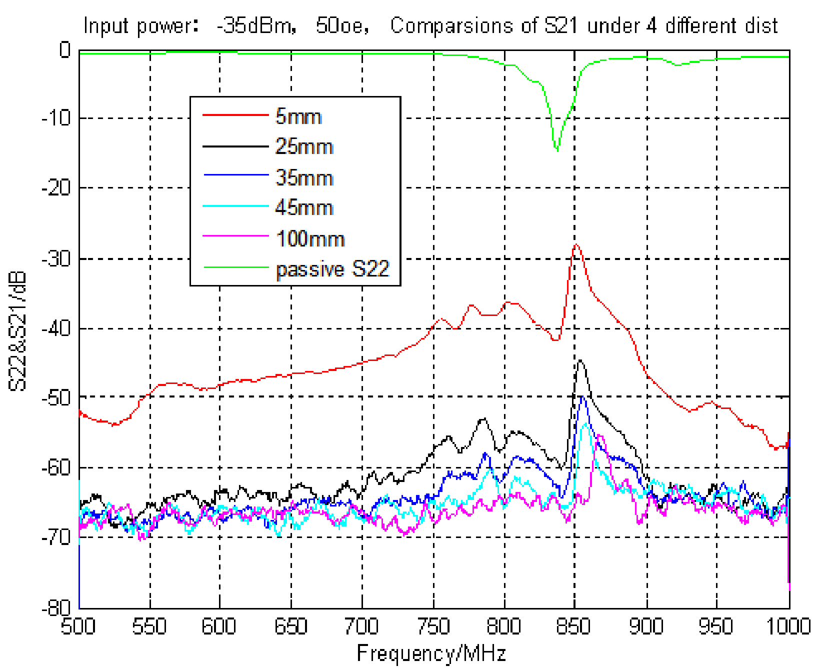

Figure 56. S22 and S21 with LNA under bias 50Oe at different detection range.

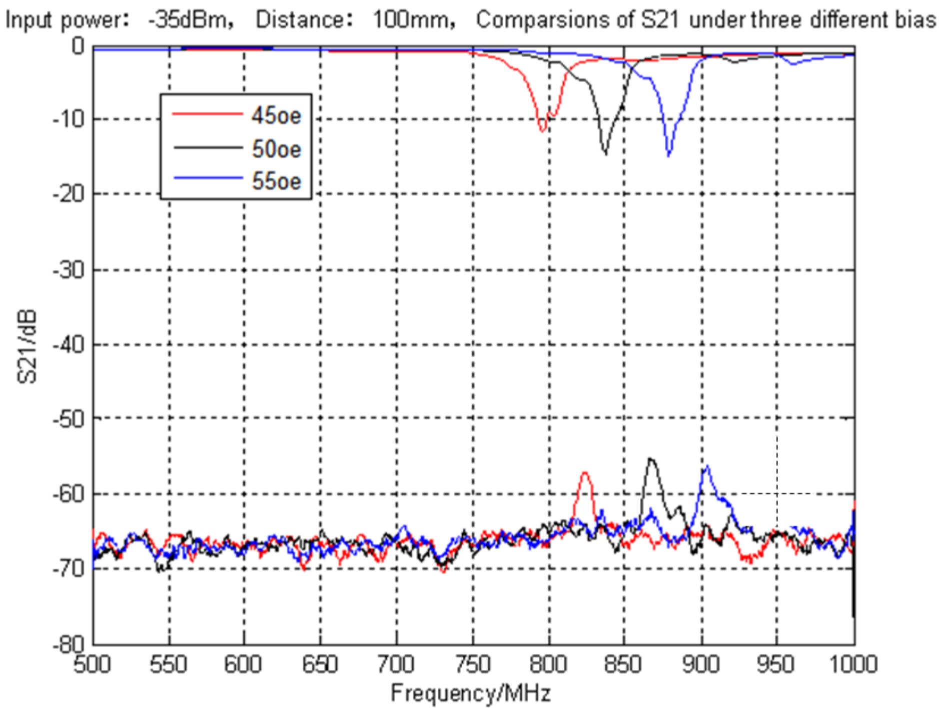

Figure 57. S22 and S21 with LNA under different bias at 100mm point.

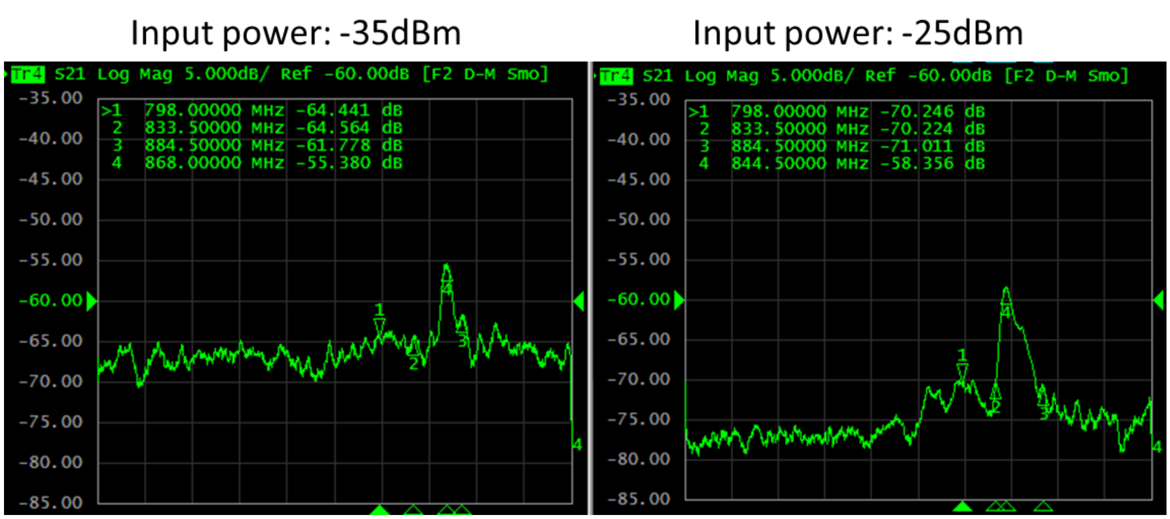

Figure 58. Comparisons of S21 with different input power under bias 50Oe at 100 mm.

At 100 mm, the peak is still relatively large to the noise floor. The magnitude of the peak in S21 at 100 mm is about 10 dB. Different bias: 45Oe, 50Oe and 55Oe are also been applied to test the tunability of the prototype and to validate the peak is generated through FMR. The result is shown in Fig. 57. Since with the integration of the LNA, more input power can be handled, the situation with -25 dBm as the input power setting has been tested as well. Compared with the -35 dBm case at 100 mm, it is clear that a larger peak of 15 dB is obtained at the same frequency,as shown in Fig. 58, which means the prototype has the potential to receiving signal from a longer distance with a higher transmitting power. In other words, the design of FMR enhanced ESAs in this dissertation with LNA is ready to be used in more practical scenarios.

S21 from the far-field measurement is displayed in Fig. 59. The same phenomenon as S21 obtained in the near-field is observed here. With higher input power (-15 dBm) at the transmitting end, higher peaks, about 20 dB, and lower noise floor, about -80 dB, are shown at the receiving end, which proves the role of the LNA played in the communication link measurements (near and far-field).

Figure 59. S22 and S21 with LNA under different bias from the far-field measurements.

The procedure for extracting efficiency E_{rad} from the measured S21 is shown as below:

Record S_{21}^{s}between two standard loops and S_{21}^{t} between the FMR ESA and a standard loop. So the receiving power of the standard loop antenna P_s and the FMR antenna with the LNA P_t are:

$$P_s = P_{input} + S_{21}^{s} \tag{6.1}$$

$$P_t = P_{input} + S_{21}^{t} - G_{LNA} \tag{6.2}$$

where P_{input} is the power injected in the standard loop and G_{LNA} is the gain of the LNA, set as -15 dBm, as stated before. The gain of the FMR enhanced ESA G_t can be calculated through comparing with the gain of the standard loop G_s, like:

$$G_t(dB) = P_t(dBm) - P_s(dBm) + G_s(dB) \tag{6.3}$$

The gain of the standard loop G_s can be obtained by substituting (6.1) into Friis function:

$$P_{input} + S_{21}^{s} = P_{input} + 2G_s(dB) - 20\log[R * 10^{-6}]\,(km) - 20\log[\mathrm{f}]\,(\mathrm{MHz}) - 32.44 \tag{6.4}$$

$$G_S = \frac{S_{21}^{S} + A}{2} \tag{6.5}$$

where A $= 20\log[R * 10^{-6}]\,(km) + 20\log[\mathrm{f}]\,(\mathrm{MHz}) + 32.44$ and R is 100 mm in this case.

Substitute (6.1), (6.2) and (6.5) into (6.3), we will have the gain of the FMR antenna G_t. Since almost all ESAs have low directivity with a pattern shaped somewhat like a distorted donut, it is fair to estimate that the directivity of the FMR enhanced ESAs D equals to 1.76dB. Therefore, the total efficiency of FMR enhanced ESA can be extrapolated as:

$$E_{total}(dB) = G_t(dB) - D(dB) \tag{6.6}$$

At last, transfer $E_{total}(dB)$ to $E_{total}(persentage)$.

The measured E_{total} at three different bias, 45Oe, 50Oe and 55Oe, are plotted together in Fig. 60 and compared with the corresponding simulated efficiencies. It is quite clear that all three peaks in the total efficiency produced by the full-wave simulation match well to those three peaks in measurements. The measured total efficiency of FMR enhanced ESA is about 0.017% as predicted by the simulations.

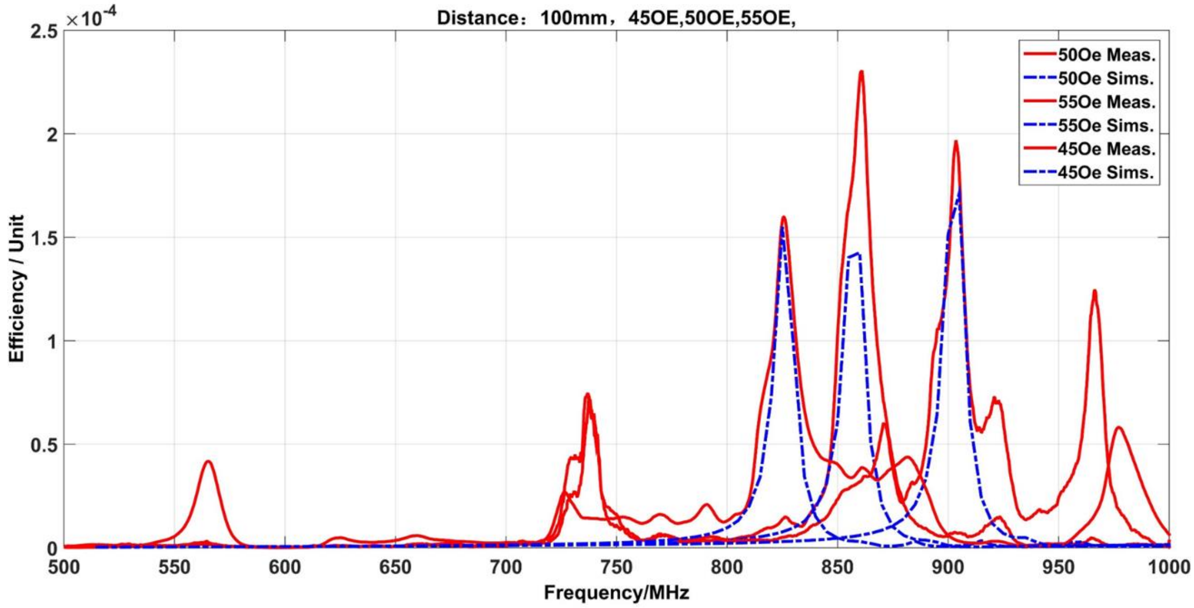

Figure 60. Total efficiency Comparisons between simulations and measurements.

By far, the experiments to measure impedance and efficiency of FMR enhanced ESAs have been fully conducted. All measurement results validate the idea of using FMR to improve both the impedance matching ability and the radiation efficiency of ESAs.

CHAPTER VII
CONCLUSIONS

The expression of radiation efficiency for ESAs with respect to μ' and μ'' is derived through examining a physics model of an ideal, thin-film ferrite radiator and compared with that in the literature.

The theory that thin-film ferrite with large μ'' can be utilized to design ESAs with high efficiency has been proven theoretically and practically.

The idea of designing highly efficient ESAs with thin-film ferrites and FMR combined is realized for the first time through a modified small single loop antenna loaded with the thin-film YIG. It is also the first time that not only just high μ'' but also the FMR has been proposed and validated through full-wave simulations and experiments for solving the poor impedance matching and low radiation efficiency issues simultaneously in the design of ESAs.

Novel yet comprehensive, frequency-independent equivalent circuit models for inductive ESAs and FMR enhanced ESAs are developed in this dissertation respectively to provide future guidance of designing such ESAs in the system level. The input impedance and radiation efficiency calculated through the circuit models well matched to the full-wave simulations.

A prototype for FMR enhanced ESAs has been fabricated and tested with near-field measurement setups. The experimental results of S parameters are reported here and compared with full-wave simulations. The consistency in those results verify the feasibility of FMR enhanced ESAs. After the low noise amplifier is integrated with the prototype, the detection range of the prototype is significantly increased and it shows that FMR enhanced ESAs are almost ready to directly implement to IOT applications, such as antennas in 5G smart phones, wearable devices for biomedical monitoring and etc., which will be discussed in future publications.

REFERENCES

[1] D. Evans, “The internet of things. How the next evolution of the internet is changing everything,” *Cisco White Paper*, 2011.

[2] L. Lizzi, F. Ferrero P. Monin, C. Danchesi and S. Boudaud, “Design of Miniature Antennas for IoT Applications”, *2016 IEEE Sixth International Conference on Communications and Electronics (ICCE)*, 2016.

[3] W. L. Stutzman and G. A. Thiele, *Antenna Theory and Design*, Hoboken, NJ, USA: Wiley, 2012.

[4] S. Schelkunoff and H. Friis, *Antenna Theory and Practice*, Wiley, 1952.

[5] H. A. Wheeler, "The radian sphere around a small antenna," Proc. IRE, vol. 47, pp. 1325-1331, Aug. 1959.

[6] H. Wheeler, "Small Antennas," *IEEE Trans. Antennas Propag*., vol. 23, no. 4, pp. 462-469, Jul.1975.

[7] C. A. Balanis, *Advanced Engineering Electromagnetics*. Hoboken, NJ, USA: Wiley, 2012.

[8] L. J. Chu, "Physical limitations of omni-directional antennas," *J. Appl. Phys*., vol. 35, pp. 1479-1484, 1948.

[9] Y.T. Lo and S.W. Lee, Eds., Antenna Handbook: *Theory, Applications, and Design*, Van Nostrand Reinhold, 2284 pp., 1988.

[10] H. Wheeler, "Fundamental limitations of small antennas," Proc. IRE, vol. 35, pp. 1479-1484, Jul. 1947.

[11] J. S. McLean, "A Re-examination of the Fundamental Limits on the Radiation Q of Electrically Small Antennas," *IEEE Trans. Antennas Propag*., vol. 44, no. 5, pp. 672-676, May, 1996.

[12] J. D. Adam, L. E. Davis, G. F. Dionne, E. F. Schloemann, and S. N. Stitzer, “Ferrite devices and materials,” *IEEE Trans. Microw. Theory Techn*., vol. 50, no. 3, Mar. 2002.

[13] M. Wu and A. Hoffmann, “Ferrites for RF passive devices,” in Solid State Physics, vol. 64. Oxford, U.K.: Academic, 2013, pp. 237–326.

[14] Z. Yao, Y. E. Wang, S. Keller, and G. P. Carman, “Bulk acoustic wave-mediated multiferroic antennas: Architecture and performance bound,” *IEEE Trans. Antennas Propag*., vol. 63, no. 8, pp. 3335–3344, Aug. 2015.

[15] M. Smith, "Properties of dielecrically loaded antennas," *Proc. IEE Electronics*, vol. 124, no. 10, pp. 837-839, Oct. 1977.

[16] S. Long, M. McAllister and L. Shen, "The resonant cylindrical dielectric cavity antenna," *IEEE Trans. on Antennas Propag*., vol. 31, pp. 406-412, Mar. 1983.

[17] Petosa, "Dielectric reosnator antennas: A historical review and the current state of the art," *IEEE Trans. Antennas Propag*., vol. 52, no. 5, pp. 91-116, Oct. 2010.

[18] V. Rumsey and W. Weeks, "Electrically small ferrite loaded loop antennas," *IRE Nat. Conv. Rec*., vol. 4, no. 1, pp. 165-170, 1956.

[19] V. Rumsey, "Reaction concept in electromagnetic theory," *Phys. Rev*., vol. 94, no. 6, pp. 1483-1491, Jun. 1954.

[20] R. DeVore and P. Bohley, "The electrically small magnetically loaded multiturn loop antenna," *IEEE Trans. Antennas Propag*., vol. 25, pp. 496-505, 1977.

[21] H. Stuart and A. Yaghjian, "Approaching the lower bounds on Q for electrically small electric dipole antennas using high permeability shells," *IEEE Trans. Antennas Propag*., vol. 58, no. 12, pp. 3865-3872, Dec. 2010.

[22] J. Lee, Y. K. Hong, S. Bae, G. S. Abo, W. Seong, and G. Kim, “Miniature Long-Term Evolution (LTE) MIMO Ferrite Antenna”, *IEEE Antennas Prop. Letters*, vol. 10, 2011.

[23] W. Lee, Y. K. Hong, J. Park, M. Choi, J. Lee, I. Baek, N. Hur and W. Seong, “Low-Profile Multiband Ferrite Antenna for Telematics Applications”, *IEEE Trans. Mag*., vol. 52, No. 7, Jul. 2016.

[24] L.-R. Tan, R.-X. Wu, C.-Y. Wang, and Y. Poo, “Ferrite-loaded SIWbowtie slot antenna with broadband frequency tunability,” *IEEE Antennas Wireless Propag. Lett.*, vol. 13, pp. 325–328, 2014.

[25] H. Moon, G. Lee, C. Chen and John L. Volakis, “An Extremely Low-Profile Ferrite-Loaded Wideband VHF Antenna Design”, *IEEE Antennas Prop. Letters*, vol. 11, 2012.

[26] J. S. McLean and R. Sutton, “An efficient, low-profile antenna employing lossy magneto-dielectric materials,” *in Proc. IEEE Int. Workshop Antenna Technol. (iWAT)*, Mar. 2012, pp. 261–264.

[27] J. McLean, H. Foltz and R. Sutton, "Electrically small TE01 mode spherical wire antennas employing lossy magnetodielectric materials," *in International Workshop on Antenna Technology Proceedings*, Lisbon, Portugal, Mar. 2010.

[28] T. Hansen, O. Kim and O. Breinbjerg, "Electrical properties of spherical dipole antennas with lossy material cores," *in 6th European conference on Antennas and Propag.*, Prague, Czech Republic, Mar. 2012.

[29] T. Yousefi, T. Sebastian, and R. E. Diaz, “Why the magnetic loss tangent is not a relevant constraint for permeable conformal antennas,” *IEEE Trans. Antennas Propag.*, vol. 64, no. 7, pp. 2784–2796, Jul. 2016.

[30] T. Sebastian, “Magneto-dielectric wire antennas theory and design,” *Ph.D. dissertation, Dept. Elect. Eng.*, Arizona State Univ., Tempe, AZ, USA, 2013.

[31] B. Lax and K. J. Button, *Microwave Ferrites and Ferrimagnetics*. New York, NY, USA: McGraw-Hill, 1962.

[32] D. M. Pozar, *Microwave Engineering, 3rd ed*. Hoboken, NJ, USA:Wiley, 2005, ch. 9, pp. 441–485.

[33] G. M. Yang, X. Xing, A. Daigle, M. Liu, O. Obi, S. Stoute, K. Naishadham, and N.X. Sun, “Tunable miniaturized patch antennas with self-biased multilayer magnetic films”, *IEEE Trans Antennas Propag 57 (2009)*, 2190–2193.

[34] W. Gu, Q. Xu, and Y. E. Wang, “Two dimensional (2D) complex permeability characterization of thin film ferromagnetic material,” *in Proc. IEEE Conf. Antennas Meas. Appl*., Syracuse, NY, USA, Oct. 2016, pp. 1–4.

[35] H. Cui, Z. Yao and Y. E. Wang, “Coupling Electromagnetic Wave to Spin Waves: A Physics-Based Nonlinear Circuit Model for Frequency-Selective Limiters,” *IEEE Trans. Microw. Theory Techn.* vol: 67 , Issue: 8 , Aug. 2019.

[36] MTI Corporation. YIG Epi Film on GGG Substrate datasheet. Accessed: Jul. 6, 2016.

[37] P. Kohnke, *ANSYS Theory Reference Release 5.6*., Ansys, 1994.

[38] V. Bekker, K. Seemann, and H. Leiste, “A new strip line broad-band measurement evaluation for determining the complex permeability of thin ferromagnetic films,” *J. Magn. Magn. Mater.*, vol. 270, no. 3, pp. 327–332, Apr. 2004.

[39] Rogers RO4003C datasheet. Accessed on Oct. 8, 2019.

[40] Texas Instruments LMH5401 datasheet. Accessed on Nov. 30, 2019.